Probing the atmospheres of scorching exoplanets via spectroscopy

Bárbara Silva Oliveira
Master in Astronomy and Astrophysics
Department of Physics and Astronomy
Faculty of Sciences of the University of Porto
2025

Probing the atmospheres of scorching exoplanets via spectroscopy

Bárbara Silva Oliveira

Dissertation carried out as part of the Master in Astronomy and Astrophysics

Department of Physics and Astronomy

2025

Supervisor

Olivier Demangeon, Dr., Instituto de Astrofísica e Ciências do Espaço

Universidade do Porto

Masters Thesis

Probing the atmospheres of scorching exoplanets via spectroscopy

Author:
Bárbara Oliveira

Supervisor:
Dr. Olivier Demangeon

A thesis submitted in fulfilment of the requirements
for the degree of MSc. Astronomy and Astrophysics

at the

Faculdade de Ciências da Universidade do Porto
Departamento de Física e Astronomia

February 6, 2026

Acknowledgements

I am sincerely grateful to all those who have supported me throughout this work. This thesis would not have been possible without the guidance and support of my supervisors, Dr. Olivier Demangeon and (almost Dr.) Ana Rita Silva. They not only made this work possible, but also supported me through every step of it. With them, I learned so much and I am forever grateful for their patience, care, and for making this a good and enriching experience.

I would not be in this position without the great teachers and professors who shaped me along the way, and for them I am deeply thankful. I also thank everyone at CAUP/IA for welcoming me and providing all the conditions necessary to carry out my work.

A big thank you to my friends, the ones I made along this journey and to those who have been there since the start. To Rui and Bernardo: thank you for the help and companionship through every challenge of the bachelor's and for keeping lunchtime fun. To Catarina, Salgado, Raquel, Gonçalo and Carlos: my life trajectory would have been very different and much more boring without you to call my best friends.

To my family I am forever thankful for cheering me on, supporting me, and complementing me where I lack. To my mom, for being everything she is, for giving me this world, and for encouraging me to explore others. To my sister, for being the greatest companion in life. To my dad, for ensuring I received the education he was never allowed to. To my cherished family members - Vóvó, Tia Lurdes, Ana, Juca, and others - I thank you for creating fun in times of stress. Very importantly, to my cat, Micas, for sleeping peacefully non stop through my every crisis. And finally, to my boyfriend, Yuri, where I find friendship, love, and family, for simply being the most fascinating and kind person I will ever have the luxury to encounter and who gets me through every journey I decide to embark on.

Resumo

As atmosferas planetárias têm vindo a atrair um crescente interesse como um passo para a descoberta de importantes perspetivas sobre a formação, estrutura e evolução dos planetas. Entre a vasta população de exoplanetas conhecidos, os Júpiteres ultraquentes fornecem laboratórios únicos para estudos atmosféricos, devido às suas altas temperaturas e, consequentemente, atmosferas extensas. Um membro desta população é o WASP-76 b, um caso de estudo popular nos últimos anos, para o qual foram detetadas várias espécies químicas atómicas, moleculares e ionizadas.

Com este trabalho pretendemos confirmar a estrutura térmica da atmosfera de WASP-76 b, detetando emissão de Fe I no lado diurno do planeta. Uma emissão diurna desta espécie indica uma camada de inversão térmica na atmosfera, previamente verificada em planetas tórridos.

Para avaliar a presença de Fe I no lado diurno de WASP-76 b, trabalhámos com observações espectroscópicas de alta resolução das fases de pré e pós-ocultação, obtidas com o instrumento de última geração ESPRESSO no VLT. Após um cuidadoso processamento dos dados e isolamento da componente do planeta, comparamos os dados com um espetro sintético da atmosfera do planeta incluindo Fe I, produzido com o código petitRADTRANS. A comparação baseou-se no método de correlação cruzada, resultando numa deteção da emissão de Fe I no lado diurno de WASP-76 b.

Combinámos as CCFs de todas as observações, obtendo uma deteção com desvio para o azul com o valor de RV $= -4.6 \pm 0.3\,\mathrm{km\,s^{-1}}$ e com significância de 4.3σ. Encontrámos também assimetrias entre o pré e o pós-eclipse, com este último a exibir uma assinatura mais forte, mas menos deslocada. Discutimos como estas descobertas apontam para a existência de um *hotspot*, embora a sua posição ainda não possa ser determinada.

Este estudo reforça a evidência de uma inversão térmica em WASP-76 b e demonstra a capacidade da espectroscopia terrestre de alta resolução para investigar a emissão diurna de UHJ. Observações futuras, combinadas com modelos de circulação global, serão essenciais para desvendar a dinâmica atmosférica e caracterizar completamente a estrutura térmica deste planeta e de UHJ semelhantes.

Palavras-chave: Espetroscopia; Exoplanetas; Atmosfera; WASP-76b

Abstract

Planetary atmospheres have been acquiring growing interest as an indirect path towards uncovering key insights on planet formation, structure and evolution. Among the vast population of known exoplanets, ultra-hot Jupiters provide unique testbeds for atmospheric studies, due to their high temperatures and, consequently, extended atmospheres. A member of this population is WASP-76 b, a popular case study in recent years, for which a number of atomic, molecular and ionised chemical species have been detected.

With this work we intended to confirm the thermal structure of WASP-76 b's atmosphere by detecting neutral iron emission on the dayside of the planet. A dayside emission of this species indicates a thermal inversion layer in the atmosphere, previously verified on scorching planets.

To assess the presence of Fe I in the dayside of WASP-76 b, we worked with high-resolution spectroscopic observations of pre- and post-occultation ranges, obtained with state-of-the-art instrument ESPRESSO at the VLT. After careful data processing and isolating the planet's component we cross-correlated it to a synthetic atmospheric spectrum with Fe I produced with petitRADTRANS. The comparison relied on the cross-correlation method, yielding a successful detection of Fe I emission on the dayside of WASP-76 b.

We combine the CCFs from all observations, obtaining a blueshifted detection at RV = $-4.6 \pm 0.3\,\mathrm{km\,s^{-1}}$ with a significance of 4.3σ. We also find asymmetries between the pre- and post-eclipse, with the latter exhibiting a stronger yet less shifted signature. We discuss how these findings point to the existence of a hotspot, although its position cannot be constrained yet.

This study strengthens the evidence for a thermal inversion in WASP-76 b and demonstrates the capability of ground-based, high-resolution spectroscopy to probe dayside emission from UHJ. Future observations, combined with global circulation models, will be key to disentangling atmospheric dynamics and fully characterising the thermal structure of this planet and UHJ alike.

Keywords: Spetroscopy; Exoplanets; Atmospheres; WASP-76b

Table of Contents

List of Tables v
List of Figures vi
Glossary ix

1. Introduction 1
   1.1. Exoplanet Atmospheres 2
   1.2. Atmospheric detection and characterisation methods 7
      1.2.1. Transit or Transmission Spectroscopy 7
      1.2.2. Emission and Reflectance Spectroscopy 10
      1.2.3. The cross-correlation method 11
   1.3. Manuscript Structure 13
2. WASP-76 b observations 14
   2.1. Planet Overview 14
   2.2. ESPRESSO spectroscopic data 20
3. Data Reduction 24
   3.1. Telluric correction: Molecfit 24
   3.2. Continuum Normalisation (Spectra Normalization Tool) 29
   3.3. Outlier Identification 32
      3.3.1. Full-spectrum smoothing + Mean Absolute Deviation (MAD) clipping 34
      3.3.2. Spectrum smoothing + Mean Absolute Deviation (MAD) clipping - using the continuum only 35
      3.3.3. Time-wise flux outlier detection 35
   3.4. Stellar Rest Frame Alignment 37
   3.5. Stellar Template and Planet Spectrum Extraction 41
4. Analysing the Planet Spectra 45
   4.1. Synthetic Model with petitRADTRANS 45
   4.2. Cross-Correlation Method 47
   4.3. Discussion 54
5. Conclusions 58

Bibliography 59

List of Tables

2.1. Stellar parameters of the WASP-76 system....16
2.2. Planetary parameters of WASP-76 b....17
2.3. Summary of atomic, ionic, and molecular detections in the atmosphere of WASP-76 b reported in the literature. 18
2.4. Summary of atmospheric detections in WASP-76 b from the literature....19
2.5. Overview of observational logs for each night....22

4.1. Results from the Gaussian fits to the CCFs. 55

List of Figures

1.1. Confirmed exoplanets from the Encyclopedia of Exoplanetary Systems, showing their orbital periods and planetary radius. The shown planets are divided into categories based on their sizes and periods. The Solar System planets are also presented for reference. The planets in which at least one molecule was detected in their atmosphere are highlighted in yellow. 3
1.2. Figure 1 from Madhusudhan (2019): Schematic of an exoplanet atmosphere divided into three main layers. The predominant physical and chemical processes are shown per layer, as well as the reach of UV, optical and IR spectroscopy. The temperature profiles are shown for a thermally inverted (red line), non-inverted (blue line), and poorly irradiated planet (dashed gray line) scenarios. 4
1.3. Adapted from Figure 2 of Winn (2010), representing a schematic illustration of a planetary transit. The upper part shows the coordinate system, with the star centred at the origin in the X–Y plane and the positive Z axis pointing towards the observer. The lower part displays the corresponding idealised transit light curve, indicating the four contact points (t_{I}–t_{IV}), the ingress/egress duration τ, the total transit duration T, and the transit depth δ. These contact points mark the instants when the stellar and planetary disks are tangent as seen by the observer. The segments between the first and second, and between the third and fourth contact points are referred to as the ingress and egress phases, respectively. 8
9figure.caption.8
1.5. Figure 1 from Prinoth et al. (2022), demonstrating the geometry of the transmitted light at the beginning (A), middle (B) and end (C) of a transit. The evening terminator is shown in blue, while the morning is shaded red. α_{max} is the orbital angle at which ingress is finished. The intensity of the shaded regions represents the contribution of the respective limb to the overall observed spectrum. 9
1.6. Schematic adapted from Winn (2009) and Perryman (2018), demonstrating the flux variations through an entire orbit, including transit and occultation. 10
1.7. Figure 4.1 from Prinoth (2025), demonstrating the cross-correlation method applied to spectroscopy. 12

2.1. Orbital diagram of WASP-76 b indicating the observed epochs and corresponding orbital phases (ϕ). Adapted from Costa Silva, A.R. et al. (2024). 22
2.2. Diagnostic plots showing the variation of key observational parameters during the four ESPRESSO visits, as a function of orbital phase. 23

3.1. Molecfit's GUI displaying one of our input spectra in blue, the inclusion regions in the shaded green area and the atlas spectra of the molecules H_2O (top panel) and O_2 (bottom panel) in orange. The yellow shaded regions are not relevant for the purpose of this manuscript. 27
3.2. Section of the first spectrum (before correction) of Epoch I, in blue, with the final configuration of the inclusion, in green, and exclusion, in red, regions used for the telluric correction. 28
3.3. Comparison between one of the original spectra (black) and its telluric-corrected version (red). The best-fit transmission spectrum from `molecfit` is also shown (blue dashes), scaled for visibility. 28

3.4. Zoom into the 5915–5925 Å region, showing one of the original spectra (black), its telluric-corrected version (red), and the best-fit transmission spectrum (blue dashes). The correction successfully removes most telluric absorption features, though some residuals remain in saturated regions. 29
3.5. Continuous spectrum from a hot, dense source. Bottom panel: the photographic spectrum (a rainbow-coloured strip). Top panel: the same spectrum as an intensity vs. wavelength plot. Source: N. Vogt, NMSU lecture notes. 30
3.6. Emission line spectrum. Top panel: photographic spectrum with bright coloured lines. Bottom panel: corresponding intensity vs. wavelength plot showing sharp emission peaks. Source: N. Vogt, NMSU lecture notes....31
3.7. Absorption line spectrum. Top panel: photographic spectrum showing dark absorption lines across the rainbow background. Bottom panel: corresponding intensity vs. wavelength plot with 'v'-shaped absorption dips. Source: N. Vogt, NMSU lecture notes. 31
3.8. Continuum normalisation process of the first observation of Epoch I, as an example. The top panel shows the measured spectrum in blue, and the continuum fit in red, while the bottom panel presents the normalised spectrum. 32
3.9. Masked spectral regions, delimited by the shaded pink area, plotted over a spectrum, in blue, and the telluric transmission of H_2O and O_2, in orange. 33
3.10. Outliers identified with the full spectrum smoothing and MAD clipping method, shown as purple points. 34
3.11. Same as Figure 3.10 for the smoothing and MAD clipping (using only the continuum) method. 35
3.12. Same as Figure 3.10 for the time-wise flux outlier detection method. 36
3.13. Number of outliers detected in the exposures of each epoch, separated into panels. The three outlier detection methods are shown, namely the full spectrum smoothing shown as the blue points, the continuum only smoothing shown in green and the time-wise flux in orange. 37
3.14. Adapted from Figure 1.11 from Seidel (2021). Schematic of reference frame shifts. **I**: BERV correction of the Earth's movement around the SSB. **II**: Shift from the SSB to the target system's barycentre (SSB): v_{sys}. **III**: Shift from the target system's barycentre to the SRF: Equation (3.4) **IV**: Shift from the target system's barycentre to the PRF: Equation (3.4)....39
3.15. Observed stellar RV values divided into epochs, with the corresponding fits represented by the orange lines. 41
3.16. Stellar template for each Epoch (median-stacked spectra in SRF). 42
3.17. Planetary spectrum from epoch I shown in the SRF, after subtracting the stellar template. 43
3.18. Comparison in different wavelength ranges of the first and last exposures of normalised stellar spectra of Epoch I with the extra masks to be applied shaded in red. 44

4.1. Comparison between the adopted P-T profile (blue) and a similar Guillot profile (orange)....46
4.2. Synthetic model emission spectrum of Fe I for WASP-76 b, produced with petitRADTRANS....49
4.3. Different forms of the synthetic emission spectrum of Fe I created with petitRADTRANS. The mainly used one is shown in the top left panel. 50
4.4. Resulting CCFs of each exposure split into epochs in the PRF. 50

4.5. Summed CCF per epoch, along with Gaussian profiles fitted to the regions near null RV, shown in black. The vertical black dashed lines represent the centres of the fitted profiles. 51
4.6. Global CCF resulting from the sum of all observations, in blue, with its respective Gaussian fit, in black. The vertical black dashed line represents the centre of the fitted profile. 51
4.7. Comparison between the resulting summed CCFs obtained through different methods. 52
4.8. K_p-v_{sys} plot of the Fe I detection, with the intensity in arbitrary units. The blue crosshair locates the maximum intensity point while the black dashed lines indicate the expected position of the peak, assuming no dynamics or asymmetric structure. 53
4.9. Resulting CCFs from summing all pre-eclipse (A) and post-eclipse (B) exposures. Each is shown with its respective Gaussian fit to the peak near null RV, in black. 53
4.10 Figure 8 from Costa Silva, A.R. et al. (2024), showcasing a schematic of the WASP-76 system and the hypothesised hotspot geometry in a no-offset (A) and a west offset (B) scenarios, at pre- and post-eclipse positions. The effect of blue and redshifts is represented by blue and red arrows, respectively. 56

1. Same as Figure 4.8 for each epoch separately. 78
2. Part of Figure A.7 from Guilluy et al. (2025), showcasing a schematic of the WASP-76 system, assuming a hotspot deviated towards East and its effect on the observed temperature gradient. 78

Glossary

BJD	Barycentric Julian Date
UHJ	Ultra-Hot Jupiter
ESPRESSO	Echelle SPectrograph for Rocky Exoplanet and Stable Spectroscopic Observations
VLT	Very Large Telescope
UT	Unit Telescopes
UHR	Ultra-High Resolution
HR	High Resolution
MR	Medium Resolution
S/N or SNR	Signal-to-Noise ratio
GTO	Guaranteed Time Observation
DRS	Data Reduction System
LBLRTM	Line-By-Line Radiative Transfer Model
LSF	Line Spread Function
GDAS	Global Data Assimilation System
GUI	Graphic User Interface
SNT	Spectra Normalization Tool
RV	Radial Velocity
MAD	Mean Absolute Deviation
CCF	Cross-Correlation Function
STIS	Space Telescope Imaging Spectograph
HST	Hubble Space Telescope
P-T	Pressure-temperature
PRF	Planet's Rest Frame
SRF	Stellar Rest Frame
SSB	Solar System Barycentre

BERV Barycentric Earth RV

CIA Collision Induced Absorption

GCM Global Circulation Models

FWHM Full Width at Half Maximum

Chapter 1

Introduction

The discovery of planets orbiting stars outside our Solar System had a profound impact on the field of astronomy and altered the perspective of both scientists and the general public about the universe we inhabit. The very first detection of a planetary companion beyond the Solar System was done in 1991 by Wolszczan and Frail (1992) on the pulsar PSR B1257+12. It was not long after, in 1995, when the first exoplanet around a Sun-type star was found by Mayor and Queloz (1995). Since these findings, the study of exoplanets has advanced at a remarkable pace, revealing both the abundance and the diversity of planetary systems in our galaxy. These planets span an enormous range of orbital configurations, sizes, masses, temperatures, and stellar host environments, surpassing the variety and scales observed within our own Solar System.

An important aspect to consider when trying to characterise the rising number of known exoplanets is their atmospheres. The study of planet atmospheres, although a very recent field of study, has bloomed over the past few years due to how important it has become in the characterisation of exoplanets. From the first detection of an exoplanet atmosphere by Charbonneau et al. (2002) on the hot Jupiter HD 209458 b using the space based instrument Space Telescope Imaging Spectrograph (STIS) aboard the Hubble Space Telescope (HST), to the first ground based atmosphere detection (Redfield et al., 2008), it has become clear that atmospheric studies provide key insights into the planet's chemical and physical properties, and allow us to peek into the formation processes involved (Madhusudhan, 2019). When we talk about how special Earth's conditions are for harbouring life, we must give credit to the Earth's atmosphere, which protects life from harmful UV radiation, regulates the temperature, provides us with essential gases and protects

us from small body impacts. Therefore, we can easily understand how fundamental atmospheres are to define favourable environmental conditions for the emergence of life, making their study fundamental in the quest for habitable worlds.

At the present time, the study of atmospheres is one of the exciting frontiers of exoplanet science. A multitude of atoms, molecules, clouds, and hazes have been detected in different planetary atmospheres by both space and ground based telescopes. Among the vast population of planets, the most frequently studied are the hot Jupiters, which present extensive hydrogen and helium envelopes containing several other atomic species. Neptune-sized and sub-Neptune planets appear to be the most common type of exoplanet, with atmospheres rich in volatiles and molecular species such as water and methane (Grasser et al., 2024). Lower in the size scale are the rocky or terrestrial planets, which are believed to have lost their primordial H/He atmosphere. Through processes such as volcanic outgassing, these planets present secondary atmospheres with elements including carbon dioxide and nitrogen, appearing overall more similar to those of the Earth, Venus, Mars or Titan (Swain et al., 2021, Hu et al., 2024). The rapid evolution of this area of research stems from improvements in both observations and theoretical models, which catapulted the age of atmospheric characterisation.

1.1. Exoplanet Atmospheres

The growing interest in the field of exoplanet studies has resulted, so far, in 5989 detections *. Figure 1.1 shows the confirmed exoplanets from the NASA Exoplanet Archive† with measured orbital period and planetary radius, and sorts them into categories based on their size and some based on their period as well. The size boundaries were defined based on Borucki et al. (2011): Earth-size, or terrestrial planets ($< 1.25R_{\oplus}$), super-Earth-size ($1.25 - 2R_{\oplus}$), Neptune-size ($2 - 6R_{\oplus}$), and Jupiter-size ($6 - 15R_{\oplus}$). The Jupiter-size planets were classified between hot Jupiters, limited to orbital periods of less than 10 days, and ultra-hot Jupiters with periods shorter than 3 days (Gaudi et al., 2005). Highlighted with a yellow edge are the planets in which at least one molecule was detected in their atmosphere, according to the Encyclopedia of Exoplanetary Systems.

*`https://exoplanetarchive.ipac.caltech.edu/`, retrieved on 29^{th} August 2025.
†`https://exoplanetarchive.ipac.caltech.edu/`

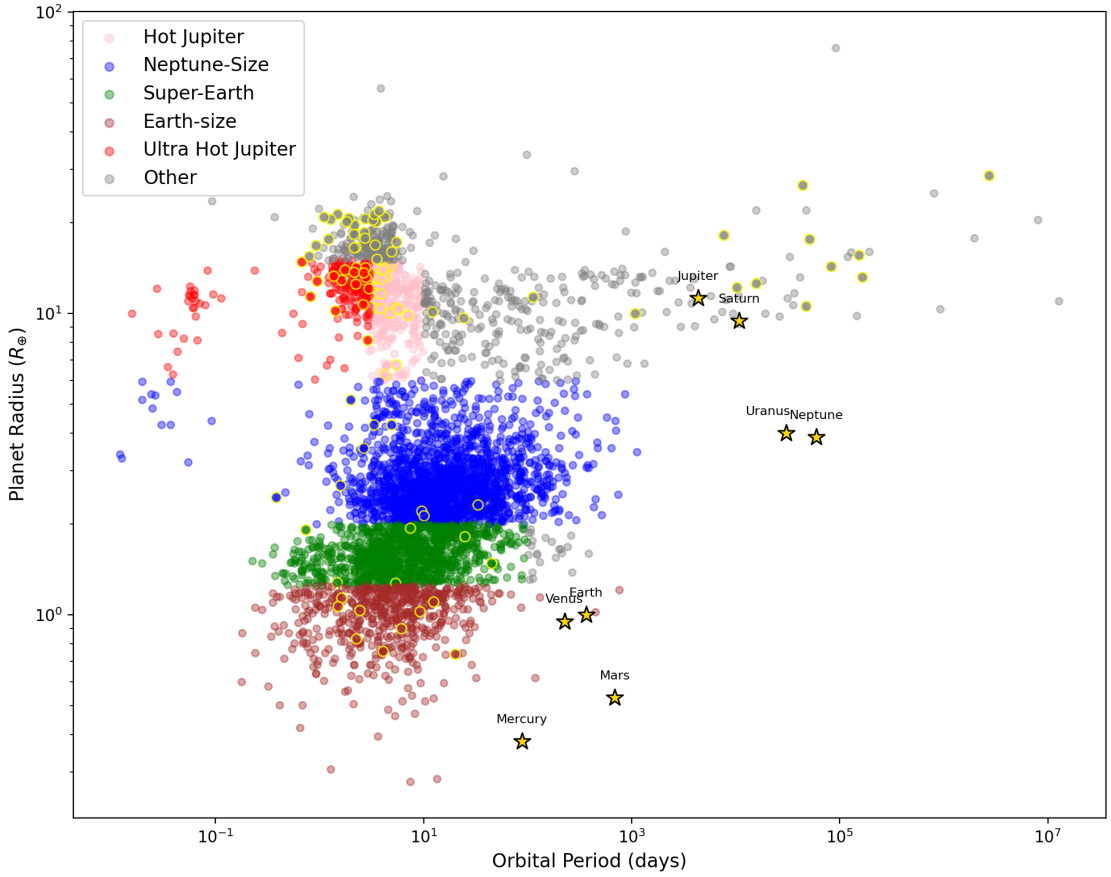

FIGURE 1.1: Confirmed exoplanets from the Encyclopedia of Exoplanetary Systems, showing their orbital periods and planetary radius. The shown planets are divided into categories based on their sizes and periods. The Solar System planets are also presented for reference. The planets in which at least one molecule was detected in their atmosphere are highlighted in yellow.

Exoplanets exhibit a broad distribution in basic physical properties: radii from ~ 0.2 to $\gtrsim 18\ R_\oplus$, masses covering several orders of magnitude, and equilibrium temperatures from a few hundred to several thousand Kelvin. This diversity naturally extends to atmospheric properties: composition, mean molecular weight, pressure–temperature (P–T) profiles, and the limits of chemical and thermodynamic equilibrium. These differences reflect the internal, historical, and stellar processes associated with each planet (Madhusudhan et al., 2014).

A planetary atmosphere is the gaseous layer surrounding a planet, with observable features influenced by its vertical stratification, that is, its pressure and temperature structure, chemical composition, and dynamical processes. For strongly irradiated exoplanets, the atmosphere can be divided into three main vertical regions: a deep layer (pressures $\gtrapprox 1$ bar) where chemical and radiative–convective equilibrium often hold; a photospheric layer ($\approx 10^{-3} - 1$ bar) where most molecular spectral features originate and dynamics,

clouds/hazes and temperature inversions become relevant; and an upper, rarified layer ($\lessapprox 10^{-6}$ - 10^{-3} bar) dominated by photochemistry and atmospheric escape. Observations probe different altitudes depending on wavelength: UV and visible light mainly sample the upper atomic and ionic layers, near- and mid-infrared measurements probe molecular bands in the photosphere, and extreme UV can reveal escaping exospheres (Madhusudhan, 2019, Madhusudhan et al., 2014). Figure 1.2 illustrates a schematic of an exoplanet atmosphere, highlighting how different spectral ranges probe distinct layers and, consequently, different physical and chemical processes (Madhusudhan, 2019).

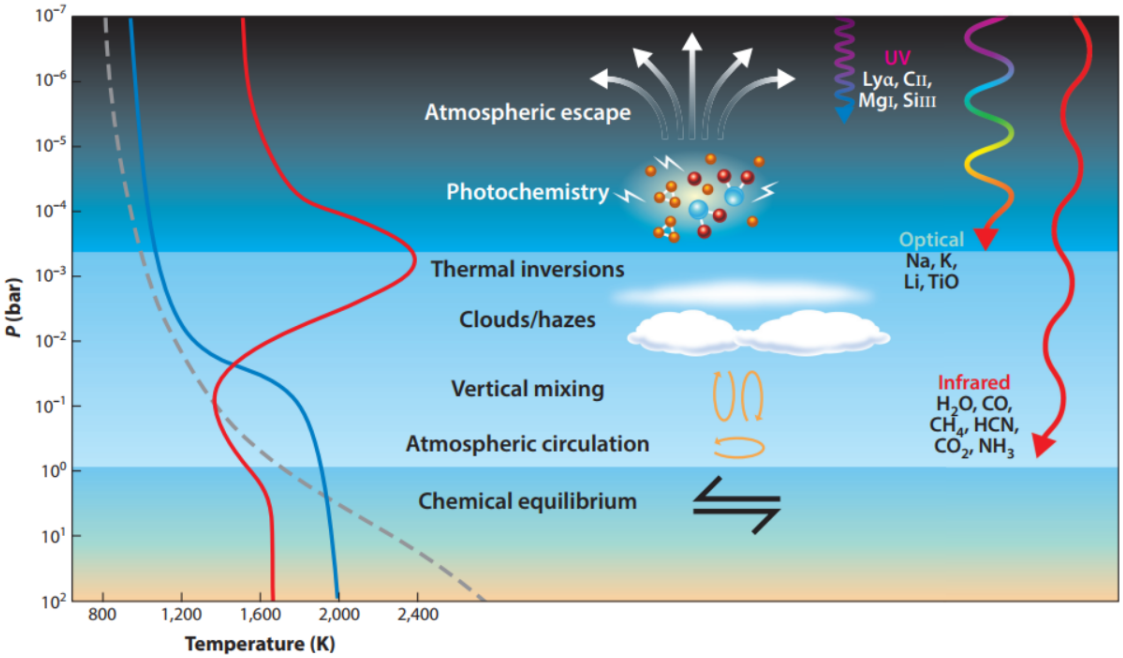

FIGURE 1.2: Figure 1 from Madhusudhan (2019): Schematic of an exoplanet atmosphere divided into three main layers. The predominant physical and chemical processes are shown per layer, as well as the reach of UV, optical and IR spectroscopy. The temperature profiles are shown for a thermally inverted (red line), non-inverted (blue line), and poorly irradiated planet (dashed gray line) scenarios.

Some important concepts for atmospheric studies are the equilibrium temperature, $T_{\rm eq}$, of a planet and the atmospheric scale height.

The equilibrium temperature of an irradiated planet is defined as the blackbody temperature assuming equilibrium between the incident stellar flux and its re-emission (thermal emission and reflected light). Equation (1.1) defines the equilibrium temperature as in Equation 2 of Charbonneau et al. (2005) and 6.158 of Perryman (2018), where $T_\star$ is the effective temperature of the star, a is the planet's semi major axis and A_B is the Bond albedo, this is, the fraction of incident light which is reflected, integrated over all wavelengths (Madhusudhan et al., 2014). The parameter f refers to the heat redistribution factor and

is set to 1 for a planet whose temperature is uniform throughout its whole surface. Assuming $f = 1$ and $A_B = 0$, which is a reasonable approximation for most hot Jupiters (Madhusudhan et al., 2014, Burrows et al., 2008, Rowe et al., 2008), we can approximate Equation (1.1) to Equation (1.2).

$$T_{\text{eq}} = T_\star \left(\frac{R_\star}{2a}\right)^{1/2} \left[f\,(1 - A_B)\right]^{1/4} \tag{1.1}$$

$$T_{\text{eq}} \simeq T_\star \left(\frac{R_\star}{2a}\right)^{1/2}, \tag{1.2}$$

In cases where the absorbed stellar energy is re-radiated exclusively from the dayside, as in the case of tidally locked planets lacking oceans or atmospheres, then $f = 2$ and the predicted temperature will increase by a factor of $2^{1/4}$ (Madhusudhan et al., 2014, Perryman, 2018).

Another important definition for the study of atmospheres, in particular transit spectroscopy, as we will see in Section 1.2, is the atmospheric scale height, H, defined in Equation (1.3), where k_B is Boltzmann's constant, T the atmospheric temperature, μ_m the mean molecular weight, and g the gravity.

$$H = \frac{k_B T}{\mu_m g} \tag{1.3}$$

This quantity becomes important when trying to define the atmosphere as an ideal gas in hydrostatic equilibrium and when determining the area of the atmosphere intercepted by stellar light during a planet transit (see Section 1.2) which corresponds to an annulus of radial extent $\approx 5H$ (Seager and Deming, 2009). This is simply a reference value of the atmosphere's extent, while the detectable height of the atmosphere depends on other factors, including the spectral resolution. When considering the atmosphere as an ideal gas in hydrostatic equilibrium, we can describe the pressure P at a height h using Equation (1.4) (Seager, 2010), where T is the temperature of the atmosphere at height h. When considering constant temperature values with altitude, the atmospheric scale height, H, represents the height for which the pressure decreases by a factor of e.

$$\frac{\mathrm{d}\ln P}{\mathrm{d}\,h} = -\frac{1}{H} \;\Rightarrow\; P(h) = P(0)\,\exp\left(-\int_0^h \frac{\mu_m g}{k_B T(h')}\,dh'\right) \tag{1.4}$$

Before describing in more detail how we can characterise the atmospheres, we should have an understanding of their constituents.

In the same way as the gas giants in our Solar System, such as Jupiter and Saturn, extrasolar gas giants possess atmospheres dominated by hydrogen and helium. Depending on the planet's temperature, other spectral features appear superimposed on these broad envelopes. On hot and ultra-hot Jupiters it is expectable to find features from alkali metals such as sodium, Na (Charbonneau et al., 2002), and potassium, K (Sing et al., 2011). Depending on their temperature, we can also expect heavier molecular species, including water vapour, H_2O (Wakeford et al., 2013, Deming et al., 2013, Kreidberg et al., 2014), methane, CH_4 (Swain et al., 2008), carbon monoxide, CO (Brogi et al., 2012), and ammonia, NH_3 (Yang et al., 2024).

Neptune-like exoplanets and smaller sub-Neptunes also retain atmospheres dominated by H_2/He, remnants of their primordial envelopes. However, in contrast to hot Jupiters, they tend to show higher fractions of heavier volatiles such as H_2O, CH_4, NH_3 and CO_2 (Madhusudhan et al., 2023, Beatty et al., 2024). This is likely a consequence of their lower masses, which facilitate atmospheric escape of the lightest gases (H/He), and the persistence of these molecules at lower temperatures. Examples include HAT-P-11 b, where HST/WFC3 detected water absorption Fraine et al. (2014); and GJ 436 b, whose featureless transmission spectrum points to a high-metallicity atmosphere depleted in methane and possibly obscured by clouds/hazes (Lanotte et al., 2014).

A particularly intriguing part of the planetary diversity lies in rocky or terrestrial exoplanets. Their atmospheres are expected to be enriched in heavier molecules produced by processes such as volcanic outgassing and surface-atmosphere interactions, rather than the primordial H/He gas from the protoplanetary nebula (e.g. Hu et al., 2024). They are thought to have lost their primary atmospheres and developed secondary ones, rich in species such as CO_2, N_2, or SO_2, more akin to those of Earth, Venus, or Mars. Because of their higher mean molecular weight, such atmospheres have smaller scale heights, H, which reduces the amplitude of spectral features in transmission spectroscopy. Moreover, the presence of clouds and hazes can mute or flatten absorption features, leading to nearly featureless spectra. An illustrative case is GJ 1132 b, where HST data revealed hints of a secondary atmosphere containing CH_4, NH_3, and HCN, possibly replenished by volcanic outgassing (Swain et al., 2021).

1.2. Atmospheric detection and characterisation methods

The detection and characterisation of exoplanetary atmospheres rely on high-precision spectroscopic techniques that aim to analyse these atmospheres across different wavelength bands and during various phases of the planets. These techniques enhance the signals obtained in order to confidently determine the composition, structure, and dynamics of the atmospheres. The most commonly used methods to detect and characterise an atmosphere are transmission, emission, and reflectance spectroscopy, which we will discuss in the following subsections.

1.2.1 Transit or Transmission Spectroscopy

A transit is observed when a planet passes between its host star and the line of sight of the observer (e.g. Charbonneau et al., 2000, Henry et al., 2000). When the planet passes in front of the star, it dims its light, causing a dip in luminosity, which can be observed in light curves (plot of the variation of flux vs. time). We can observe an illustration of a transit and its light curve in Figure 1.3. In the image we can observe the four contact points of a transit: first contact marks the beginning of the transit, when the planet's limb first touches the stellar disk, while the fourth contact corresponds to the same configuration on exit. The second and third contacts occur when the planet is fully inside the stellar disk, marking the end of ingress and the start of egress, respectively. Measuring the light radiated from the star before, during and after the planet's transit, we can compute some physical properties of the system. For example, the depth, δ, of the transit informs us on the amount of light blocked out by the planet and therefore the relative radius of the planet, as expressed by Seager and Mallén-Ornelas (2003) in Equation (1.5), where $F_\star$ is the stellar flux out-of-transit, F_{obs} is the observed flux during transit, R_p is the radius of the planet, and $R_\star$ is the stellar radius.

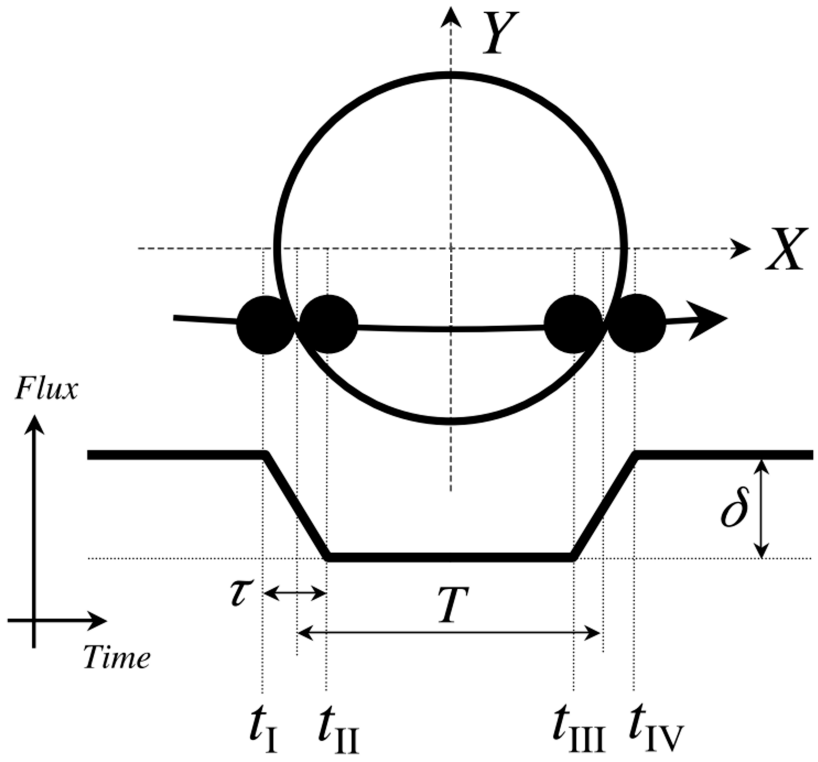

FIGURE 1.3: Adapted from Figure 2 of Winn (2010), representing a schematic illustration of a planetary transit. The upper part shows the coordinate system, with the star centred at the origin in the X–Y plane and the positive Z axis pointing towards the observer. The lower part displays the corresponding idealised transit light curve, indicating the four contact points (t_{I}–t_{IV}), the ingress/egress duration τ, the total transit duration T, and the transit depth δ. These contact points mark the instants when the stellar and planetary disks are tangent as seen by the observer. The segments between the first and second, and between the third and fourth contact points are referred to as the ingress and egress phases, respectively.

$$\delta = \frac{F_\star - F_{obs}}{F_\star} \sim \left(\frac{R_p}{R_\star}\right)^2 \tag{1.5}$$

When we take into consideration that a transiting planet may possess an atmosphere, we can understand that the stellar light is further dimmed as a consequence of its extent. Unlike the planet itself, which is fully opaque, part of the starlight passes through the atmospheric limb, as schematically shown in Figure 1.4. This transmitted light carries the chemical imprint of the planet's atmosphere, having been filtered by its constituent species. This principle forms the basis of transmission spectroscopy, a widely used technique to detect and study exoplanetary atmospheres and the method that enabled their first detection. The region of the atmosphere probed by transmission spectroscopy is defined as the terminator. This region can be split into two categories: the leading (morning) terminator and trailing (evening) terminator. Because the planet is spinning around

its rotation axis, these two limbs introduce opposite Doppler shifts: the leading terminator usually appears slightly red-shifted, while the trailing terminator appears slightly blue-shifted. Figure 1.5 shows how the stellar light probes the terminator region.

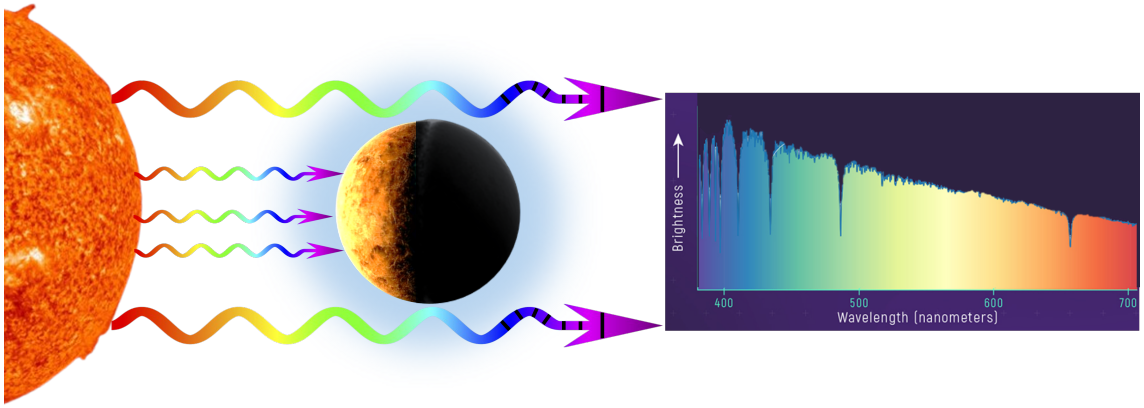

FIGURE 1.4: Schematic of stellar light being transmitted through the atmosphere of a planet. On the right is an example of a stellar spectrum containing the effect of the planet's atmosphere. This image was made from different sources.*

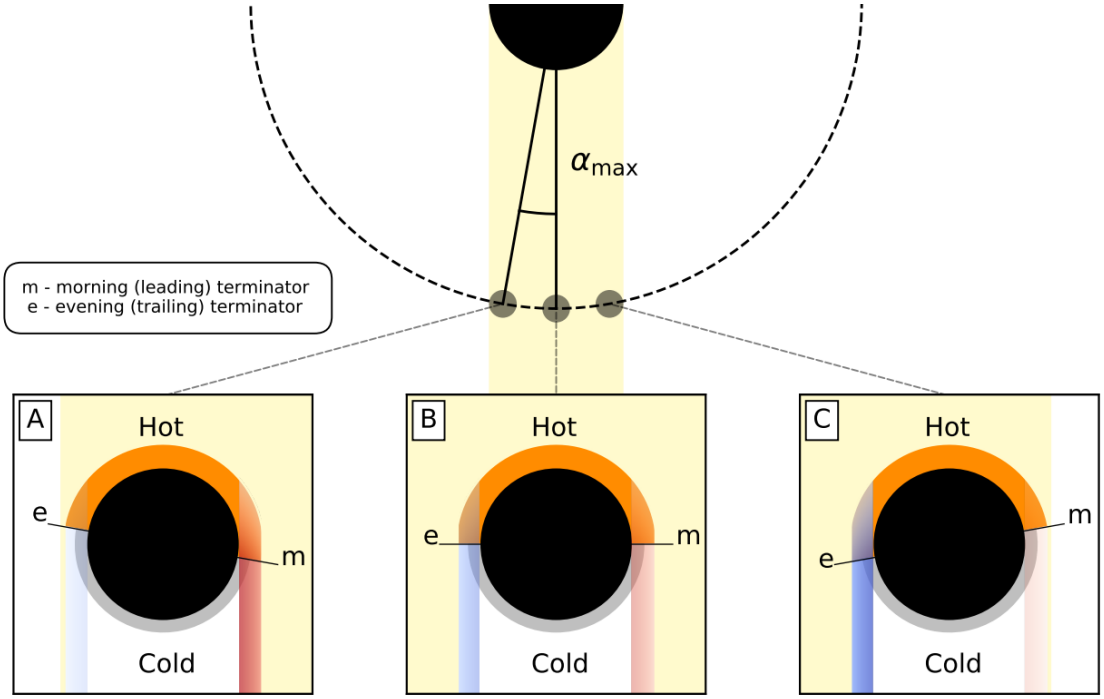

FIGURE 1.5: Figure 1 from Prinoth et al. (2022), demonstrating the geometry of the transmitted light at the beginning (A), middle (B) and end (C) of a transit. The evening terminator is shown in blue, while the morning is shaded red. α_{max} is the orbital angle at which ingress is finished. The intensity of the shaded regions represents the contribution of the respective limb to the overall observed spectrum.

*Credit:
Image of the Sun: NASA/ SDO/AIA
Image of the spectrum: NASA, ESA, CSA, Leah Hustak (STScI)
Image of the planet: Tobias Stierli/Flaeck

If we now consider the planet's full light curve, as shown in Figure 1.6, the planet both passes in front of the star and moves behind it. The primary transit (or simply transit, as we have been describing it) has a counterpart event 180º out of phase, when the planet is hidden behind the star. This event is referred to as an occultation, secondary transit, or secondary eclipse. During the transit, the planet blocks a portion of the starlight. After the transit, the illuminated day-side gradually steps into view, increasing the observed flux. The flux decreases again during the secondary eclipse, when the planet passes behind the star, leaving only the stellar flux, and rises once more as the day-side becomes visible again. While transmission spectroscopy probes the terminator region of the atmosphere, occultations enable us to study the dayside emission of the planet, which leads us to another atmosphere detection and characterisation technique: emission spectroscopy.

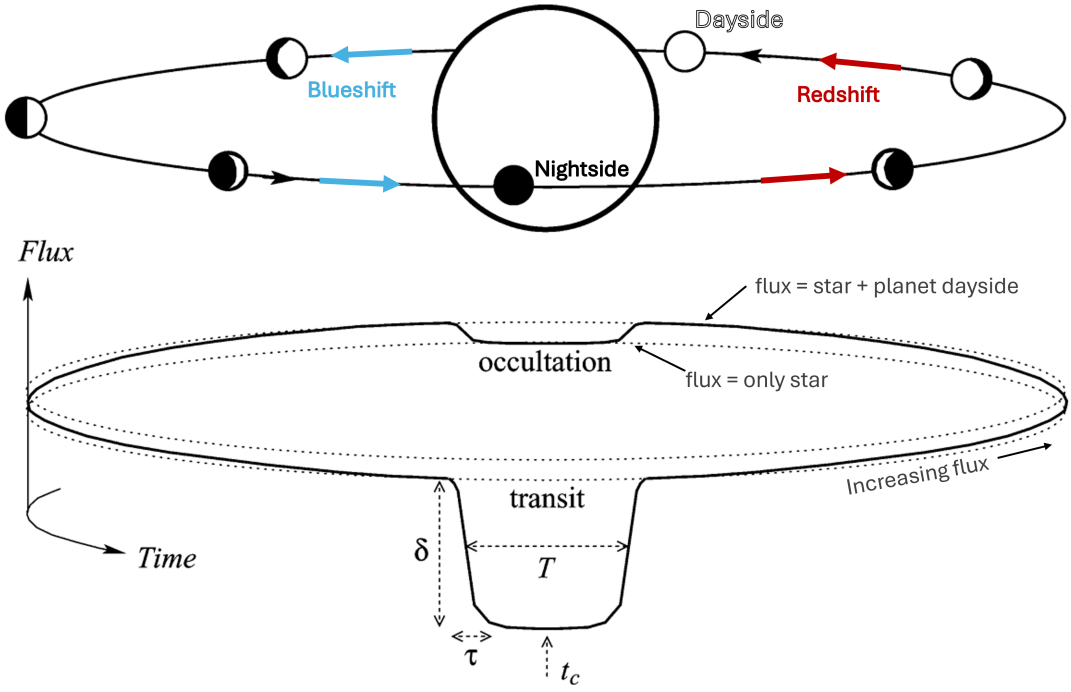

FIGURE 1.6: Schematic adapted from Winn (2009) and Perryman (2018), demonstrating the flux variations through an entire orbit, including transit and occultation.

1.2.2 Emission and Reflectance Spectroscopy

Emission spectroscopy allows us to study the dayside atmosphere of an exoplanet by measuring the combined light from the star and planet when the planet's illuminated hemisphere is visible. Typically, the planetary spectrum is obtained by comparing the flux just before and after the secondary eclipse (star + planet) with that measured during the eclipse itself (star only). In practice, however, useful information can also be obtained

from spectra taken immediately outside the eclipse, when the dayside still contributes to the observed signal, as is done in this work.

At optical wavelengths, the planetary signal contains both thermal emission and reflected starlight, while in the infrared it is dominated by thermal emission. This allows us to constrain the temperature structure of the dayside atmosphere and to identify molecular and atomic species through their emission and absorption features. In particular, the depth of the secondary eclipse provides the planet's flux at different wavelengths, which can be expressed as brightness temperatures $T_b(\lambda)$, that is, the temperature a blackbody would need in order to emit the observed flux at a given wavelength (see Equation (1.6), where B_λ is the Planck function) (Perryman, 2018, Alonso et al., 2009):

$$F_\lambda^{\text{planet}} = B_\lambda \left(T_b(\lambda)\right) \Rightarrow T_b = \frac{hc}{k\lambda} \ln^{-1}\left(1 + \frac{2hc^2}{\lambda^5 F_\lambda^{\text{planet}}}\right) \tag{1.6}$$

Different wavelengths probe different layers of the atmosphere. In regions where the temperature decreases with height, low-opacity wavelengths allow radiation to escape from deeper, hotter layers, while strong molecular bands probe higher, cooler layers. By combining brightness temperatures across wavelengths, it is possible to reconstruct the planet's P–T profile. Observations of exoplanet daysides have revealed a variety of atmospheric structures, including thermal inversions (layers where temperature increases with altitude, see Section 2.1) observed in ultra-hot Jupiters such as WASP-18b, WASP-33b, CoRoT-2b and WASP-76b (Sheppard et al., 2017, Snellen et al., 2010a, Yan et al., 2023).

Besides thermal emission, a planet can also reflect and scatter incoming stellar light, particularly at optical wavelengths. The strength of this reflected component depends on atmospheric composition, cloud coverage, and albedo, and it can dominate in cooler planets where thermal emission is weak. Reflectance spectroscopy has been used to study scattering processes and estimate planetary albedos, providing complementary information on atmospheric properties (Madhusudhan et al., 2014, Martins et al., 2015).

1.2.3 The cross-correlation method

A popular method used to detect and study exoplanet atmospheres is the cross-correlation method. This method consists of generating the cross-correlation function (CCF) between

the observed spectrum and a template, thus evaluating how well the two match. The template can contain the spectral contribution of a given chemical species in order to verify if it exists in the spectrum of a planet's atmosphere. Depending on whether the CCF is calculated on the planet's rest frame (PRF) or on the stellar rest frame (SRF), we expect a detection to show itself as a peak at 0 or at the value of the planet's radial velocity (RV), respectively. Figure 1.7 demonstrates how the CCF is obtained for a single spectrum. Equations (1.7) and (1.8) show the discrete and continuum implementation of the cross-correlation between a spectrum $F(\lambda)$ and a template $T(\lambda)$ shifted by RV.

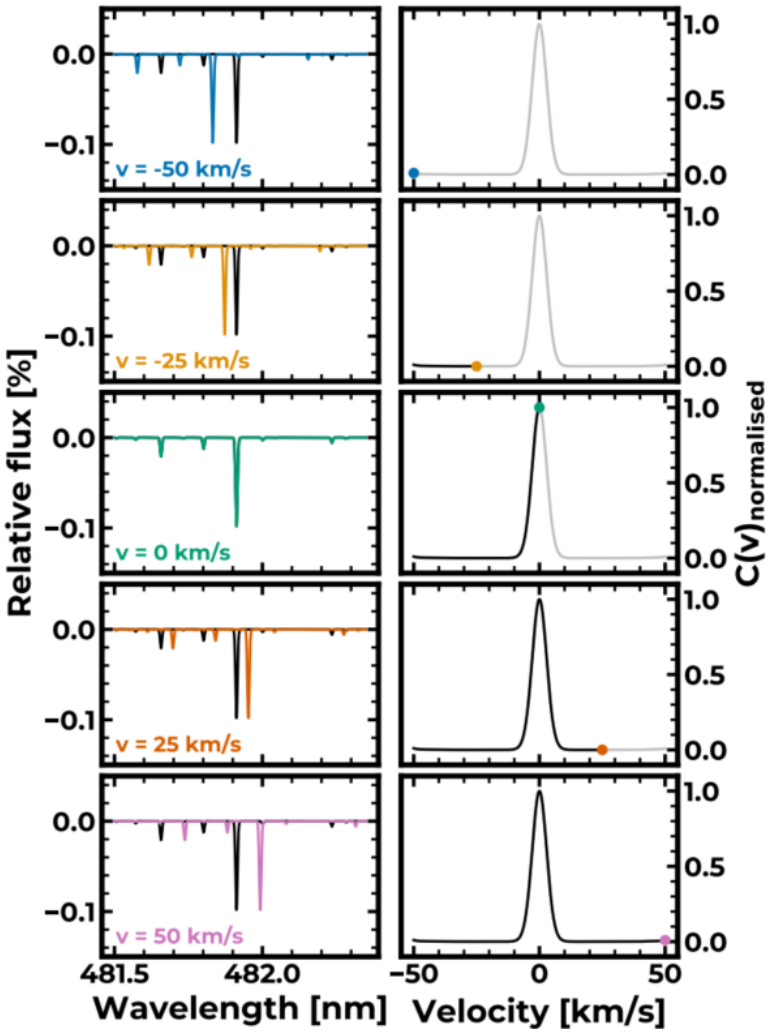

FIGURE 1.7: Figure 4.1 from Prinoth (2025), demonstrating the cross-correlation method applied to spectroscopy.

$$CCF(RV) = \sum_{i=0}^{N} F(\lambda_i) T(\lambda_i, RV) \tag{1.7}$$

$$CCF(RV) = \int_{0}^{+\infty} F(\lambda)\, T(\lambda, RV)\, d\lambda \tag{1.8}$$

The cross-correlation method has become very interesting in the study of atmospheres, mostly due to its capability of enhancing the signal of very faint absorption or emission lines in spectra. Planetary lines are often much smaller than the stellar components that dominate an exposure, and even if the removal of the stellar contribution were flawless, these lines would still be too faint and smaller than the noise to be individually identified. The cross-correlation method helps by comparing every small line in the spectra with the template and effectively combining their signal. This method was first applied to exoplanetary atmospheres by Snellen et al. (2010b) to detect CO on the atmosphere of HD 209458 b; however, it was originally applied by Simkin (1974) for the study of stars and galaxies, even though the CCF had been well known to engineers long before. Since then, it is widely used to detect molecules like TiO (e.g. Nugroho et al., 2017, Prinoth et al., 2023) and H_2O (e.g. Birkby et al., 2013, 2017) and atoms, such as Fe (e.g. Hoeijmakers et al., 2024, Costa Silva, A.R. et al., 2024, Prinoth et al., 2025) and Ca (e.g. Hoeijmakers et al., 2024, Merritt et al., 2021).

The method comes with pitfalls such as the loss of information on individual spectral lines, a necessary trade-off for the enhanced S/N, and its strong dependence on the chosen template. The template is a model spectrum based on molecular or atomic line lists at assumed temperatures and pressures; if these line lists are inaccurate, the signal of a poorly modeled species may be suppressed (de Regt et al., 2022).

We have addressed the potential risks and benefits of implementing this method, emphasising the importance of careful usage and interpretation.

1.3. Manuscript Structure

This manuscript will present my work on the study of the atmosphere of the planet WASP-76 b via emission spectroscopy. In Chapter 2 we introduce the planet, the observations that make this work possible and the instrument that collected them. In Chapter 3 we guide the reader through the data pre-processing, including correction for the Earth's atmosphere in Section 3.1, the continuum normalisation in Section 3.2, outlier handling in Section 3.3, rest-frame alignments in Section 3.4, and finally the removal of the stellar contribution and extraction of the planet's spectrum in Section 3.5. Once we extract the planet's spectrum from the data we can move on to its analysis using the cross-correlation method, for which we need a template of the species of interest: neutral iron, Fe I. This is done in Chapter 4. Finally, in Chapter 5 we draw the conclusions and final thoughts of the work demonstrated in this dissertation.

Chapter 2

WASP-76 b observations

To properly frame the analysis that follows, this Chapter introduces the study target, WASP-76 b, in more depth and presents the ESPRESSO observations that made our study possible. The ultra-hot Jupiter (UHJ) WASP-76 b serves as an ideal laboratory for studying atmospheres in scorching environments. The first section provides an overview of the planet's known properties and its relevance within the broader class of UHJ. The second outlines the spectroscopic data obtained with ESPRESSO.

2.1. Planet Overview

WASP-76 b is a representative member of the ultra-hot Jupiter population, a class of gas giants with masses and radii comparable to Jupiter, but orbiting extremely close to their host stars and subjected to intense stellar irradiation, which raises their equilibrium temperature above 2000 K. WASP-76 A, its host star, is an F7-type star with an apparent magnitude of $V = 9.52$ mag (Høg et al., 2000, West et al., 2016), an effective temperature of $T_{\rm eff} = 6329 \pm 65$ K and a radius $R_\star = 1.458 \pm 0.021 R_\odot$ (Ehrenreich et al., 2020). WASP-76 b completes one orbit every 1.81 days at a distance of 0.033 AU from its star, placing it in a regime of extreme irradiation. Due to this tight orbit, the planet is expected to be tidally locked, with one hemisphere permanently facing the star and the other in perpetual darkness. This results in a pronounced thermal difference: the dayside reaches temperatures of $T_{\rm day} = 2623 \pm 20$ K (Demangeon et al., 2024), significantly higher than the estimated equilibrium temperature of $T_{\rm eq} = 2228 \pm 122$ K (Ehrenreich et al., 2020), while the nightside remains substantially cooler with a temperature of $T_{\rm night} = 1670^{+20}_{-23}$ K (Demangeon et al., 2024). With a radius of 1.854 $R_{\rm Jup}$ and a mass of $0.894 M_{\rm Jup}$ (Ehrenreich et al., 2020), the planet is also one of the most inflated hot Jupiters observed to date. A summary of

the star's and the planet's key physical and orbital parameters can be found in Tables 2.1 and 2.2, respectively.

UHJs like WASP-76 b provide a valuable testbed for studying planetary atmospheres under extreme conditions. The intense stellar irradiation on the dayside produces physical environments with temperatures similar to those found in low mass stellar photospheres. At such high temperatures, often exceeding 2500 K, most molecular species are thermally dissociated, and the atmosphere becomes dominated by neutral and ionised atomic species (Parmentier et al., 2018, Hoeijmakers et al., 2019). In contrast, the much cooler nightside allows for molecular recombination and possibly even condensation processes. This thermal contrast gives rise to a pronounced gradient in temperature and atmospheric composition.

One of the key features predicted in the atmospheres of UHJs is the presence of thermal inversion layers - regions in which temperature increases with altitude (Haynes et al., 2015, Evans et al., 2017, Pino et al., 2020, Yan, F. et al., 2020). Hints of a thermal inversion in WASP-76 b have already been reported in previous studies (Edwards et al., 2020, May et al., 2021, Fu et al., 2021), and were later confirmed through near-infrared CRIRES+ observations by Yan et al. (2023). These inversions arise when stellar radiation is absorbed efficiently at low pressures, heating the upper atmosphere. Early theoretical work proposed Titanium Oxide (TiO) and Vanadium Oxide (VO) as the primary high-altitude absorbers responsible for driving such inversions (Hubeny et al., 2003, Fortney et al., 2008), due to their strong visible-wavelength opacities. However, while TiO and VO have been identified in some planets, including tentatively in WASP-76 b (Edwards et al., 2020, Fu et al., 2021, Tsiaras et al., 2018, Changeat et al., 2022, Pelletier et al., 2023, Maguire et al., 2024), their role in creating thermal inversions remains uncertain. These species may be depleted through condensation on the cooler nightside, due to their high condensation temperatures, making their overall contribution highly uncertain. More recent modeling by Lothringer et al. (2018) has highlighted the role of neutral atomic species - particularly Fe I, Mg I, and Ca I - in shaping UHJ temperature structures. At the high temperatures typical of these atmospheres, these atoms absorb stellar light in the optical and near-UV, and can create temperature inversions even without molecules like TiO or VO. Their influence is enhanced by continuous opacity from H^- ions.

Starting with the initial discovery of WASP-76 b by West et al. (2016), followed by tentative or low-resolution detections of H_2O, TiO, and VO in transmission spectra (Tsiaras

et al., 2018, Fisher and Heng, 2018, Žák et al., 2019, Seidel et al., 2019), and then the first high-resolution detections of neutral sodium (Na I; Žák et al. 2019, Seidel et al. 2019) and neutral iron (Fe I; Ehrenreich et al. 2020), several other atomic, ionic, and molecular species have since been reported in the atmosphere of WASP-76 b, as summarised in Tables 2.3 and 2.4.

Observationally, Fe I has been detected in several UHJs through both transmission and emission spectroscopy. In transmission, Fe I absorption has been identified in the terminator regions (Ehrenreich et al., 2020, Hoeijmakers et al., 2018, Bourrier, V. et al., 2020, Borsa, F. et al., 2022). Emission spectroscopy has confirmed the presence of Fe I on the dayside in multiple planets (Pino et al., 2020, Yan, F. et al., 2020, Scandariato et al., 2023, Nugroho et al., 2020). Ehrenreich et al. (2020) reported an asymmetric Fe I signature in transmission spectra of WASP 76 b, observed on the evening limb but absent on the morning limb, a result that has been independently confirmed in subsequent studies (Pelletier et al., 2023, Kesseli and Snellen, 2021, Kesseli et al., 2022). Among other interpretations, these results have been suggested as evidence that Fe I condenses when crossing the cooler nightside, while remaining in gaseous form on the hotter dayside. If this is the case, Fe I should be observable in emission from the dayside hemisphere. Motivated by this scenario, Costa Silva, A.R. et al. (2024) confirmed the presence of Fe I on the dayside of WASP-76 b using high-resolution emission spectroscopy and detected a blueshift in the Fe I emission signature. In this work, our objective is to reproduce the results of Costa Silva, A.R. et al. (2024) and investigate the dynamics of Fe in the atmosphere of WASP-76 b.

Table 2.1: Stellar parameters of the WASP-76 system

Parameter	**Symbol (unit)**	**Value**	**Reference**
Right ascension	RA	$01^{h}\ 46^{m}\ 31.9^{s}$	Gaia Collaboration (2020)
Declination	Dec	$+02^{\circ}\ 42'\ 02.0''$	Gaia Collaboration (2020)
V magnitude	$V_{\rm mag}$ (mag)	9.52 ± 0.03	Høg et al. (2000)
Spectral type	–	F7	West et al. (2016)
Effective temperature	$T_{\rm eff}$ (K)	6329 ± 65	Ehrenreich et al. (2020)
Radius	$R_{\star}$ ($R_{\odot}$)	1.458 ± 0.021	Ehrenreich et al. (2020)
Mass	$M_{\star}$ ($M_{\odot}$)	1.756 ± 0.071	Ehrenreich et al. (2020)
Surface gravity	$\log g$ (cgs)	4.196 ± 0.106	Ehrenreich et al. (2020)
RV semi-amplitude	$K_{\star}$ (m s^{-1})	$116.02^{+1.29}_{-1.35}$	Ehrenreich et al. (2020)
Systemic velocity	$v_{\rm sys}$ (km s^{-1})	Epoch I: -1.2106 ± 0.0002	This work
		Epoch II: -1.2129 ± 0.0003	This work
		Epoch III: -1.2073 ± 0.0002	This work
		Epoch IV: -1.2108 ± 0.0003	This work

TABLE 2.2: Planetary parameters of WASP-76 b

Parameter	Symbol (unit)	Value	Reference
Radius	R_p (R_{Jup})	$1.854^{+0.077}_{-0.076}$	Ehrenreich et al. (2020)
Mass	M_p (M_{Jup})	$0.894^{+0.014}_{-0.013}$	Ehrenreich et al. (2020)
Surface gravity	g_p (m s^{-2})	6.4 ± 0.5	Ehrenreich et al. (2020)
Inclination	i (deg)	$89.623^{+0.014}_{-0.013}$	Ehrenreich et al. (2020)
Semi-major axis	a (AU)	0.0330 ± 0.0002	Ehrenreich et al. (2020)
Orbital period	P (days)	$1.80988198^{+0.00000056}_{-0.00000064}$	Ehrenreich et al. (2020)
Mid-transit time	T_c (BJD)	$58080.626165^{+0.0000367}_{-0.0000418}$	Ehrenreich et al. (2020)
RV semi-amplitude	K_p (km s^{-1})	196.52 ± 0.94	Ehrenreich et al. (2020)
Equilibrium temperature	T_{eq} (K)	2228 ± 122	Ehrenreich et al. (2020)
Dayside temperature	T_{day} (K)	2623 ± 20	Demangeon et al. (2024)

TABLE 2.3: Summary of atomic, ionic, and molecular detections in the atmosphere of WASP-76 b reported in the literature.

Chemical species	Reference
Ba II	[1], [2]
Ca I	[2]
Ca II	[1], [2], [3], [4], [5], [6], [7]
Co I	[6]
Cr I	[1], [2], [6], [7]
Fe I	[1], [2], [3], [6], [7], [8], [9], [10], [11]
Fe II	[2]
H I	[1], [2], [6]
He I	[4], [12], [13]
K I	[2], [3], [6], [7]
Li I	[1], [2], [3], [6], [7]
Mg I	[1], [2], [3], [6], [11]
Mn I	[1], [2], [3], [6]
Na I	[1], [2], [3], [5], [6], [7], [14], [15], [16], [17], [18]
Ni I	[2], [6]
O I	[2]
Sr II	[6]
V I	[1], [2], [6], [7]
CO	[19], [20], [21]
H_2O	[19], [20], [21], [22], [23], [24], [25], [26], [27]
HCN	[22]
OH	[21], [27], [28]
TiO	[19], [23], [26]
VO	[2], [11], [23], [25]

References. (1) Azevedo Silva et al. (2022); (2) Pelletier et al. (2023); (3) Tabernero et al. (2021); (4) Casasayas-Barris et al. (2021); (5) Deibert et al. (2021); (6) Kesseli et al. (2022); (7) Deibert et al. (2023); (8) Ehrenreich et al. (2020); (9) Kesseli and Snellen (2021); (10) Costa Silva, A.R. et al. (2024); (11) Maguire et al. (2024); (12) Lampón et al. (2023); (13) Masson et al. (2024); (14) Seidel et al. (2019); (15) Žák et al. (2019); (16) Seidel et al. (2021); (17) Kawauchi et al. (2022); (18) Sicilia et al. (2025); (19) Fu et al. (2021); (20) Yan et al. (2023); (21) Weiner Mansfield et al. (2024); (22) Sánchez-López et al. (2022); (23) Tsiaras et al. (2018); (24) Fisher and Heng (2018); (25) Changeat et al. (2022); (26) Edwards et al. (2020); (27) Gandhi et al. (2024); (28) Landman et al. (2021).

TABLE 2.4: Summary of atmospheric detections in WASP-76 b from the literature.

Paper	Species Detected	Instrument	Resolution	Method (Spectroscopy)
Tsiaras et al. (2018)	H_2O; tentative: TiO, VO	HST / WFC3	Low	Transmission
Fisher and Heng (2018)	H_2O	HST / WFC3	Low	Transmission
Seidel et al. (2019)	Na I	HARPS	High	Transmission
Žák et al. (2019)	Na I	HARPS	High	Transmission
Ehrenreich et al. (2020)	Fe I	VLT / ESPRESSO	High	Transmission
Edwards et al. (2020)	TiO, H_2O	HST / WFC3	Low	Transmission and Emission
Kesseli and Snellen (2021)	Fe I	HARPS	High	Transmission
Tabernero et al. (2021)	Li I, Na I, Mg I, Ca II, Mn I, K I, Fe I	VLT / ESPRESSO	High	Transmission
Fu et al. (2021)	H_2O, CO, TiO	HST; Spitzer	Low	Transmission and Emission
Seidel et al. (2021)	Na I	HARPS; VLT / ESPRESSO	Mixed	Transmission
Deibert et al. (2021)	Ca II, Na I	GRACES	High	Transmission
Casasayas-Barris et al. (2021)	Ca II; upper limit: He I	CARMENES	High	Transmission
Landman et al. (2021)	OH	CARMENES	High	Transmission
Kesseli et al. (2022)	Li I, Na I, Mg I, Ca II, V I, Cr I, Mn I, Fe I, Ni I, Sr II; tentative: H I, K I, Co I	VLT / ESPRESSO	High	Transmission
Sánchez-López et al. (2022)	H_2O, HCN	CARMENES	High	Transmission
Kawauchi et al. (2022)	Na I	Subaru/HDS	High	Transmission
Changeat et al. (2022)	H_2O, VO	HST / WFC3 G141; Spitzer	Low	Transmission and Emission
Azevedo Silva et al. (2022)	Ba II, Ca II, Cr I, Fe I, H I, Li I, Mg I, Mn I, Na I, V I	VLT / ESPRESSO	High	Transmission
Yan et al. (2023)	H_2O, CO	CRIRES +	High	Emission
Lampón et al. (2023)	He I	CARMENES	High	Transmission
Pelletier et al. (2023)	H I, Ba II, Ca I, Ca II, Cr I, Fe I, K I, Li I, Mg I, Mn I, Na I, Ni I, V I; tentative: Fe II, O I, VO	MAROON-X	High	Transmission
Deibert et al. (2023)	Ca II, Fe I, Na I; tentative: Cr I, K I, Li I, V I	GRACES	High	Transmission
Costa Silva, A.R. et al. (2024)	Fe I (blueshifted)	VLT / ESPRESSO	High	Emission
Maguire et al. (2024)	VO, Fe I, Mg I	VLT / ESPRESSO	High	Transmission
Gandhi et al. (2024)	OH, H_2O	CARMENES, HST/WFC3, Spitzer	Mixed	Transmission
Weiner Mansfield et al. (2024)	H_2O, CO, OH	Gemini-S/IGRINS	High	Transmission
Masson et al. (2024)	tentative: He I	CFHT / SPIROU	High	Transmission
Sicilia et al. (2025)	Na I	HARPS-N	High	Transmission

2.2. ESPRESSO spectroscopic data

The observations analysed in this work were obtained with the Echelle SPectrograph for Rocky Exoplanet and Stable Spectroscopic Observations (ESPRESSO), a high-resolution spectrograph of ESO's Very Large Telescope (VLT) (Pepe et al., 2021), installed at the Paranal Observatory in Chile. ESPRESSO operates in the optical range (380–788 nm) and can be used with one or all four Unit Telescopes (UT), achieving spectral resolutions between $R \sim 70\,000$ and $R \sim 190\,000$, depending on the configuration.

ESPRESSO offers several observing configurations designed to balance spectral resolution and light-collecting efficiency, depending on the scientific goals. These include Ultra-High Resolution (UHR), High Resolution (HR), and Medium Resolution (MR) modes. The key difference between these modes lies in the fibre size and telescope setup: UHR uses a 12.7 mm fibre with one UT to achieve the highest resolution ($R \sim 190\,000$); HR uses a 25.4 mm fibre with one UT to provide a resolution of $R \sim 140\,000$; and MR uses a 25.4 mm fibre for each UT, combining the light from all four and offering a lower resolution ($R \sim 70\,000$) but significantly increased photon throughput. Although each UT feeds light of the target star into a single science fibre (Fibre A), ESPRESSO has a dual-fibre system and the spectrograph always operates with two input fibres (A and B) in parallel, projecting their spectra side-by-side onto the detector. This dual-fibre design allows simultaneous acquisition of science and reference frames: the sky or a wavelength calibration source (Fabry-Perot or Laser Frequency Comb).

ESPRESSO supports different detector binning configurations, which define how many adjacent CCD pixels are read out together during data acquisition. In an N $\times$ M binning scheme, N pixels are combined in the spatial (cross-dispersion) direction and M in the spectral (dispersion) direction. This reduces readout noise by a factor of N $\times$ M, as the signal from all binned pixels is read in a single operation rather than individually. Binning is therefore particularly advantageous for low signal-to-noise ratio (S/N) observations where readout noise is a limiting factor. However, the trade-off is reduced spatial sampling (by N) and reduced spectral sampling (by M), which can limit resolution or affect precision in highly sampled spectra.

For WASP-76 b, ESPRESSO is particularly well suited to detect atomic and ionic features in the planetary spectrum, thanks to its stability and high resolving power. For our observations of WASP-76 b, the instrument was operated in HR21 mode, which uses one UT with the 25.4 mm fibre and 2×1 binning, meaning that two pixels were combined in the spatial

direction while spectral sampling was preserved. This configuration yields a spectral resolution of approximately $R \sim 140\,000$ covering the visible wavelength range from 3800 to 7880 Å. The observations were carried out, with the sky in the B fibre, during four visits covering orbital phases shortly before and after secondary transit, when the dayside of the planet is in view, as part of the programmes 1104.C-0350(U) and 110.24CD.004 of the Guaranteed Time Observation (GTO). These phases are ideal for studying thermal emission and for searching for emission lines originating from the hot dayside atmosphere, as the planet is fully illuminated. In particular, atomic and ionic species present in the upper atmosphere can emit in the optical as they are excited by intense stellar irradiation.

The data consists of the two epochs before the secondary transit taken on 14th October 2022 and on 9th September 2021 and the two epochs after the secondary transit taken on 2nd September 2021 and 18th October 2022, corresponding, respectively, to epochs I, II, III and IV, ordered by increasing orbital phase. The dataset consists of 74 spectra of the star and planet before the eclipse and 74 spectra of the star and planet after the eclipse, resulting in a total of 148 high-resolution spectra. Each spectrum corresponds to an exposure time of 300s and the total spectra of one night corresponds to an observing time between 3 and 4 hours. The data files used correspond to the S1D spectra observed with fibre A that was pointed at our target, with the sky background captured by fibre B subtracted. The S1D spectra files provide one-dimensional, wavelength-calibrated and flux-calibrated spectra with merged échelle orders. ESPRESSO is an échelle spectrograph, meaning it uses a cross-dispersed grating to separate incoming starlight into many overlapping spectral orders, which are then spatially separated on the detector by a second prism or grating. This design allows simultaneous coverage of a broad wavelength range at high resolving power. The result is a spectrum distributed over roughly 85 individual orders, each corresponding to a narrow segment of the full optical range — the S1D format collapses this information into a continuous 1D spectrum for each exposure.

More information about these observations can be found summarized in Table 2.5. The orbital phases covered by the observations are schematized in Figure 2.1. To evaluate the quality and consistency of the observational conditions across the four ESPRESSO epochs, we analysed the variation of key parameters as a function of orbital phase, as shown in Figure 2.2. This includes the seeing, radial velocity of the host star, signal-to-noise ratio (S/N) (taken from order 106 of ESPRESSO, around the wavelength 5800 Å), airmass, integrated water vapour, and relative humidity. Each parameter is plotted individually for epochs I through IV, highlighting the stability and atmospheric transparency of each

night. In particular, the airmass remained low (typically < 1.5), and the S/N values were consistently above 60 in all datasets, supporting the high quality of the spectra. The integrated water vapour and humidity levels, which are important for telluric correction, also remained relatively stable within each night, with epoch IV being the one that shows more variability in humidity through the night.

TABLE 2.5: Overview of observational logs for each night.

Epoch	Night	VLT Unit	# spectra	Exposure time	Phase coverage	S/N range(*)	Airmass range	Seeing (") range	MJD Start
I	2022-10-14	UT1	39	300 s	0.34-0.42	61-91	1.126-1.445	0.43-1.05	59867.09828268
II	2021-09-09	UT2	35	300 s	0.39-0.47	77-95	1.126-1.337	0.40-0.88	59467.21008223
III	2021-09-02	UT1	35	300 s	0.54-0.61	62-74	1.126-1.301	0.43-0.80	59460.23621672
IV	2022-10-18	UT1	39	300 s	0.54-0.62	72-88	1.127-1.491	0.60-1.15	59871.08151808

Notes. (*) Values taken from order 106 of ESPRESSO, at ∼5800 Å.

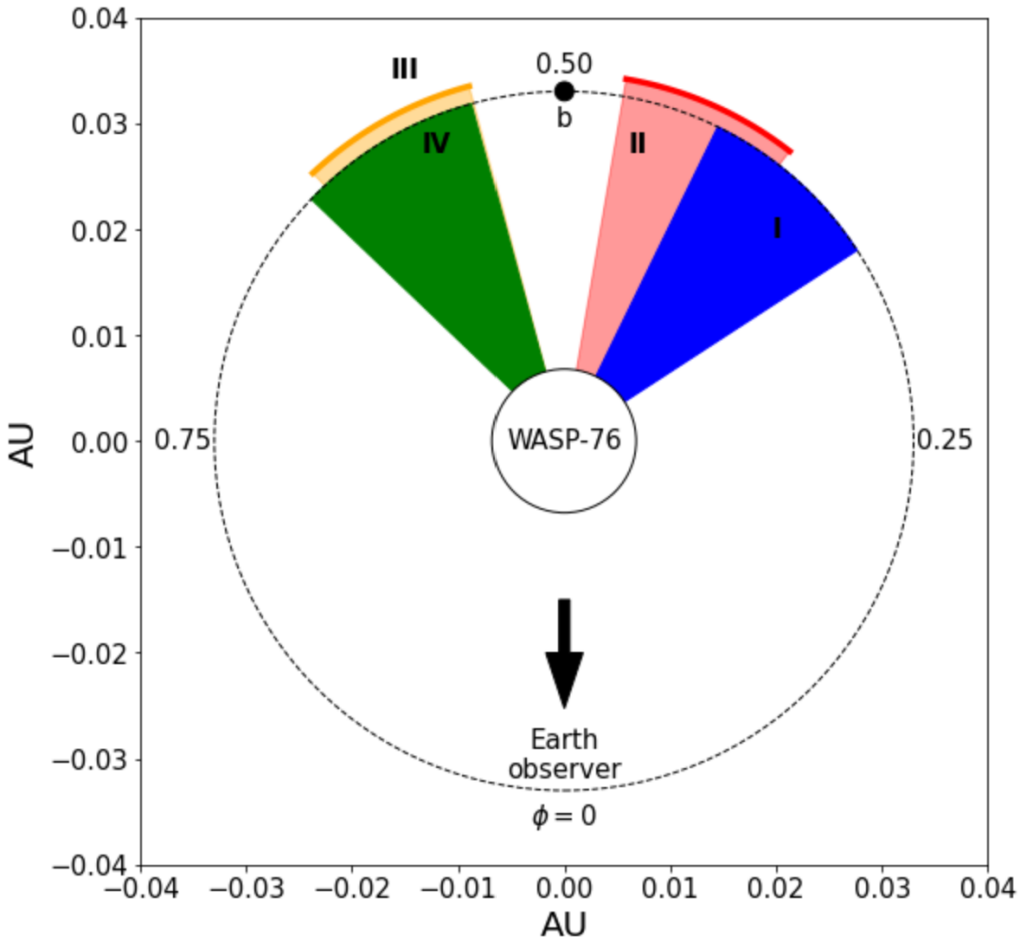

FIGURE 2.1: Orbital diagram of WASP-76 b indicating the observed epochs and corresponding orbital phases (ϕ). Adapted from Costa Silva, A.R. et al. (2024).

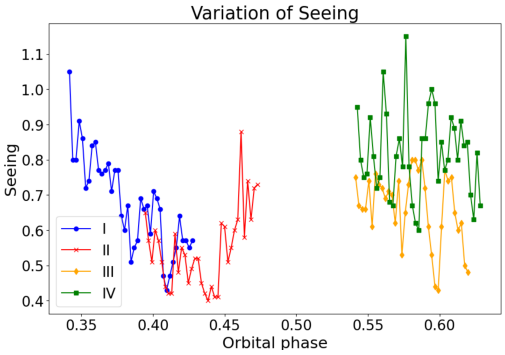

(A) Seeing

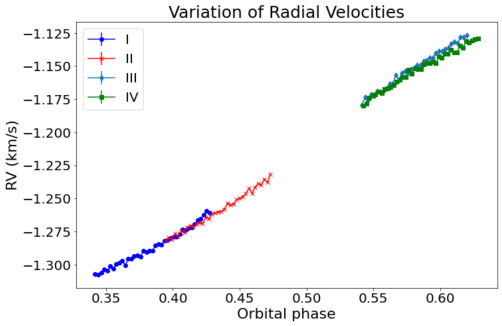

(B) Systemic radial velocity of the star

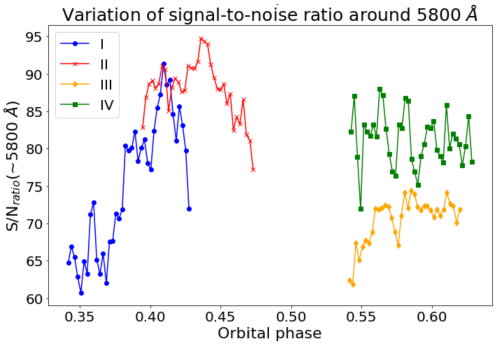

(C) Signal-to-noise ratio around 5800 Å (spectral order 106)

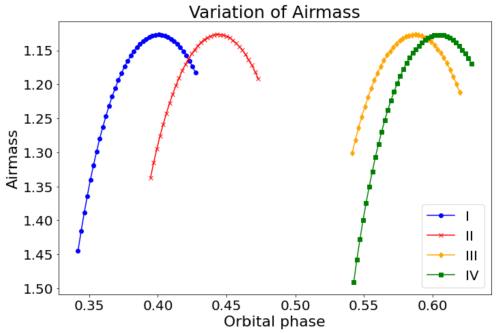

(D) Airmass

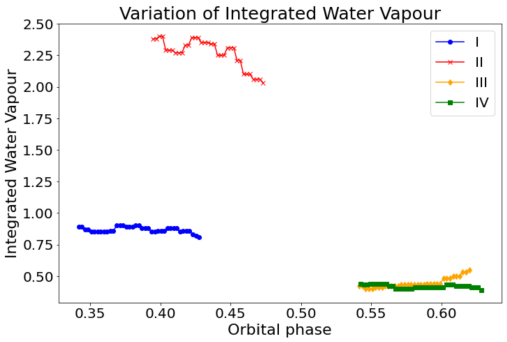

(E) Integrated water vapour

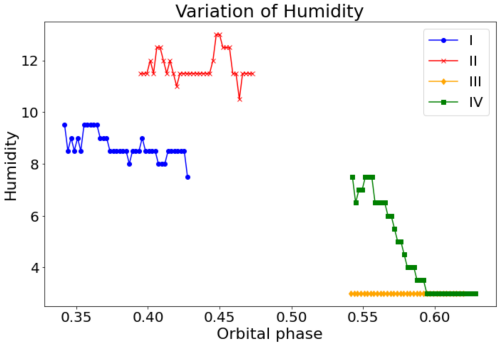

(F) Relative humidity (in %)

FIGURE 2.2: Diagnostic plots showing the variation of key observational parameters during the four ESPRESSO visits, as a function of orbital phase.

Chapter 3

Data Reduction

Ground-based spectroscopic observations of exoplanets are subject to numerous sources of contamination, both astrophysical and instrumental. The atmosphere of the Earth imprints strong absorption features on the data, requiring precise telluric correction techniques. In addition, instrumental effects, stellar spectral features, and Doppler shifts due to the orbital motion of the system must be carefully accounted for to isolate the faint signal of the planet.

This chapter outlines the data reduction and correction procedures applied to the ESPRESSO observations of WASP-76 b. The goal is to extract the high-resolution emission spectrum of the planet's dayside with minimal contamination. The raw science frames were first processed using the standard ESPRESSO Data Reduction System (DRS, version 3.0.0, Pepe et al. (2021)), producing S1D spectra corrected for instrumental effects and aligned to the Solar-System's barycentric rest frame. From this point, we implemented a custom reduction pipeline consisting of seven main steps, including telluric correction with Molecfit (Smette et al. (2015), Kausch et al. (2015)), continuum normalisation, outlier rejection, systemic velocity determination, transformation to the stellar rest frame, stellar template subtraction, and final shifting to the planet rest frame.

Each step is described in detail in the following sections.

3.1. Telluric correction: Molecfit

The removal of telluric absorption lines is a crucial step in the analysis of ground-based astronomical spectra. These lines, imprinted by molecules in Earth's atmosphere (primarily H_2O, O_2, and CO_2), can overlap with spectral features of interest and severely limit the detection of exoplanetary signals. To correct for this contamination, we employed `Molecfit` (Smette et al., 2015, Kausch et al., 2015), a radiative transfer tool developed by ESO that

models and removes telluric absorption features from observed spectra using synthetic transmission spectra of the Earth's atmosphere.

The software combines a line-by-line radiative transfer code (LBLRTM; Clough et al. (2005)), a molecular line database, atmospheric profiles, and instrumental line spread function (LSF) modelling. Atmospheric profiles are generated by merging a standard climate-based profile for the observatory site with local meteorological data and Global Data Assimilation System (GDAS) profiles retrieved for the observation time. This ensures accurate vertical distributions of temperature, pressure, and humidity. `Molecfit` operates on user-defined wavelength ranges ("inclusion regions" or "fitting ranges" - `WAVE INCLUDE` in the interface) that contain strong telluric lines but minimal intrinsic stellar or instrumental features. The fitting process adjusts molecular column densities and the parameters of the LSF and its accuracy depends on the amount of continuum level present in the inclusion regions. Regions affected by stellar or instrumental artefacts can be excluded to avoid biasing the fit ("exclusion regions"). Once the best-fit parameters are determined, `Molecfit` produces a high-resolution model of the telluric transmission across the entire spectral range, which is then used to divide the observed spectrum and remove atmospheric absorption. This approach achieves accuracies comparable to, or better than, those obtained with traditional telluric standard stars, with typical residuals below 2% of the continuum for unsaturated lines (Smette et al., 2015). Its versatility allows application to a wide range of instruments operating between 0.3 and 30 μm, making it well suited for high-resolution exoplanet spectroscopy.

We focused the telluric correction on the molecules H_2O and O_2, which dominate the optical part of the spectrum. For this purpose, we used four inclusion regions, corresponding to spectral intervals where the telluric absorption lines of these molecules are deepest, as identified on Molecfit's Graphic User Interface (GUI) (see Figure 3.1). These intervals were initially provided by the Molecfit *auto-molecule algorithm* (or `auto-molecule`), which selects regions where the atlas spectrum of a molecule shows absorption features deeper than 2% of the continuum. The atlas spectra of H_2O and O_2 are overplotted in Figure 3.1, confirming that the automatically chosen regions indeed correspond to strong telluric features. We then refined these regions by slightly restricting the fitting intervals, as advised in Appendix A of the MOLECFIT Reflex Tutorial, as well as broadening one region in two of the epochs to include more continuum, which improves the accuracy of the fit. Within each inclusion region, we defined exclusion sub-ranges to mask strong stellar features, ensuring that the fit was driven only by telluric lines. The final configuration

of inclusion and exclusion regions is shown in Figure 3.2. Besides the wavelength region selection for the fitting, other parameters worth defining are the continuum polynomial order, for which we used a 4^{th} degree polynomial and the profile that determines the LSP, for which we used the default Gaussian profile with an initial value of one pixel for the Full Width at Half Maximum (FWHM). The parameter tuning and region selection was performed for the first observation of each night. The resulting `molecfit` recipe was then applied to the subsequent observations of the corresponding night starting from the best fit parameters of the first spectrum to achieve convergence faster than if we started from the default ones. For each observation, the outputs consist of FITS files containing the telluric-corrected spectrum, the corresponding transmission spectrum, and the best-fit model parameters. Figures 3.3 and 3.4 illustrate one of the original spectra with the corresponding telluric-corrected spectrum overplotted for comparison. In Figure 3.3 we can observe that around the wavelength regions 6865 - 6910 Å and 7590 - 7680 Å the telluric-corrected spectrum shows artificially large flux values. This occurs because these regions are heavily saturated: the flux in the original spectrum is nearly zero, which makes it difficult for `molecfit` to perform a reliable correction. We later mask these regions due to the uncertain quality of the telluric correction.

The original spectra provided by the ESPRESSO pipeline includes associated uncertainties arrays. Since the telluric correction is performed by dividing the flux by the transmission spectrum of the Earth's atmosphere from `molecfit`, the corresponding uncertainties were propagated in the same way. This is, the error arrays of the original spectra were divided by the corresponding transmission spectrum.

Due to intrinsic errors with the usage of the include and exclude regions function of `molecfit`, we could not reduce all the data, so the data previously reduced by Costa Silva, A.R. et al. (2024) was used instead.

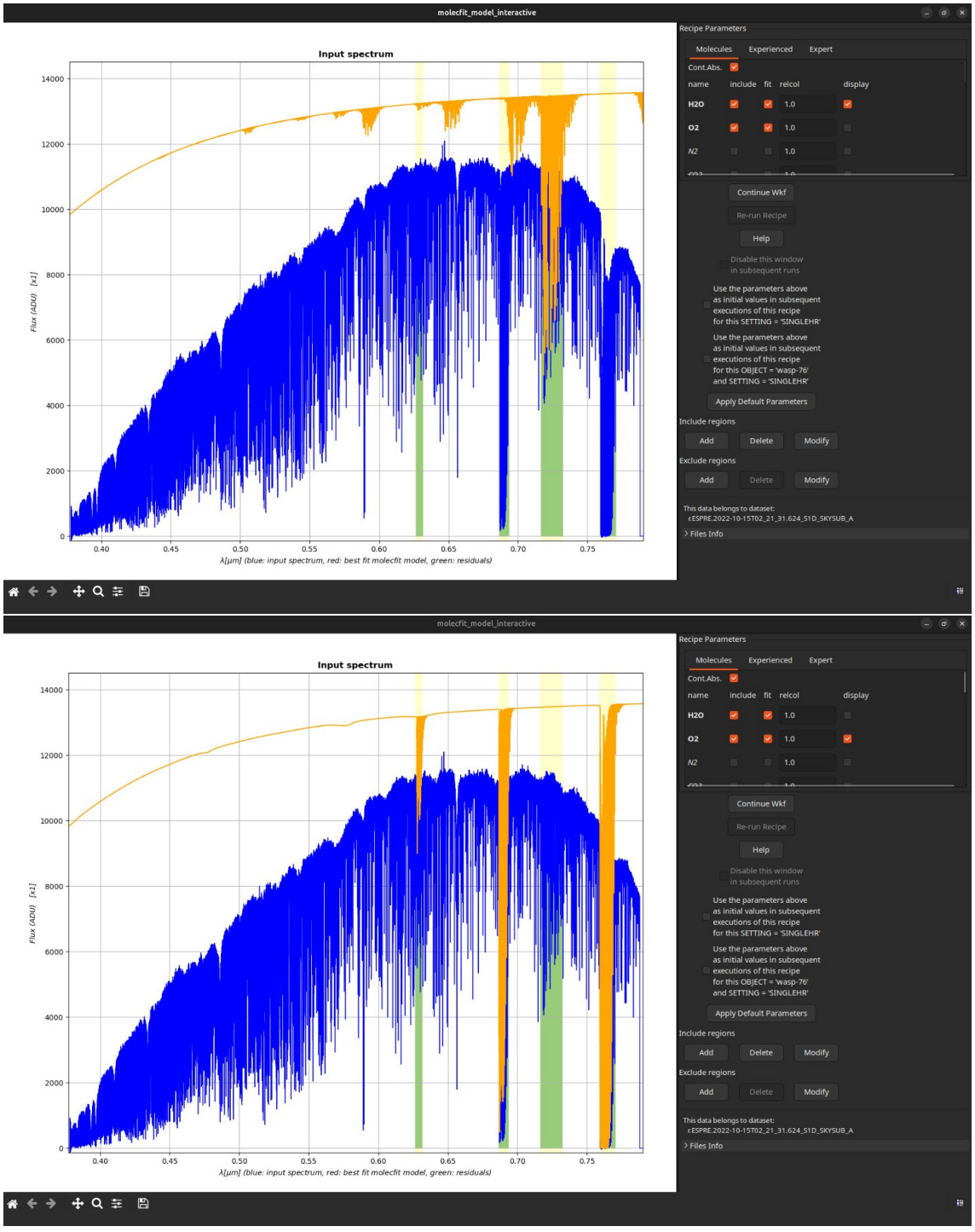

FIGURE 3.1: Molecfit's GUI displaying one of our input spectra in blue, the inclusion regions in the shaded green area and the atlas spectra of the molecules H_2O (top panel) and O_2 (bottom panel) in orange. The yellow shaded regions are not relevant for the purpose of this manuscript.

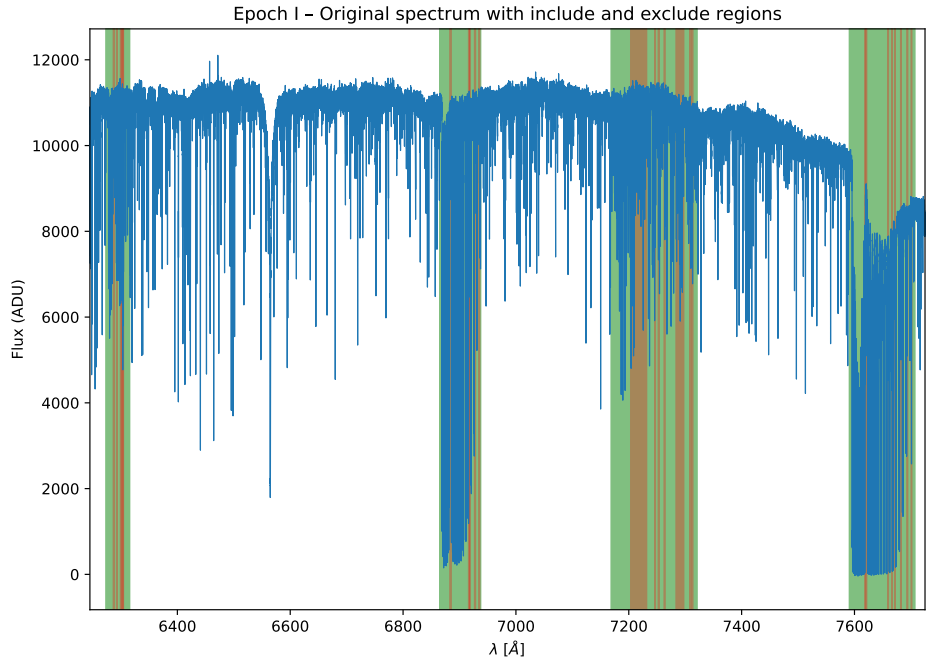

FIGURE 3.2: Section of the first spectrum (before correction) of Epoch I, in blue, with the final configuration of the inclusion, in green, and exclusion, in red, regions used for the telluric correction.

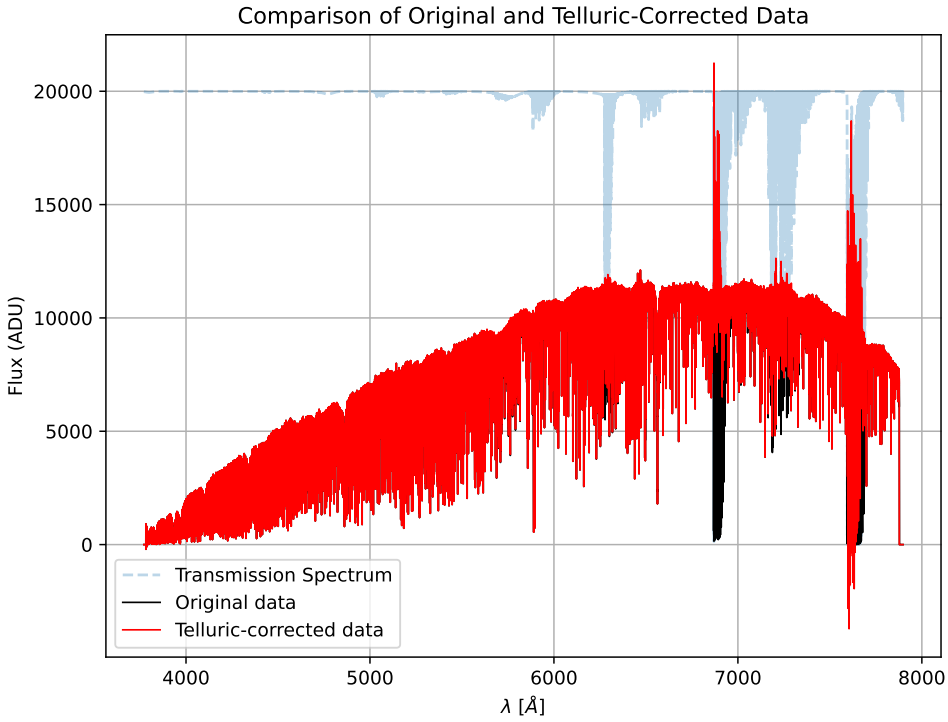

FIGURE 3.3: Comparison between one of the original spectra (black) and its telluric-corrected version (red). The best-fit transmission spectrum from `molecfit` is also shown (blue dashes), scaled for visibility.

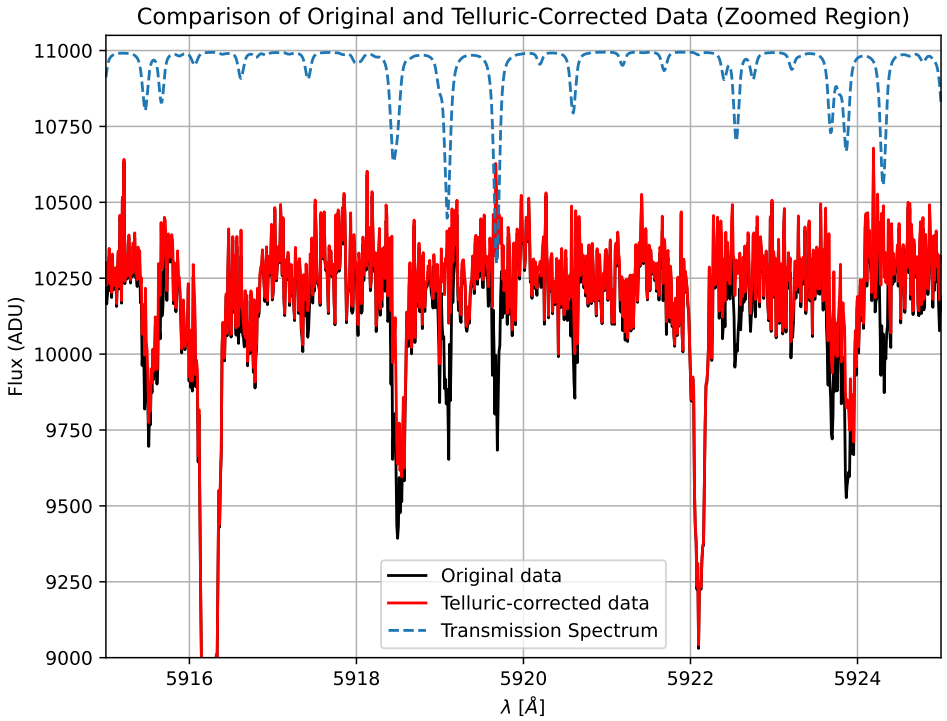

FIGURE 3.4: Zoom into the 5915–5925 Å region, showing one of the original spectra (black), its telluric-corrected version (red), and the best-fit transmission spectrum (blue dashes). The correction successfully removes most telluric absorption features, though some residuals remain in saturated regions.

3.2. Continuum Normalisation (Spectra Normalization Tool)

In spectroscopy, the continuum is the smooth background flux of a spectrum, produced by blackbody radiation, or thermal emission, from dense media such as stellar photospheres, upon which narrower absorption and emission features are superimposed. In photographs, the continuum appears as a rainbow-coloured strip, while in modern spectral plots it is represented by a smooth curve (see Figure 3.5). A hot, low-density gas produces discrete emission lines, whereas when a continuous spectrum passes through cooler material, dark absorption lines are imprinted, appearing as "v-shaped" dips in the continuum plot (see Figures 3.6 and 3.7). In real observations, the continuum shape is further influenced by instrumental response and telluric absorption, meaning it must be empirically estimated. Continuum normalisation is therefore an essential step in spectral analysis, where even small variations in the continuum can significantly impact the detection of atmospheric features. In this work, we employed the Spectra Normalization Tool (SNT), a Python-based code developed at the Instituto de Astrofísica e Ciências do

Espaço *, which implements an alpha-shape algorithm to trace the upper envelope of the spectrum. This method is heavily based on the approach used in RASSINE (Cretignier et al., 2020) and adapted to facilitate modularity and parameter control. The alpha-shape algorithm is used to select a set of points in the spectrum, called anchor points, that are thought to reflect the continuum of the spectra (as opposed to points that reflect absorption lines) and processes them to remove outliers. These anchors are then interpolated (typically using a cubic spline or linear fit) to generate a smooth continuum function. Several parameters control the behaviour of the algorithm, such as the alpha-shape radius, the stretching factor between wavelength and flux axes, and optional smoothing or denoising functions. The output of SNT is a continuum-normalised flux spectrum, where the continuum has been divided out while preserving the relative line depths and shapes. Regarding the uncertainties of the spectra, the same principle from before was applied during the continuum normalisation. As the observed flux was divided by the fitted continuum, the associated uncertainties were divided by the same continuum function to ensure consistent error propagation. The fitted continuum and the resulting continuum-normalised spectrum are shown in Figure 3.8.

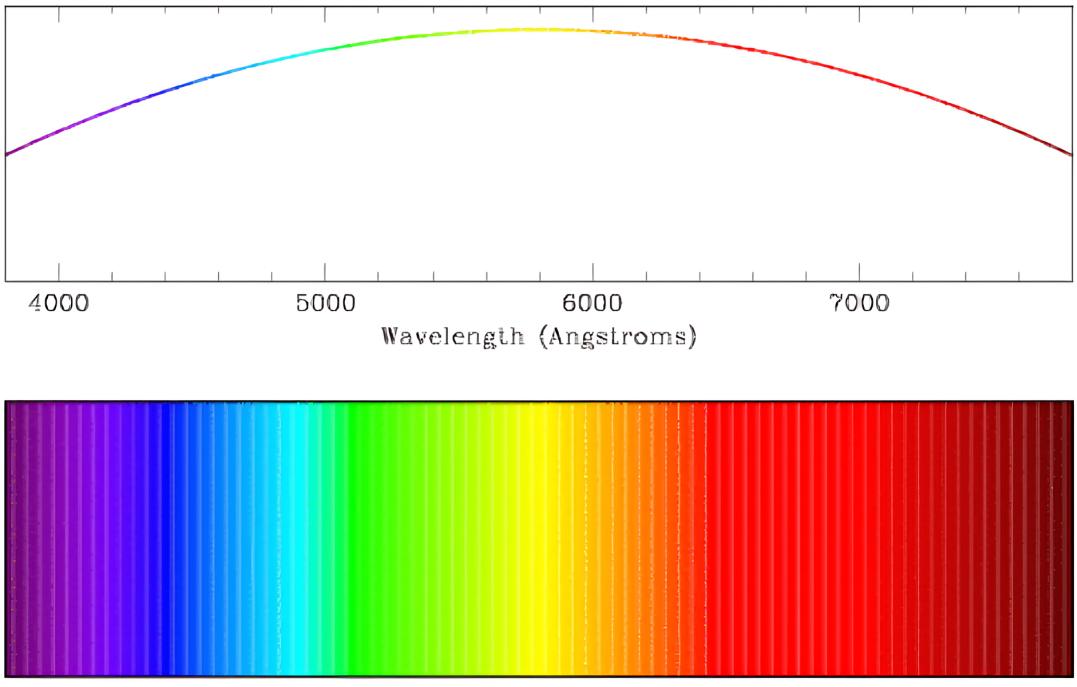

FIGURE 3.5: Continuous spectrum from a hot, dense source. Bottom panel: the photographic spectrum (a rainbow-coloured strip). Top panel: the same spectrum as an intensity vs. wavelength plot. Source: N. Vogt, NMSU lecture notes.

*https://github.com/iastro-pt/Spectra-Normalization-Tool/tree/main

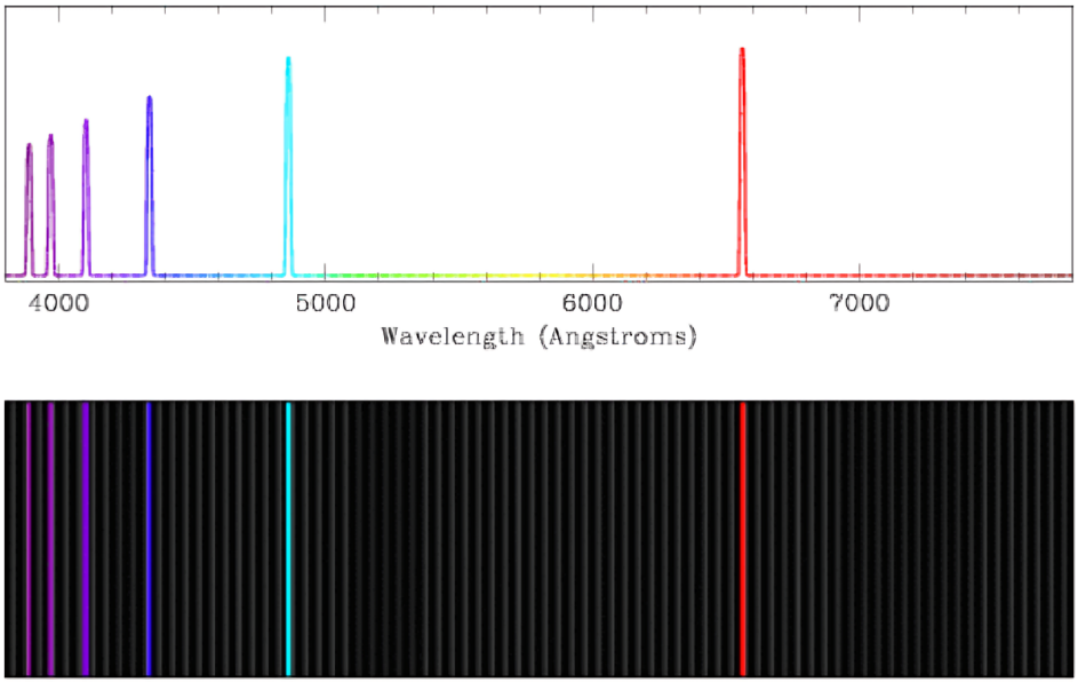

FIGURE 3.6: Emission line spectrum. Top panel: photographic spectrum with bright coloured lines. Bottom panel: corresponding intensity vs. wavelength plot showing sharp emission peaks. Source: N. Vogt, NMSU lecture notes.

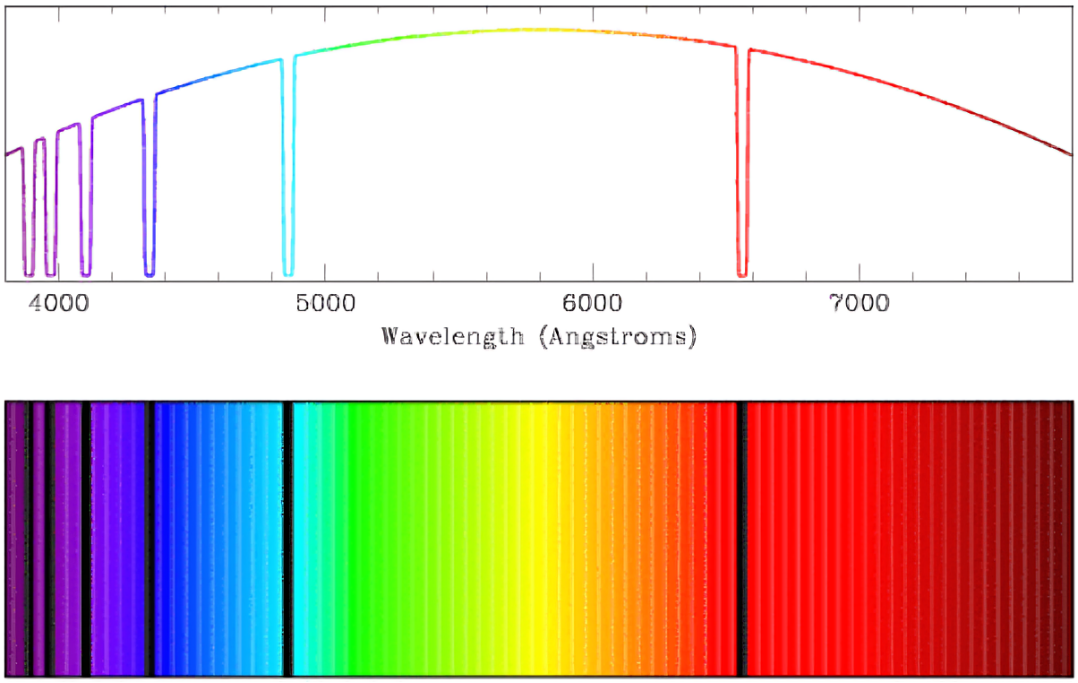

FIGURE 3.7: Absorption line spectrum. Top panel: photographic spectrum showing dark absorption lines across the rainbow background. Bottom panel: corresponding intensity vs. wavelength plot with 'v'-shaped absorption dips. Source: N. Vogt, NMSU lecture notes.

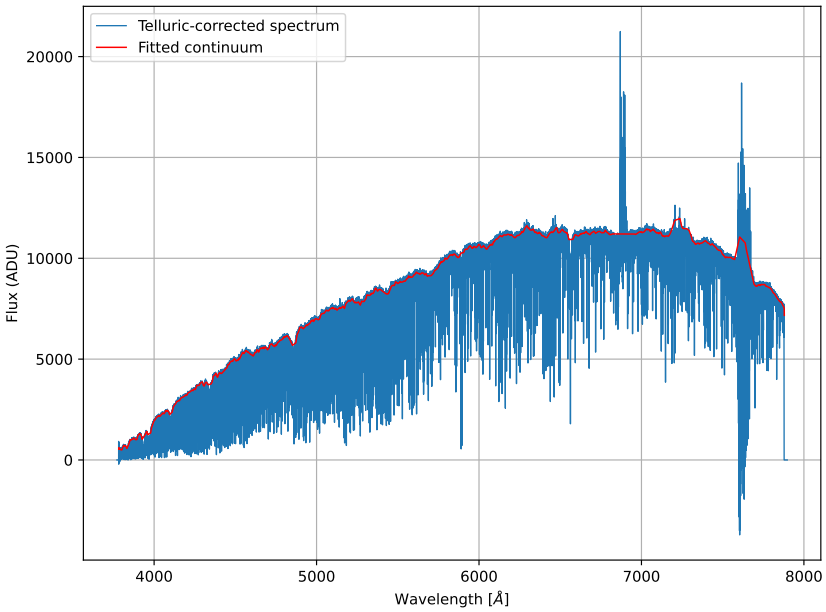

(A) Telluric-corrected spectrum (black) with fitted continuum (red).

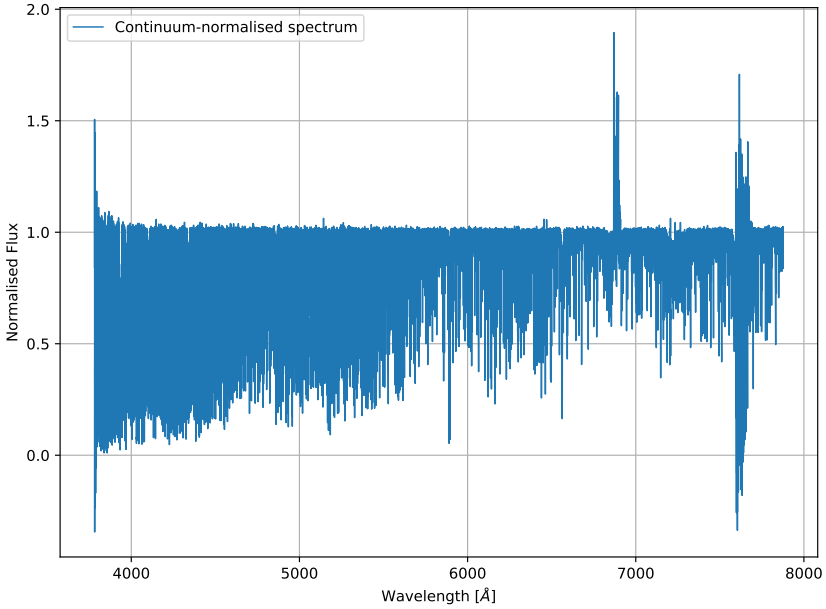

(B) Continuum-normalised spectrum.

FIGURE 3.8: Continuum normalisation process of the first observation of Epoch I, as an example. The top panel shows the measured spectrum in blue, and the continuum fit in red, while the bottom panel presents the normalised spectrum.

3.3. Outlier Identification

Before moving on to the rest of the data pre-processing, we aimed to ensure the data would not be affected by an imperfect correction on the deepest telluric absorptions. For this reason, we decided to mask out the zones where the transmission spectrum from `molecfit` had strong, saturated or nearly saturated, tellurics. Additionally, since the borders of ESPRESSO data are lower in S/N because of the efficiency of the spectrograph

that decreases significantly below 4000 Å (see ESPRESSO user manuals, in particular Fig. 11 of Period 102 *), we excluded all measurements below this threshold to prevent regions with excessive noise from affecting our results. The regions that were masked out are shown in Figure 3.9 and are comprised in these wavelength intervals: [3770-4000] Å, [5867.56–6005.55] Å, [6270.23–6344.15] Å, [6439.08–6606.96] Å, [6858.15–7417.40] Å and [7586.03–7751.12] Å.

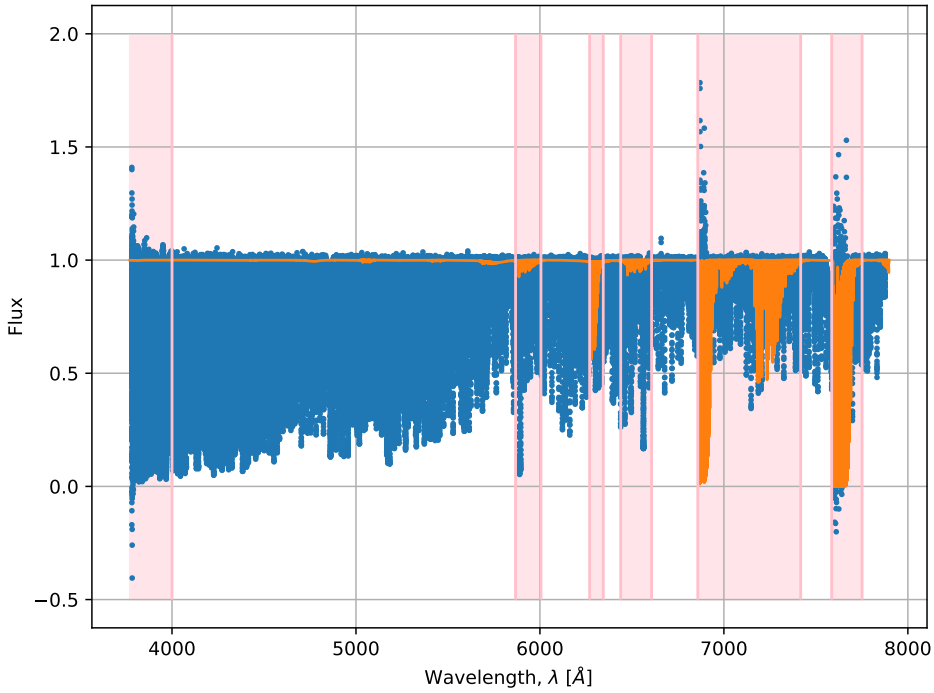

FIGURE 3.9: Masked spectral regions, delimited by the shaded pink area, plotted over a spectrum, in blue, and the telluric transmission of H_2O and O_2, in orange.

Following the masking procedure, we divide each spectrum by their respective median flux. This mitigates residual offsets from imperfect continuum fitting, ensuring robust scaling and that all spectra are aligned at a common baseline (continuum ≈ 1) before subsequent analysis.

At this point, the data still contains unreliable points that can wrongly affect the results. Such outliers can be caused by cosmic rays or instrument effects and need to be dealt with. First, they have to be identified, for which there are several methods. We compared three different approaches which we will get into in Sections 3.3.1 to 3.3.3.

*https://www.eso.org/sci/facilities/paranal/instruments/espresso/doc.html

3.3.1 Full-spectrum smoothing + Mean Absolute Deviation (MAD) clipping

A possible approach to outlier detecting is assessing the deviation of the real data points to those of a smooth flux curve. To this end, we performed a 1D convolution using a Box filter kernel with a width of 5 pixels, so, essentially, each point in the original spectrum is replaced by the average of itself and 2 pixels on each side. The residuals were obtained by subtracting the smoothed spectrum from the observed spectrum. We then computed the mean absolute deviation (MAD) of each spectrum using Equation (3.1). In this approach, data points were flagged as outliers if their residuals exceeded the MAD by 5 times $\left(\text{outliers} \Leftrightarrow |\text{residuals}| \geq 5\,\text{MAD}\right)$. In Figure 3.10 we can observe the identified outliers on one of the spectra of Epoch I after normalisation and masking.

$$\text{MAD} = \frac{1}{N}\sum_{i=1}^{N}|x_i - \bar{x}| \tag{3.1}$$

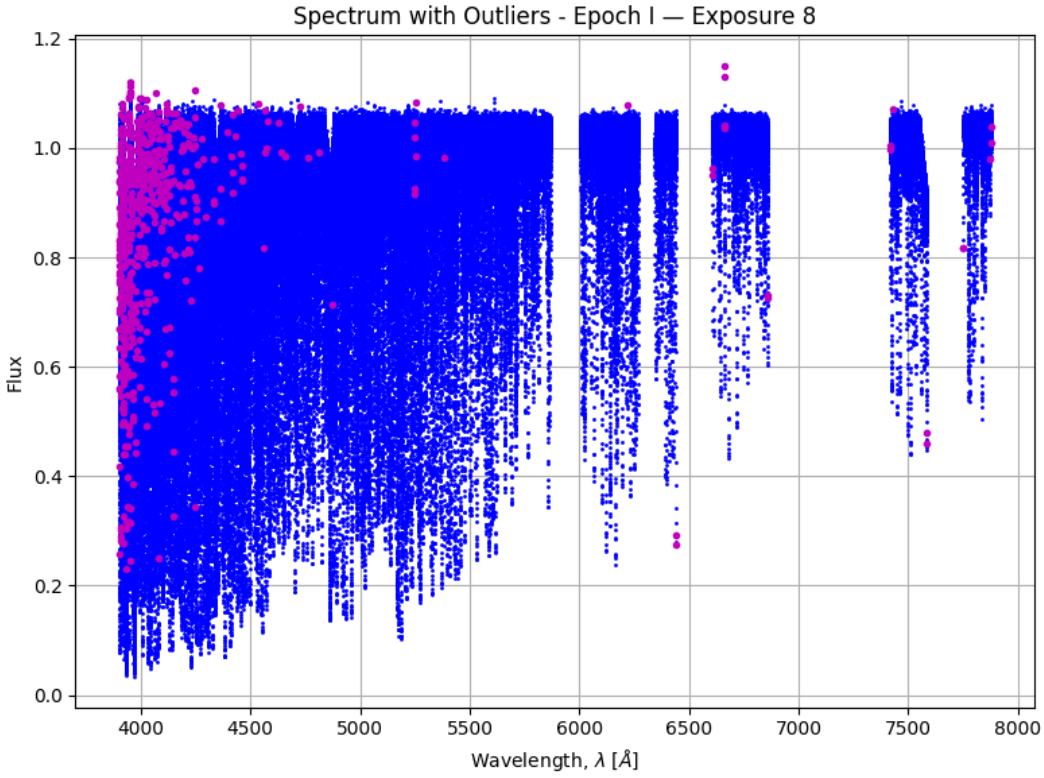

FIGURE 3.10: Outliers identified with the full spectrum smoothing and MAD clipping method, shown as purple points.

3.3.2 Spectrum smoothing + Mean Absolute Deviation (MAD) clipping - using the continuum only

In addition to the full-spectrum MAD clipping, we also tested an alternative approach where the MAD statistics was computed only in regions of the spectrum with flux above 0.95 (i.e. close to the continuum level). This is a way to obtain a more reliable estimate of the scatter in the data and reduce the risk of wrongly flagging deep stellar features as outliers. The process of this approach is the same as before, with the additional step of masking out all spectral regions with flux values below 0.95 for the MAD calculation. As before we identify outliers based on the MAD threshold $\left(\text{outliers} \Leftrightarrow |\text{residuals}| \geq 5\,\text{MAD}\right)$. In Figure 3.11 we can observe the identified outliers on one of the spectra of Epoch I after normalisation and masking.

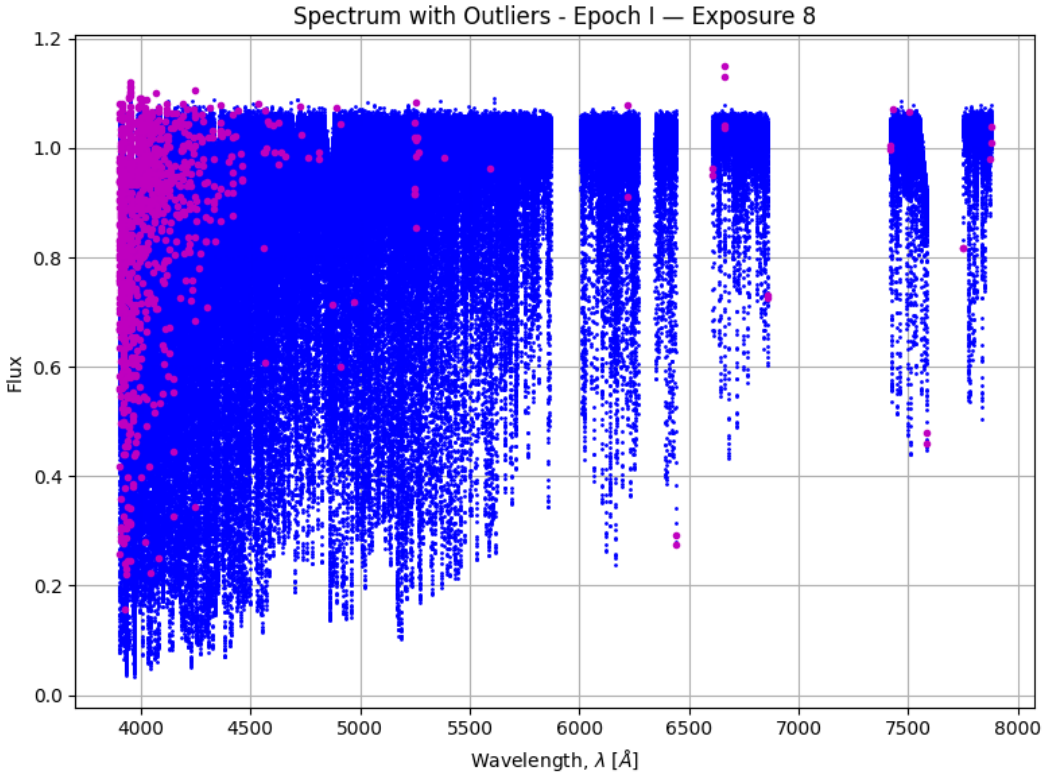

FIGURE 3.11: Same as Figure 3.10 for the smoothing and MAD clipping (using only the continuum) method.

3.3.3 Time-wise flux outlier detection

The previous two methods focus on outlier detection in each spectrum of each Epoch individually. In the third and preferred approach, for each epoch, we considered all observations at a given wavelength pixel. We do this by stacking all the flux measurements

at each wavelength index over all spectra of one epoch, forming a column for every wavelength in the array. For each column, we take its median and its MAD. We rescale the MAD by 1.4826 to obtain a robust estimate of the standard deviation, σ. We then mark as outliers any points deviating more than 3 σ from the median. In Figure 3.12 we can observe the identified outliers on one of the spectra of Epoch I after normalisation and masking.

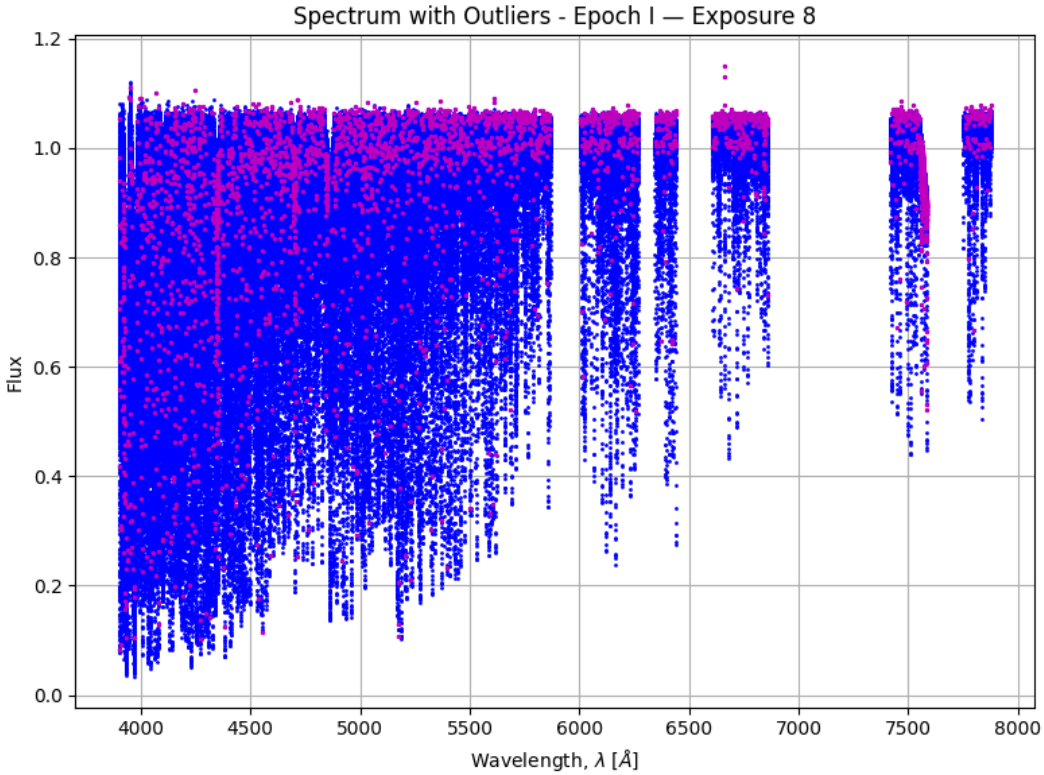

FIGURE 3.12: Same as Figure 3.10 for the time-wise flux outlier detection method.

This method, although presented last, was the one we initially used for our analysis, as it is the one adopted by Costa Silva, A.R. et al. (2024). We started investigating these other outlier detection methods at a later stage and compared them in Figure 3.13 by illustrating the relation between the number of flagged outliers and the S/N of the spectra for all four epochs and the three different approaches considered. This comparison revealed that this method actually performs worse than expected. Specifically, the number of flagged outliers increases at lower S/N, when the opposite should happen, since higher photo-noise should hide outliers at lower S/N. This means the method is likely flagging white noise as outliers. As we had already proceeded with the work using this method before doing this analysis, we can say our choice of outlier detection method is not the best. However,

we believe that because this strategy uses the statistical distribution of flux values across all spectra of an epoch at each wavelength, it makes it less sensitive to individual spectral features. When applying this time-series method, instead of discarding the flagged points, we imputed the local column's median value, ensuring that we do not leave many gaps in the data.

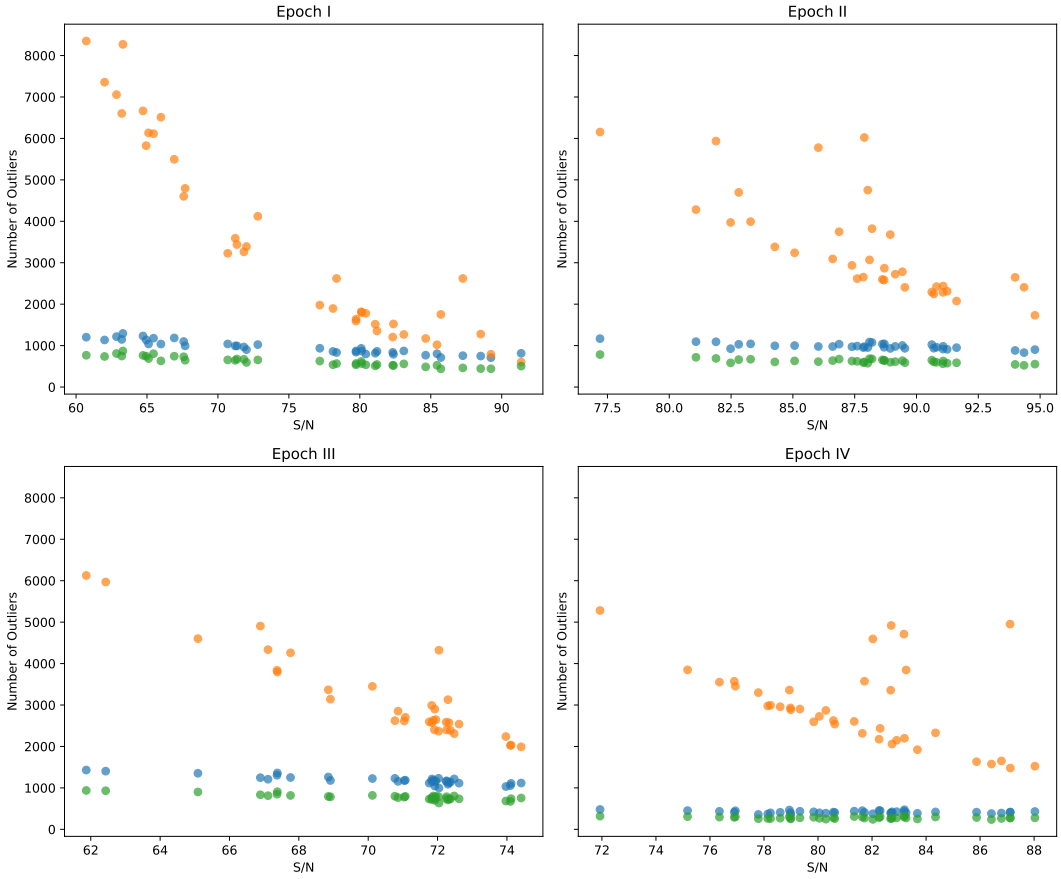

FIGURE 3.13: Number of outliers detected in the exposures of each epoch, separated into panels. The three outlier detection methods are shown, namely the full spectrum smoothing shown as the blue points, the continuum only smoothing shown in green and the time-wise flux in orange.

3.4. Stellar Rest Frame Alignment

The next step in our data pre-processing is ensuring we are working in the correct reference frame. As we will now aim at correcting the stellar imprints on the spectra, we need to make sure that the wavelength vector that we are working with is the wavelength vector as emitted by the source (in this case, the star), λ_e, i.e. expressed in the Stellar Reference Frame (SRF) where the source is immobile. The ESPRESSO DRS corrects the data for the Earth's movement around the Barycenter of the Solar System through the Barycentric Earth RV (BERV) and the S1D spectra that it provides are expressed in the reference frame of the Solar System's Barycenter (SSB). In this referential, the observed wavelength

vector, λ_{obs}, is Doppler shifted compared to λ_e following Equation (3.2), where RV is the radial velocity of the target, this is, the velocity of the target in the line of sight with the observer and c is the speed of light ($c \approx 2.99 \times 10^5$ km/s). When the RVs are very low, which is the case of this work, with RVs ranging from $-1.3\,\mathrm{km\,s^{-1}}$ to $-1.1\,\mathrm{km\,s^{-1}}$, we can use the fact that $\frac{RV}{c} << 1$ to approximate $\frac{1}{1+\frac{RV}{c}} \approx 1 - \frac{RV}{c}$, therefore Equation (3.2) becomes Equation (3.3).

$$\lambda_{obs} = \lambda_e \sqrt{\frac{1+\frac{RV}{c}}{1-\frac{RV}{c}}} \Leftrightarrow \lambda_e = \lambda_{obs} \sqrt{\frac{1-\frac{RV}{c}}{1+\frac{RV}{c}}} \tag{3.2}$$

$$\lambda_e = \lambda_{obs} \left(1 - \frac{RV}{c}\right) \tag{3.3}$$

To align the stellar spectra, we must thus shift them from the SSB to the SRF. A schematic of these reference frame shifts is shown in Figure 3.14. The correction to pass from the target system's barycentre to the SRF (**III**) or later to the Planetary Reference Frame (PRF) (**IV**) is done using the RV model for an orbiting body, as defined in Equation (3.4), where θ is the true anomaly, t is the time of the observation, ω is the argument of the periastron and K is the body's RV semi-amplitude. The correction to pass from the SSB to the target system's barycentre (**II**) is done using the systemic velocity, v_{sys}, this is, the velocity of the target system relative to the observer.

$$RV = K \left[\cos\left(\theta(t) + \omega\right) + e \cdot \cos\omega\right] \tag{3.4}$$

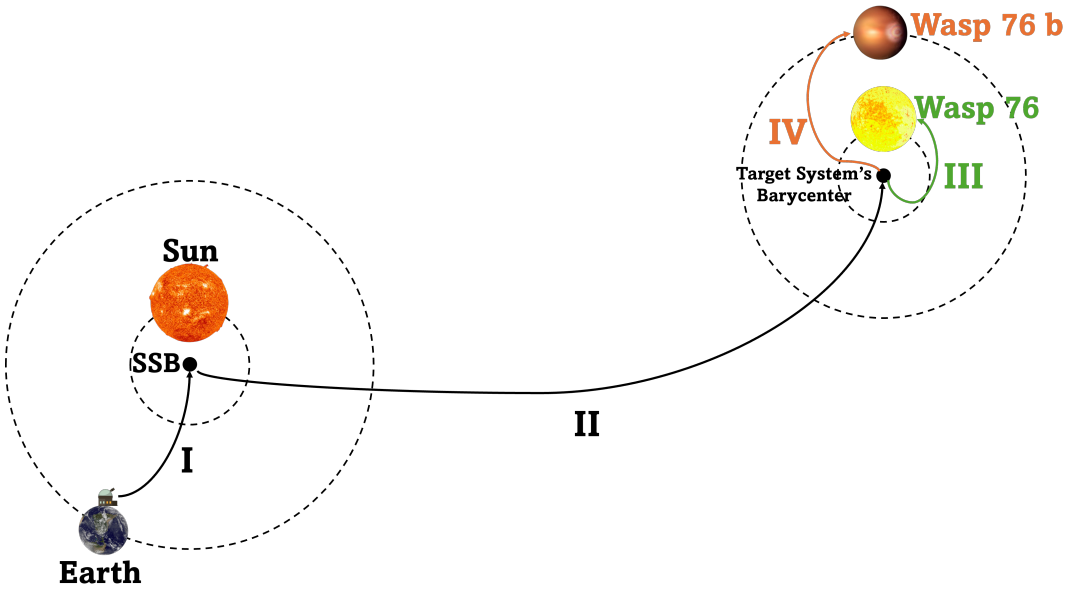

FIGURE 3.14: Adapted from Figure 1.11 from Seidel (2021). Schematic of reference frame shifts. **I**: BERV correction of the Earth's movement around the SSB. **II**: Shift from the SSB to the target system's barycentre (SSB): v_{sys}. **III**: Shift from the target system's barycentre to the SRF: Equation (3.4) **IV**: Shift from the target system's barycentre to the PRF: Equation (3.4).

As pointed out by Costa Silva, A.R. et al. (2024), there are discrepancies in the systemic velocity (v_{sys}) values reported in the literature for WASP-76. The discovery paper gives $v_{sys} = -1.0733 \pm 0.0002\,\mathrm{km\,s^{-1}}$ (West et al., 2016), SIMBAD reports $-1.152 \pm 0.0033\,\mathrm{km\,s^{-1}}$ from Gaia Data Release 2 (DR2) (Soubiran et al., 2018), while Ehrenreich et al. (2020) obtained slightly different values for each of their observing epochs: $-1162.00^{+2.86}_{-2.63}\ \mathrm{m\,s^{-1}}$, $-1167.54^{+2.79}_{-2.73}\ \mathrm{m\,s^{-1}}$ and $-1171.11^{+1.28}_{-1.36}\ \mathrm{m\,s^{-1}}$. This parameter is important for an accurate alignment of spectra across rest frames, and Costa Silva, A.R. et al. (2024) therefore re-determined it by performing a simple least-squares fit of a Keplerian model to the RV values provided by the ESPRESSO pipeline, leaving v_{sys} as the only free parameter.

Following their approach, we repeated this procedure for our work in order to ensure a consistent reference frame for each epoch. The least-squares fit was applied to Equation (3.5), where RV_{obs} refers to the BERV corrected RVs observed by ESPRESSO. A circular orbit ($e = 0$) was assumed (Costa Silva, A.R. et al., 2024, Ehrenreich et al., 2020, Valente and Correia, 2022), and the argument of periastron was set to $\frac{\pi}{2}$. The other orbital elements were set to those listed in Tables 2.1 and 2.2. In a circular orbit, the true anomaly, $\theta(t)$, is the same as the eccentric anomaly, E, and the mean anomaly, M. Therefore, following Equation (3.6), for the assumed circular orbit, the true anomaly, $\theta(t)$ corresponds to the phase of our observations, where P is the orbital period and $\tau = T_c$ (mid-transit

time). The uncertainties of the values of v_{sys} we computed were obtained through the square root of the diagonal elements of the covariance matrix of the algorithm. These values ($0.0002 - 0.0003\,km\,s^{-1}$) represent the internal statistical precision of the fit, although the true uncertainty is expected to be larger due to correlations with the other parameters.

The values we computed for v_{sys} were:

- Epoch I: $v_{sys} = -1.2106\,km\,s^{-1} \pm 0.0003\,km\,s^{-1}$
- Epoch II: $v_{sys} = -1.2129\,km\,s^{-1} \pm 0.0003\,km\,s^{-1}$
- Epoch III: $v_{sys} = -1.2073\,km\,s^{-1} \pm 0.0002\,km\,s^{-1}$
- Epoch IV: $v_{sys} = -1.2108\,km\,s^{-1} \pm 0.0003\,km\,s^{-1}$

$$RV_{obs} = v_{sys} + K_\star \left[\cos\left(\theta(t) + \omega\right) + e \cdot \cos\omega\right] \tag{3.5}$$

$$M = \frac{2\pi}{P}(t - \tau) \tag{3.6}$$

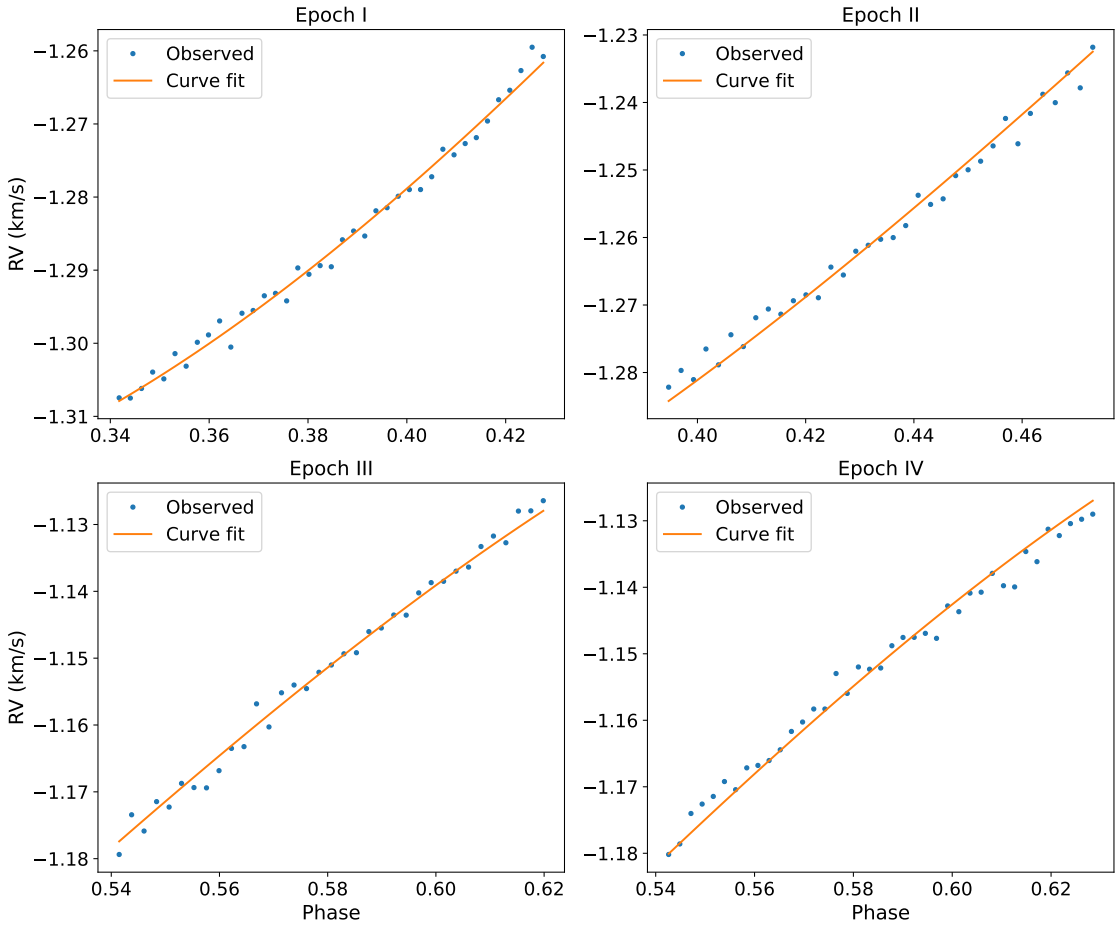

FIGURE 3.15: Observed stellar RV values divided into epochs, with the corresponding fits represented by the orange lines.

After computing the best-fit values of v_{sys}, we used them to model the stellar RVs for each observation phase with Equation (3.5). The fitted RV curves are shown in Figure 3.15. These modelled RVs were then used to compute the Doppler shift to finally pass all spectra to the SRF following Equation (3.3).

3.5. Stellar Template and Planet Spectrum Extraction

Given that the primary goal of this work is to identify emission from the planet's atmosphere, it is essential to remove the stellar contribution from the observed spectra. To achieve this, we must first identify the stellar component in our data by building a stellar template for each epoch. This template is obtained as the median of all spectra in that epoch. Before performing the median, we need to ensure that the spectra are all expressed in a common wavelength grid. This is guaranteed by interpolating each exposure in that epoch onto a common grid, which we do using cubic splines. The common wavelength grid is arbitrarily chosen to be the wavelength array of the first exposure for each epoch.

With all spectra aligned in the SRF on a common grid, the stellar lines appear at the same wavelength in every exposure, ensuring that their signal is magnified in the stellar template. As we will discuss ahead in Chapter 4, the planet's RV changes by at least ≈ 1.5 km s^{-1} between consecutive exposures. This ensures that the planetary signal besides being faint, shifts in wavelength over time in the SRF and is thus further attenuated by the median. The use of the median rather than the mean also guarantees that the template is robust against residual outliers, enhancing the stellar lines while suppressing unwanted features. Figure 3.16 shows the stellar template obtained for each epoch.

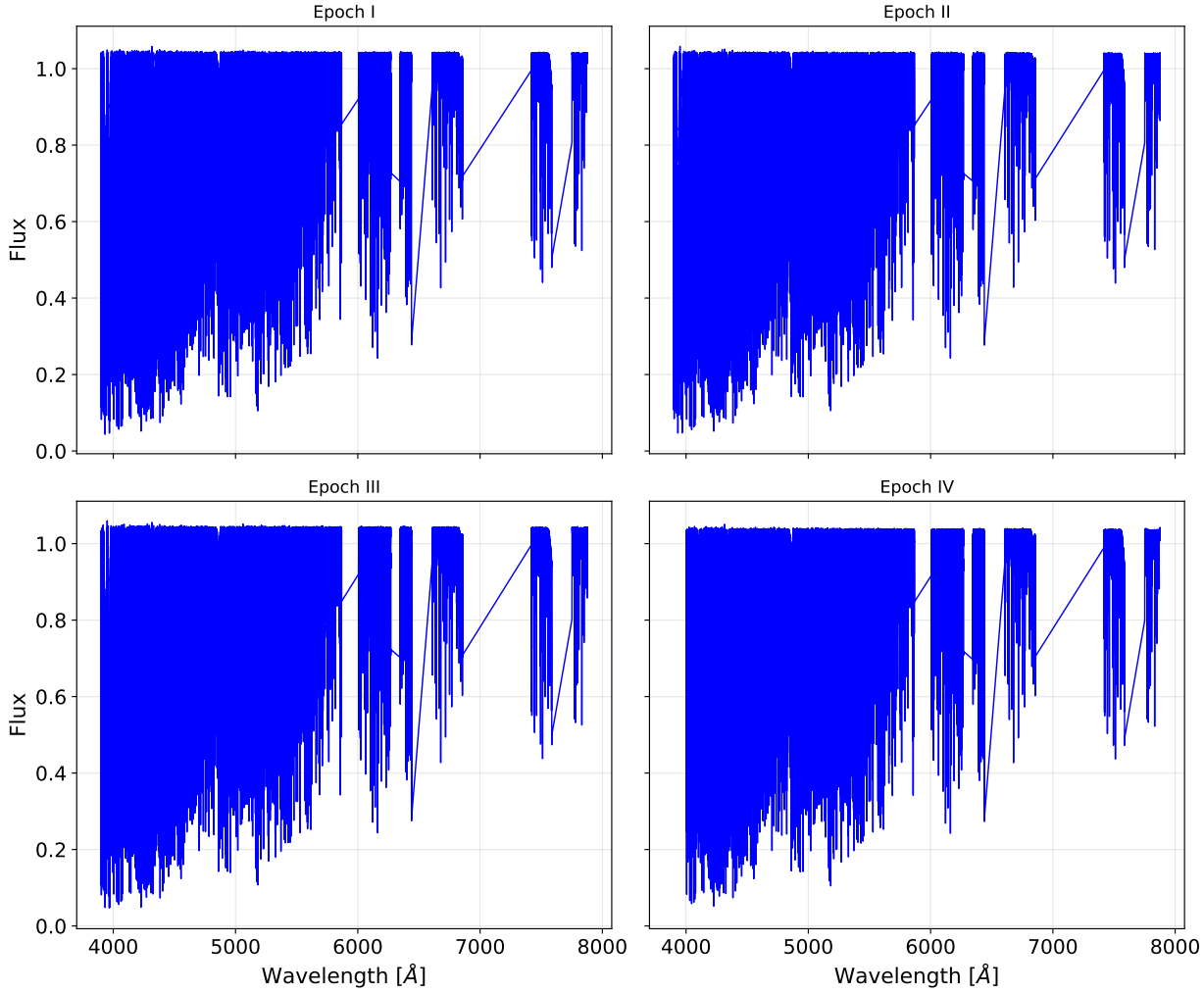

FIGURE 3.16: Stellar template for each Epoch (median-stacked spectra in SRF).

After singling out the stellar component of our data, we use it to single out just our planet's contribution, by subtracting the median star template to the data. Once this subtraction is applied, we are left with the emission of our planet in the SRF. Figure 3.17 shows an example of the planet's spectrum for one of the observations of Epoch I.

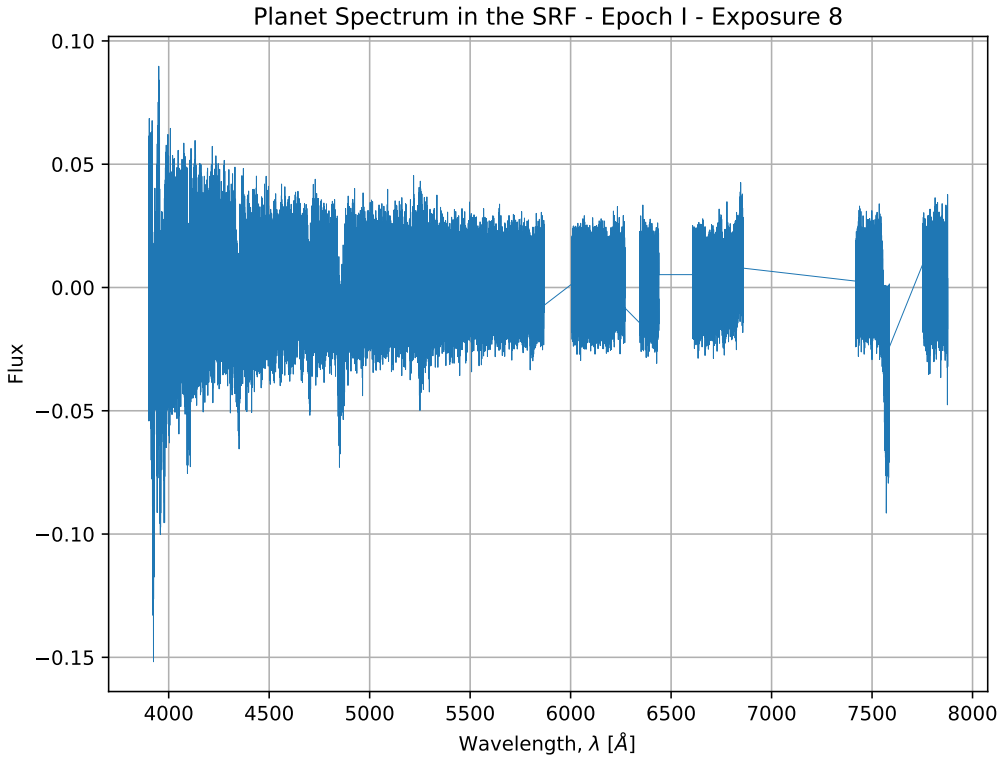

FIGURE 3.17: Planetary spectrum from epoch I shown in the SRF, after subtracting the stellar template.

Upon closer inspection of the spectra in the SRF, particularly when over-plotting multiple exposures, we identified regions showing misalignment and inconsistent flux levels between exposures. These discrepancies are most evident around the cores of strong stellar lines and in zones affected by telluric absorption, though they could also result from imperfect continuum normalisation. In future work, it would be valuable to refine the normalisation step and assess its impact on the results. To evaluate whether the observed inconsistencies could bias our analysis, we adopted a dual strategy for Epoch I: in one case, applying additional masks to the problematic regions, and in the other, treating the data consistently with the other epochs, this is, without the additional masks. If the masked approach had resulted in significantly improved results, we would have extended it to all epochs; however, this was not the case. The additional masked intervals are shown in Figure 3.18 and correspond to [3958.837, 3960.862] Å, [3970.411, 3979.377] Å,, [4840.530, 4874.564] Å, and [7555.999, 7586.1] Å.

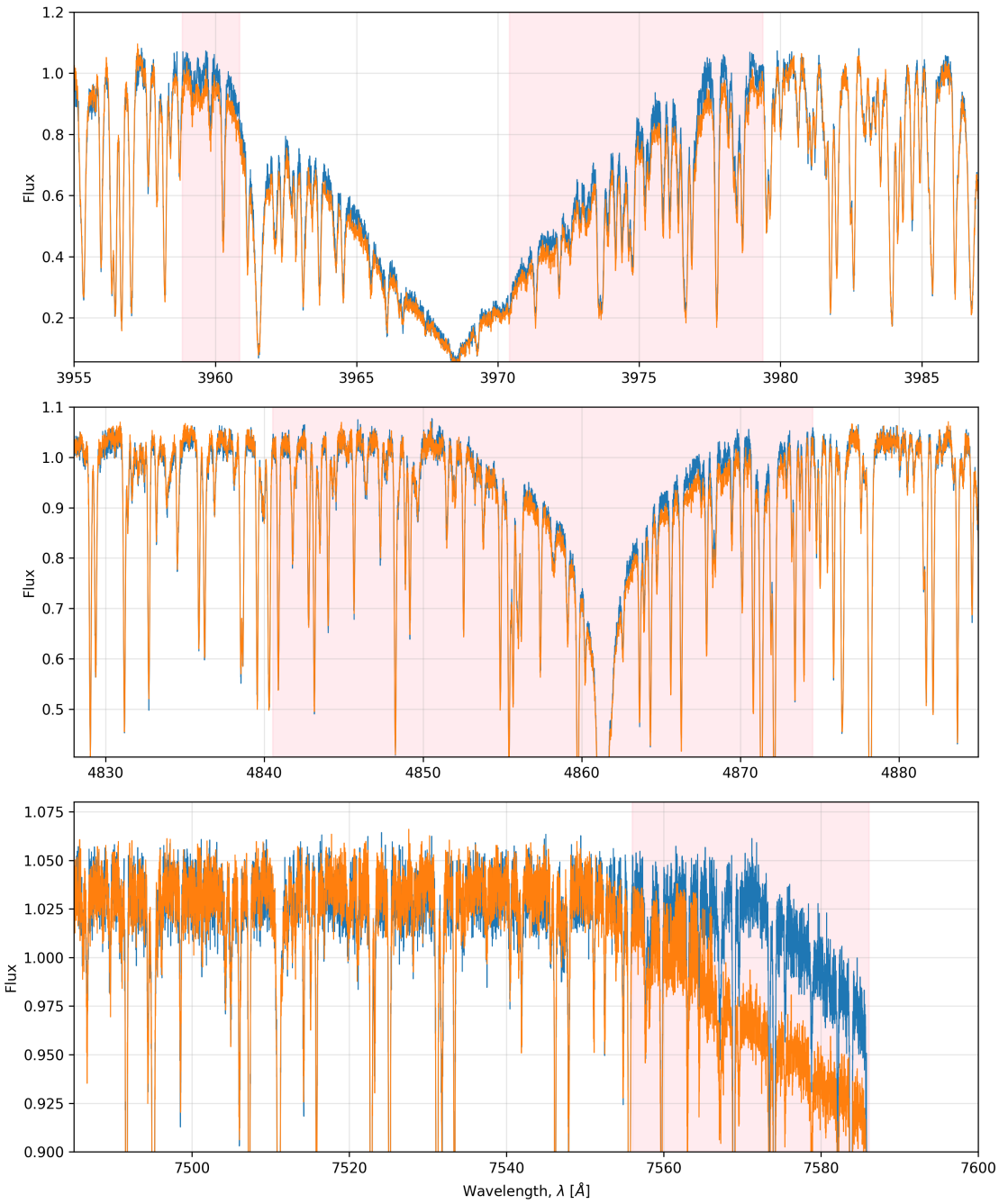

FIGURE 3.18: Comparison in different wavelength ranges of the first and last exposures of normalised stellar spectra of Epoch I with the extra masks to be applied shaded in red.

Chapter 4

Analysing the Planet Spectra

Having obtained the planetary spectrum, we aim to verify the presence of neutral iron by comparing it with a theoretical template spectrum of our planet's atmosphere containing Fe I using the CCF method.

4.1. Synthetic Model with petitRADTRANS

In order to obtain a synthetic model simulating our planet's atmosphere with iron as the only trace species, we used the Python package petitRADTRANS (version 3.1.3) (Mollière et al., 2019). petitRADTRANS is a quick and reliable Python radiative transfer code built for the spectral characterization of exoplanet atmospheres and can be used to obtain transmission and emission spectra of exoplanets, at low ($\lambda/\Delta\lambda = 1000$, correlated-k method) or high ($\lambda/\Delta\lambda = 10^6$) resolution. Given user-defined P-T profiles and chemical abundances, the code computes the synthetic spectrum by solving the radiative transfer, taking into account the effects of molecular and atomic line opacities, clouds, Collision Induced Absorption (CIA) and Rayleigh scattering.

To produce our synthetic spectrum, we modelled an emission spectrum of WASP-76b using petitRADTRANS, assuming a H_2-He dominated atmosphere with the trace species Fe I. The atmosphere is represented by 150 logarithmically spaced pressure layers from 2 μbar to 200 bar. Opacity sources include continuous absorption due to collisions between H_2-H_2 (Borysow et al., 2001, Borysow, 2002) and H_2-He (Borysow et al., 1988, 1989, Borysow and Frommhold, 1989) molecules (collision-induced absorption), and Fe I opacities treated line-by-line (high resolution mode) over the wavelengths of 0.35–0.8 μm. The CIA and Fe I opacities were obtained via Keeper*, with the spectral lines of Fe I being

*https://keeper.mpdl.mpg.de/d/ccf25082fda448c8a0d0

determined from the line lists of Kurucz* and contributed by K. Molaverdikhani†. The atmospheric composition is fixed in every layer, with H_2 and He making up 0.74 and 0.24 of the mass, respectively, Fe at 0.0017, corresponding to the solar abundances according to Lodders (2020), and a mean molar mass of 2.33 atomic mass units (amu). The other necessary parameters (e.g. reference gravity) were set to those of WASP-76 b. Lastly, the only thing left to define is the pressure-temperature (P-T) profile. The profile we use was based on the Global Circulation Models (GCM) of Wardenier et al. (2021, 2023, 2025) and on the one adapted by Costa Silva, A.R. et al. (2024). We defined two isothermal layers, with the deep atmosphere at T = 1700 K and P > 0.1 bar and the upper atmosphere at T = 3500 K and P < 0.001 bar, and implemented a linear slope between them, with temperature decreasing with pressure, thus increasing with height, corresponding to a thermally inverted atmosphere. We also attempted to generate this P–T profile using the petitRADTRANS function `temperature_profile_function_guillot_global`, following Guillot (2010), for comparison. Although we did not continue with the Guillot function model, Figure 4.1 shows a Guillot profile, for comparison, and the inversion profile ultimately used in this work.

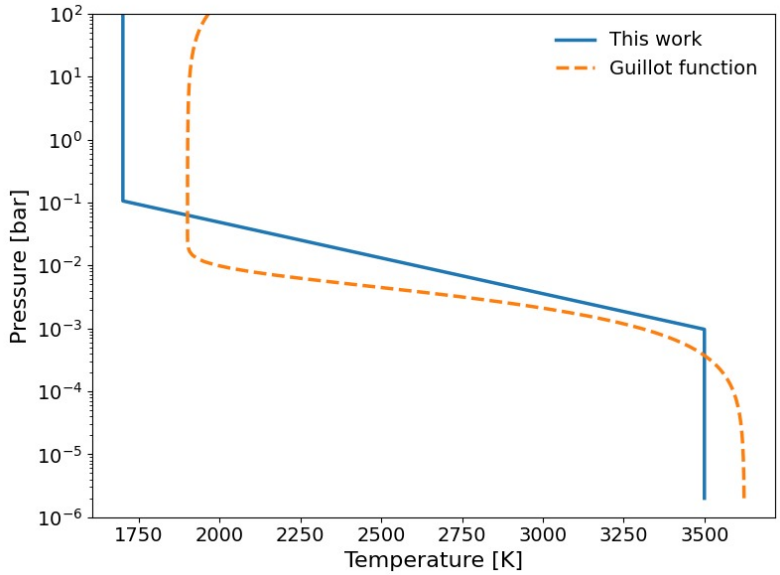

FIGURE 4.1: Comparison between the adopted P-T profile (blue) and a similar Guillot profile (orange).

Using the parameters and P-T profile described above, we were able to produce the synthetic model shown in Figure 4.2, with the units of wavelength and flux provided by petitRADTRANS in its standard setting, so flux, F_λ, in erg cm^{-2} s^{-1} cm^{-1}. This corresponds to

*`http://kurucz.harvard.edu/`
†karan.molaverdikhani@colorado.edu

the simulated intrinsic emission spectrum of the planet's atmosphere, independent of the stellar contribution. In some studies, however, these spectra are further transformed into contrast models $\left(F_{\text{planet}}/F_{\text{star}}\right)$ by scaling with the projected area of the planetary disk and normalising by the stellar flux modelled as a blackbody of temperature the same as the effective stellar temperature. To further resemble our synthetic spectrum to one observed by ESPRESSO, we convolved it with a Gaussian kernel to match the resolution of our observations ($R \approx 140000$). An additional important step for preparing the synthetic model for the CCF method is continuum correction. To achieve this, we identified continuum regions in the spectrum, applied a fourth-degree polynomial fit, and subtracted this fit from the spectrum, ensuring that the continuum of our template is centred at zero. Figure 4.3 shows the continuum-corrected synthetic models produced with petitRADTRANS. We present both the convolved and unconvolved models, as well as versions in the original flux units and transformed into contrast models. Displaying these four versions is useful because, during our CCF analysis, we initially obtained uninterpretable results and tested different versions of the synthetic spectrum. We later identified that the cause of these unexpected results was primarily related to misalignments in the rest frame.

4.2. Cross-Correlation Method

With the planetary spectrum extracted from our observations and a corresponding synthetic model in hand, we can proceed to compute the cross-correlation function (CCF). For a general introduction to the CCF method, we refer to Chapter 1. In this work, we implement the method by comparing each observed spectrum with a synthetic model generated using petitRADTRANS. Throughout this section, we present the results obtained with the synthetic model convolved to match the resolution of our data and expressed in flux units (see Figure 4.3a).

We use a non-weighted CCF as defined in Equation (4.1), where s_i denotes the flux at each data point in the planetary spectrum, and $m_i(RV)$ represents the corresponding model value shifted by a radial velocity RV.

$$\text{CCF}(RV) = \sum_i s_i \, m_i(RV) \tag{4.1}$$

Each exposure therefore produces one CCF curve, computed over a velocity range from

-300 to 300 km s^{-1} in steps of 1 km s^{-1}. To implement this in `Python`, we tested two functions: the `PyAstronomy` cross-correlation routine* and a custom routine from Costa Silva, A.R. et al. (2024). At this stage, the observations, and consequently the CCFs, are still in the SRF. The next step is to shift them into the PRF, which requires transforming back to the system barycentre and applying the planet's radial velocity. We then interpolate all CCFs onto a common velocity grid of $[-120, 120]$ km s^{-1}. The resulting CCFs, aligned in the PRF, are shown in Figure 4.4.

The final step is to sum the CCFs. First, we sum them within each epoch, and then we combine all 148 exposures in the PRF. A detection of the Fe I emission lines implies a peak of the CCF around RV = 0 km s^{-1} (when working in the PRF). To present this peak relative to the noise, we convert the CCFs into a S/N scale. This is done by taking the mean and standard deviation of a baseline region (defined within $[-115, -35]$ km s^{-1} and $[35, 115]$ km s^{-1}), subtracting the mean from the CCF values, and dividing by the standard deviation. To each summed CCF in S/N scale, we fitted a Gaussian curve to the region around 0 km s^{-1}, which allows us to retrieve the RV value of the CCF peak, that, in the absence of atmospheric dynamics, is expected to be null. Figure 4.5 shows the CCFs of each epoch summed in the PRF, and Figure 4.6 shows the sum of all of them, with the respective Gaussian profile identified. We note that, particularly for Epoch I, the peak is not clearly distinguished from the noise, and that a slight slope appears on the negative side of the CCF. After achieving our results using the method described this far, we attempted to improve the S/N by testing alternative normalisation strategies, such as subtracting the median instead of the mean, applying rolling mean/median filters, and using only the positive baseline ($[35, 115]$ km s^{-1}) to estimate the noise. In addition, we repeated the analysis on the alternative spectra for Epoch I described in Section 3.5, where more spectral regions had been masked. A comparison of these approaches, along with the results obtained using the `PyAstronomy` function and the routine from Costa Silva, A.R. et al. (2024), is presented in Figure 4.7.

Instead of fixing the planet's semi-amplitude, K_p, one can explore a grid of K_p values. For each trial value the CCF is re-computed over a range of radial velocity shifts, and the outcomes are combined into a two-dimensional diagnostic diagram, commonly referred to as the K_p-v_{sys} map (Brogi et al., 2012, Boldt-Christmas et al., 2024). This map functions as a detection tool, since the planetary signal manifests as a bright region of high correlation near the true K_p ($K_p = 196.52 \pm 0.94$ km s^{-1} in our case) and at $v_{sys} \approx 0$ km s^{-1}. The signal

*`https://pyastronomy.readthedocs.io/en/latest/pyaslDoc/aslDoc/crosscorr.html`

is expected at zero on the systemic velocity axis because we shift the CCFs into the PRF, however if this correction were not applied, the expected signal would instead be centred on the target's systemic velocity. The K_p-v_{sys} plot of the four epochs combined is shown in Figure 4.8 and for each epoch in Figure 1 from the Appendix. For the purpose of studying the effect of the orbital phase in the detection of Fe I, we also computed the summed CCF for the pre- and post- eclipse ranges, this is, the CCFs of Epochs I and II were added to make Figure 4.9a (pre-eclipse) and the Epochs III and IV were also co-added resulting in Figure 4.9b.

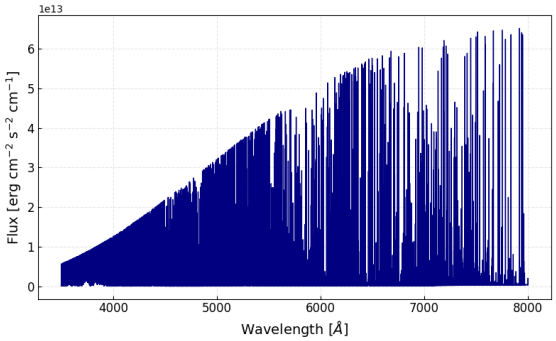

FIGURE 4.2: Synthetic model emission spectrum of Fe I for WASP-76 b, produced with petitRADTRANS.

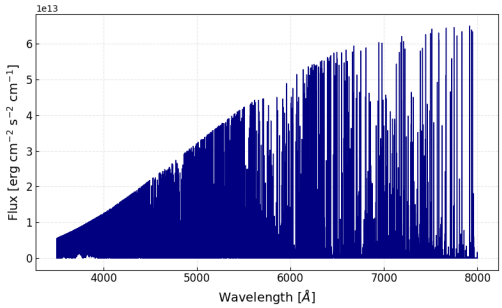

(A) Synthetic model convolved to a resolution of 140000 in flux units.

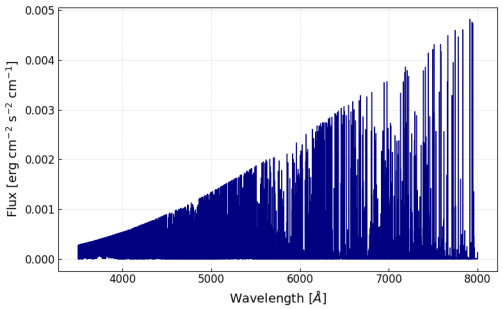

(B) Synthetic model convolved to a resolution of 140000 transformed into a contrast model ($F_{planet}/F_{\star}$).

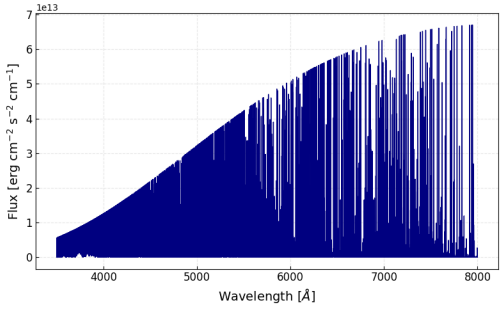

(C) Synthetic model in the original resolution of 10^6 in flux units.

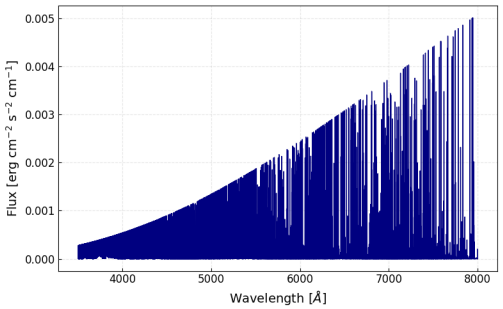

(D) Synthetic model in the original resolution of 10^6 transformed into a contrast model ($F_{planet}/F_{\star}$).

FIGURE 4.3: Different forms of the synthetic emission spectrum of Fe I created with petitRADTRANS. The mainly used one is shown in the top left panel.

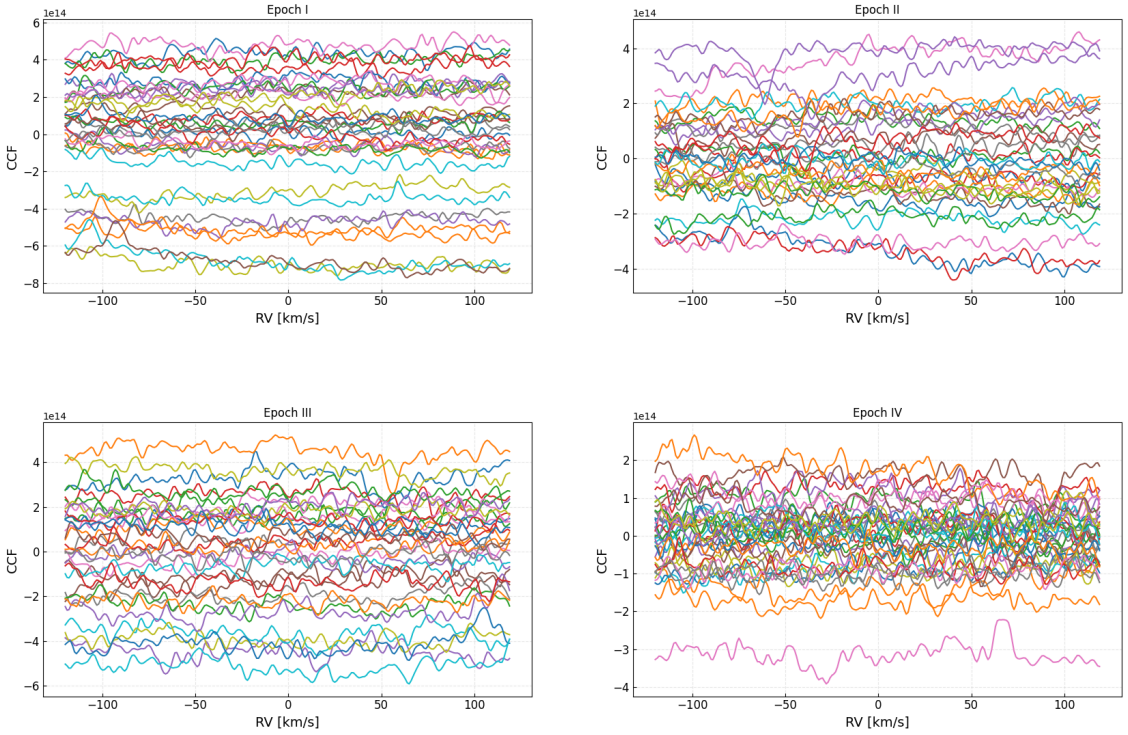

FIGURE 4.4: Resulting CCFs of each exposure split into epochs in the PRF.

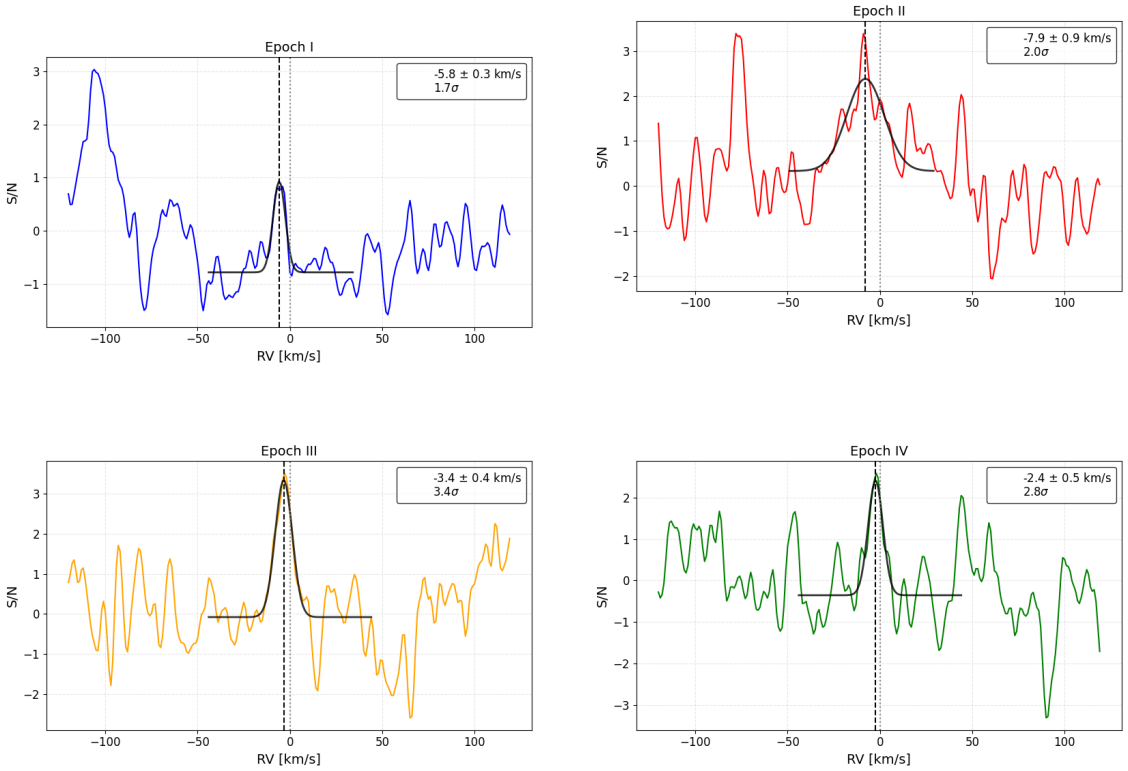

FIGURE 4.5: Summed CCF per epoch, along with Gaussian profiles fitted to the regions near null RV, shown in black. The vertical black dashed lines represent the centres of the fitted profiles.

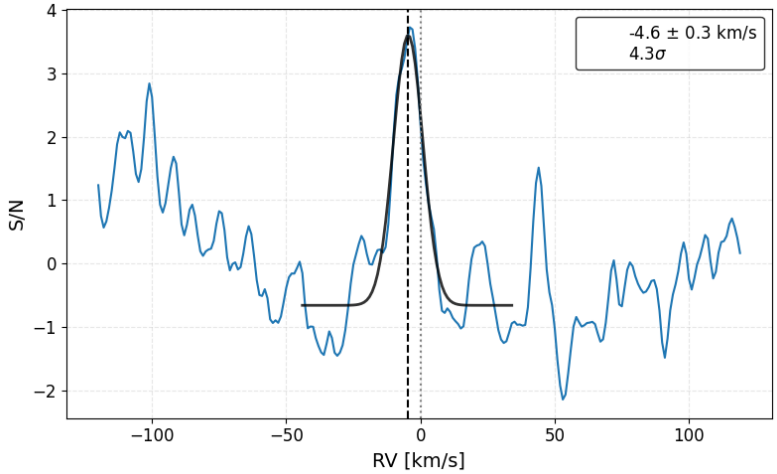

FIGURE 4.6: Global CCF resulting from the sum of all observations, in blue, with its respective Gaussian fit, in black. The vertical black dashed line represents the centre of the fitted profile.

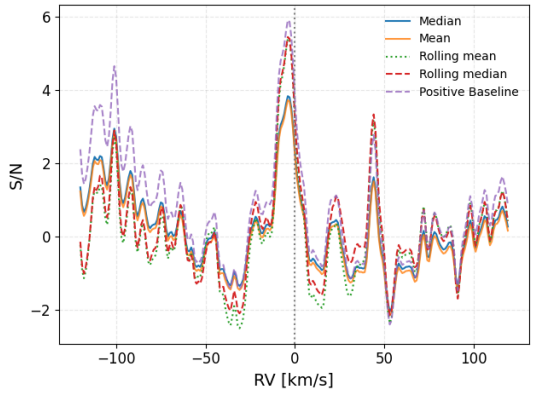

(A) Comparison between different methods of determining the CCF S/N scale.

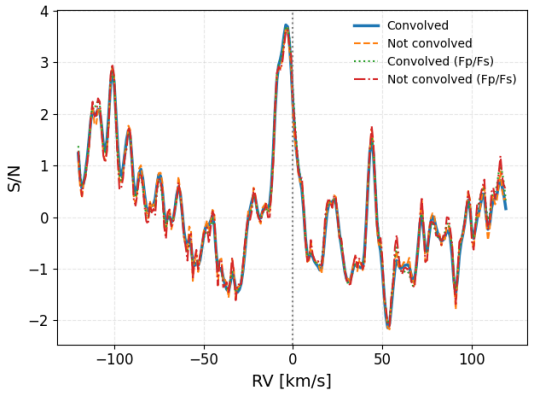

(B) Comparison between the models represented in Figure 4.3.

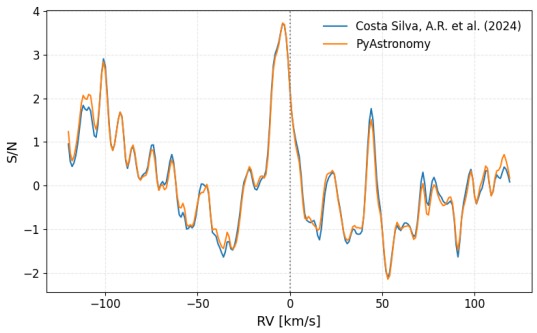

(C) Comparison between using Costa Silva, A.R. et al. (2024)'s routine and PyAstronomy's routine.

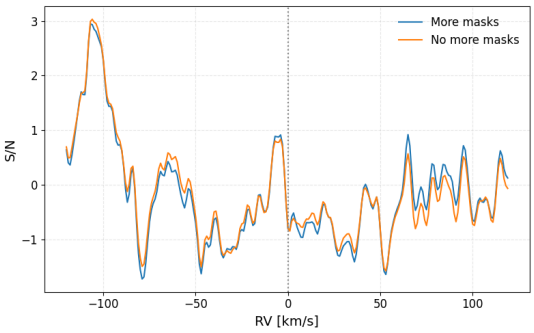

(D) Epoch I: sames masks as the other epochs (in orange) and including the masks from Figure 3.18 (in blue).

FIGURE 4.7: Comparison between the resulting summed CCFs obtained through different methods.

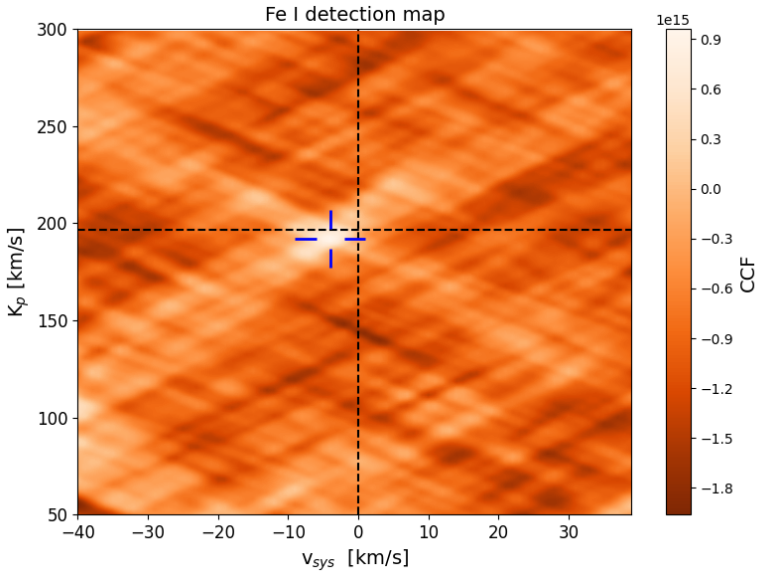

FIGURE 4.8: K_p-v_{sys} plot of the Fe I detection, with the intensity in arbitrary units. The blue crosshair locates the maximum intensity point while the black dashed lines indicate the expected position of the peak, assuming no dynamics or asymmetric structure.

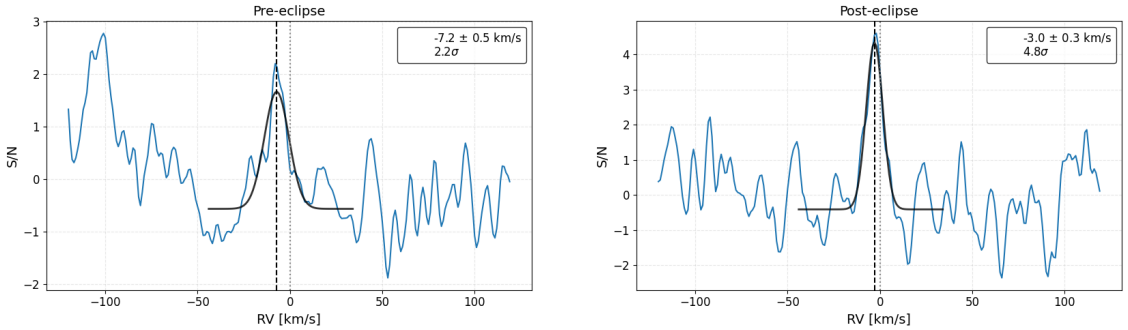

(A) Epochs I and II.

(B) Epoch III and IV.

FIGURE 4.9: Resulting CCFs from summing all pre-eclipse (A) and post-eclipse (B) exposures. Each is shown with its respective Gaussian fit to the peak near null RV, in black.

4.3. Discussion

From the direct observations of the above figures, we can report that Fe I is tentatively detected at a $\approx$ 2-3σ level in each epoch and that all epochs show a blueshifted signal. The significance of these tentative detections is 1.7σ, 2.0σ, 3.4σ and 2.8σ for Epochs I, II, III and IV, respectively, which are fairly low values for S/N. We noticed in the individual CCFs that they are not well centred around 0, which could be due to imperfect normalisation. In Figure 4.7d we compare the CCFs for Epoch I using the case where we masked extra regions, and we conclude that did not affect relevantly the resulting CCFs, however that does not mean that more careful normalisation of the observations would not contribute to more centred CCFs. There were some actions we could have taken to try and correct for this, such as subtracting the median of all CCFs to themselves. We also note that there is a significant slope on most of the CCFs, particularly towards the negative RV values. We tried minimizing their effect with different methods to calculate the S/N. As we can observe from Figure 4.7a when using only a positive baseline for the S/N conversion the significance of the peak increases, however it also accentuates the slope in the CCF. In contrast, when applying the rolling mean and rolling median methods with a window of 75 points, the slope is slightly improved and the peak enhanced. A smaller window size would improve the slope even further, however it would compromise the peak. Although this represented a promising alternative approach that could be further optimised, it was tested only at a later stage, and therefore we ultimately adopted the mean-based method as in Costa Silva, A.R. et al. (2024).

The additional peaks and the residual slope could be a result of noise or uncorrected features in the spectra that mimic planetary signals. Furthermore, as noted by Costa Silva, A.R. et al. (2024), the CCF process itself may introduce spurious peaks when template lines happen to align with unrelated spectral features. From Figure 4.7b we also conclude that the convolution of the model to the instrument's resolution and passing the model to a contrast model do not affect the results significantly. Likewise, from Figure 4.7c, we conclude the choice of routine to implement the CCF does not have significant impact, however, for practicality, we note that the routine from Costa Silva, A.R. et al. (2024) is faster.

For Epoch II, as we can see in Figure 4.5, the amplitude of the signal is underestimated by the Gaussian fit, due to to small spikes in amplitude close to the main peak. This epoch, together with Epoch I, showed the weakest detections. The difficulty in clearly identifying

the peak of Epoch II was somewhat surprising, since this night had the highest S/N and the best seeing conditions.

From the CCFs plots we report tentative detections for all epochs of observations, with peaks at RV and full width at half maximum, FWHM, values of 7.8, 23.9, 11.0 and 9.5 km s^{-1} for each epoch, respectively. For the four co-added epochs we report a detection of significance 4.3σ at RV $= -4.6 \pm 0.3$ and FWHM $= 12.9\,\mathrm{km\,s^{-1}}$. The detection of Fe I emission on the dayside of WASP-76b supports the existence of a thermal inversion layer in the dayside atmosphere. For the results grouped by orbital range (see Figure 4.9), we note that the v_{sys} shift decreases from before to after the occultation. A summary of these results is presented in Table 4.1. The uncertainties we present are a direct result of the Gaussian fit, therefore they are likely underestimated.

Table 4.1: Results from the Gaussian fits to the CCFs.

Species	Epoch	S/N	RV peak (km s^{-1})	FWHM (km s^{-1})
Fe I	I	1.7σ	-5.8 ± 0.3	7.8 ± 0.8
	II	2.0σ	-7.9 ± 0.9	23.9 ± 2.9
	III	3.4σ	-3.4 ± 0.4	11.0 ± 0.9
	IV	2.8σ	-2.4 ± 0.5	9.5 ± 1.3
	I & II (pre-eclipse)	2.2σ	-7.2 ± 0.5	15.6 ± 1.4
	III & IV (post-eclipse)	4.8σ	-3.0 ± 0.3	10.6 ± 0.8
	Four epochs co-added	4.3σ	-4.6 ± 0.3	12.9 ± 0.8

Figure 4.8 shows that, in accordance to Costa Silva, A.R. et al. (2024), the iron emission peak is not at the expected v_{sys} (0 in the PRF), but instead at a blueshifted value. However, unlike what is presented in the same study, we find a value of K_p different to the expected one $\left(K_p = 196.52\,\mathrm{km\,s^{-1}}\right)$, slightly shifted to the lower value of $K_p = 192\,\mathrm{km\,s^{-1}}$. Even though several factors rooted in the noise of the data and inherent method limitations may contribute to this effect, the lower value is in accordance to the recent findings of Guilluy et al. (2025) and Wardenier et al. (2025), and as mentioned in these papers it is in agreement with high-resolution emission observations of different UHJs (e.g. Hoeijmakers et al. (2024), Brogi et al. (2023), Cont et al. (2022)). This negative offset of the K_p value could then be a result of planet rotation.

As pointed out before, we find asymmetries in the position and strength of the CCF peaks between the post-eclipse and the pre-eclipse detections. From the K_p–v_{sys} map and the CCFs plots, we reach the same conclusion as Costa Silva, A.R. et al. (2024) that the emission signal of Fe I is blueshifted. The existence of a shift could be explained by atmospheric dynamics. Costa Silva, A.R. et al. (2024) suggests that the observed blueshift might arise

from a strong upward flow of material in the vicinity of the planet's substellar point, that is, the location on the planet's atmosphere that lies directly beneath the star, receiving the maximum stellar radiation. Moreover, as pointed out before, we find asymmetries in the position of this blueshift and strength of the CCF peaks between the post-eclipse and the pre-eclipse detections. According to Costa Silva, A.R. et al. (2024), the differences in the pre- and post-eclipse blueshifts can be explained by the existence of a hotspot displaced towards the west side of the planet's dayside. This way, the upflowing material would contribute to a larger blueshift during the pre-eclipse as the material moves away from the hotspot. Figure 4.10 schematizes the proposed explanation of Costa Silva, A.R. et al. (2024) to the different blueshifts before and after occultation. On the other hand, Wardenier et al. (2025) does not predict a blueshifted iron detection and the detections of Guilluy et al. (2025) seem to be consistent with a null RV shift. Figure 4.9 shows an asymmetry in peak strength, unlike the results of Costa Silva, A.R. et al. (2024), which was puzzling. However, such asymmetry was also detected in the same dataset by Guilluy et al. (2025), though we cannot rule out it being a result from the data pre-processing and excess noise in Epoch I and II. Guilluy et al. (2025) suggested attributing this asymmetry to a hotspot displacement from the substellar point, however, to the east side (see Figure 2 from the Appendix). This is based on the fact the line strength is dependent on the temperature gradient and not on the temperature value itself, thus near a hotspot the gradient would be lower, resulting in a weaker detection.

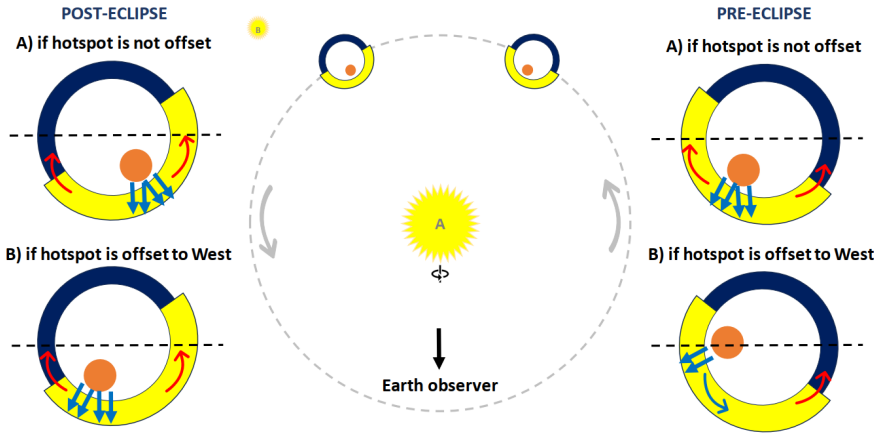

FIGURE 4.10: Figure 8 from Costa Silva, A.R. et al. (2024), showcasing a schematic of the WASP-76 system and the hypothesised hotspot geometry in a no-offset (A) and a west offset (B) scenarios, at pre- and post-eclipse positions. The effect of blue and redshifts is represented by blue and red arrows, respectively.

Ultimately, these interpretations are incompatible in regards to the location of the hotspot and the existence of a blueshift, possibly induced by differences in the data processing and

modelling or by missing physics in GCM works (Wardenier et al., 2025). This highlights the need for more observations to precisely constrain the properties and structure of the dayside of WASP-76 b.

Chapter 5

Conclusions

This work set out to investigate the dayside of WASP-76 b through the analysis of ESPRESSO data, providing insights into the challenges and opportunities of high-resolution exoplanet spectroscopy. The primary goal was to use the cross-correlation method to identify neutral iron emission signatures, thus confirming the existence of a thermal inverted atmospheric profile. We started with 148 exposures covering the orbital phases right before (pre) and after (post) the secondary eclipse, spanning the ranges of 0.34-0.47 and 0.54-0.62 in orbital phase. We corrected these data for telluric features, normalised it, handled their outliers, aligned them in the proper rest frames and removed the portion of the data corresponding to the stellar light, constructing a planetary spectra. The obtained planetary spectra was compared to a template we produced with petitRADTRANS using the CCF method. We present these results as CCFs added for each epoch, for the four epochs all together and for the joined pre- and post- occultation epochs in a S/N scale. We also show the K_p-v_{sys} detection map. We obtained a blueshifted detection of Fe I with a significance of 4.3σ at an RV value of $-4.6 \pm 0.3\,\mathrm{km\,s^{-1}}$ for all epochs co-added.

We obtained a lower value of K_p than expected ($K_p = 192\,\mathrm{km\,s^{-1}}$), whose origin is unclear (faults in the data processing, inherent noise or planet rotation). Most puzzling, we found that the blueshift is larger and the significance of the signal smaller for the pre-eclipse phase range than for the post-eclipse. The existence of a blueshift could be explained by some atmospheric scenarios, in particular, by a rising flow of hot material at the hotspot location of the atmosphere and travelling to the nightside. The asymmetry in the position of the shift could imply a westward deviation of this hotspot (Costa Silva, A.R. et al., 2024). In contrast, the asymmetry in the detection strength could indicate an eastward deviation of the hotspot (Guilluy et al., 2025). Simultaneously, recent studies could not confirm this blueshift (Guilluy et al., 2025).

While the results presented here provide intriguing evidence for thermal inversion and atmospheric dynamics in WASP-76 b, their interpretation remains limited by methodological and modelling uncertainties. Systematic effects in the data reduction, combined with the inherent challenges of isolating the faint planetary signal, underline the need for further refinement of the methodology. Nevertheless, this work demonstrates the potential of dayside emission spectroscopy with ESPRESSO and highlights the importance of combining such observations with future ones. Expanding this analysis to additional observations and instruments, as well as developing more physically comprehensive GCMs would benefit a broader understanding of the atmosphere of WASP-76 b and other ultra-hot Jupiters.

References

A. Wolszczan and D. A. Frail, "A planetary system around the millisecond pulsar PSR1257 + 12," , vol. 355, no. 6356, pp. 145–147, Jan. 1992. [Cited on page 1.]

M. Mayor and D. Queloz, "A Jupiter-mass companion to a solar-type star," , vol. 378, no. 6555, pp. 355–359, Nov. 1995. [Cited on page 1.]

D. Charbonneau, T. M. Brown, R. W. Noyes, and R. L. Gilliland, "Detection of an Extrasolar Planet Atmosphere," , vol. 568, no. 1, pp. 377–384, Mar. 2002. [Cited on pages 1 and 6.]

S. Redfield, M. Endl, W. D. Cochran, and L. Koesterke, "Sodium Absorption from the Exoplanetary Atmosphere of HD 189733b Detected in the Optical Transmission Spectrum," , vol. 673, no. 1, p. L87, Jan. 2008. [Cited on page 1.]

N. Madhusudhan, "Exoplanetary Atmospheres: Key Insights, Challenges, and Prospects," , vol. 57, pp. 617–663, Aug. 2019. [Cited on pages vi, 1, and 4.]

N. Grasser, I. A. G. Snellen, R. Landman, D. G. Picos, and S. Gandhi, "Peering above the clouds of the warm Neptune GJ 436 b with CRIRES+," , vol. 688, p. A191, Aug. 2024. [Cited on page 2.]

M. R. Swain, R. Estrela, G. M. Roudier, C. Sotin, P. B. Rimmer, A. Valio, R. West, K. Pearson, N. Huber-Feely, and R. T. Zellem, "Detection of an Atmosphere on a Rocky Exoplanet," , vol. 161, no. 5, p. 213, May 2021. [Cited on pages 2 and 6.]

R. Hu, A. Bello-Arufe, M. Zhang, K. Paragas, M. Zilinskas, C. van Buchem, M. Bess, J. Patel, Y. Ito, M. Damiano, M. Scheucher, A. V. Oza, H. A. Knutson, Y. Miguel, D. Dragomir, A. Brandeker, and B.-O. Demory, "A secondary atmosphere on the rocky exoplanet 55 Cancri e," , vol. 630, no. 8017, pp. 609–612, Jun. 2024. [Cited on pages 2 and 6.]

W. J. Borucki, D. G. Koch, G. Basri, N. Batalha, T. M. Brown, S. T. Bryson, D. Caldwell, J. Christensen-Dalsgaard, W. D. Cochran, E. DeVore, E. W. Dunham, T. N. Gautier, III, J. C. Geary, R. Gilliland, A. Gould, S. B. Howell, J. M. Jenkins, D. W. Latham, J. J. Lissauer, G. W. Marcy, J. Rowe, D. Sasselov, A. Boss, D. Charbonneau, D. Ciardi, L. Doyle, A. K. Dupree, E. B. Ford, J. Fortney, M. J. Holman, S. Seager, J. H. Steffen, J. Tarter, W. F. Welsh, C. Allen, L. A. Buchhave, J. L. Christiansen, B. D. Clarke, S. Das, J.-M.

Désert, M. Endl, D. Fabrycky, F. Fressin, M. Haas, E. Horch, A. Howard, H. Isaacson, H. Kjeldsen, J. Kolodziejczak, C. Kulesa, J. Li, P. W. Lucas, P. Machalek, D. McCarthy, P. MacQueen, S. Meibom, T. Miquel, A. Prsa, S. N. Quinn, E. V. Quintana, D. Ragozzine, W. Sherry, A. Shporer, P. Tenenbaum, G. Torres, J. D. Twicken, J. Van Cleve, L. Walkowicz, F. C. Witteborn, and M. Still, "Characteristics of Planetary Candidates Observed by Kepler. II. Analysis of the First Four Months of Data," , vol. 736, no. 1, p. 19, Jul. 2011. [Cited on page 2.]

B. S. Gaudi, S. Seager, and G. Mallen-Ornelas, "On the Period Distribution of Close-in Extrasolar Giant Planets," , vol. 623, no. 1, pp. 472–481, Apr. 2005. [Cited on page 2.]

N. Madhusudhan, H. Knutson, J. J. Fortney, and T. Barman, "Exoplanetary Atmospheres," in *Protostars and Planets VI*, H. Beuther, R. S. Klessen, C. P. Dullemond, and T. Henning, Eds., Jan. 2014, pp. 739–762. [Cited on pages 3, 4, 5, and 11.]

D. Charbonneau, L. E. Allen, S. T. Megeath, G. Torres, R. Alonso, T. M. Brown, R. L. Gilliland, D. W. Latham, G. Mandushev, F. T. O'Donovan, and A. Sozzetti, "Detection of Thermal Emission from an Extrasolar Planet," , vol. 626, no. 1, pp. 523–529, Jun. 2005. [Cited on page 4.]

M. Perryman, *The Exoplanet Handbook*, 2018. [Cited on pages vi, 4, 5, 10, and 11.]

A. Burrows, L. Ibgui, and I. Hubeny, "Optical Albedo Theory of Strongly Irradiated Giant Planets: The Case of HD 209458b," , vol. 682, no. 2, pp. 1277–1282, Aug. 2008. [Cited on page 5.]

J. F. Rowe, J. M. Matthews, S. Seager, E. Miller-Ricci, D. Sasselov, R. Kuschnig, D. B. Guenther, A. F. J. Moffat, S. M. Rucinski, G. A. H. Walker, and W. W. Weiss, "The Very Low Albedo of an Extrasolar Planet: MOST Space-based Photometry of HD 209458," , vol. 689, no. 2, pp. 1345–1353, Dec. 2008. [Cited on page 5.]

S. Seager and D. Deming, "On the Method to Infer an Atmosphere on a Tidally Locked Super Earth Exoplanet and Upper Limits to GJ 876d," , vol. 703, no. 2, pp. 1884–1889, Oct. 2009. [Cited on page 5.]

S. Seager, *Exoplanets*, 2010. [Cited on page 5.]

D. K. Sing, J. M. Désert, J. J. Fortney, A. Lecavelier Des Etangs, G. E. Ballester, J. Cepa, D. Ehrenreich, M. López-Morales, F. Pont, M. Shabram, and A. Vidal-Madjar, "Gran Telescopio Canarias OSIRIS transiting exoplanet atmospheric survey: detection of

potassium in XO-2b from narrowband spectrophotometry," , vol. 527, p. A73, Mar. 2011. [Cited on page 6.]

H. R. Wakeford, D. K. Sing, D. Deming, N. P. Gibson, J. J. Fortney, A. S. Burrows, G. Ballester, N. Nikolov, S. Aigrain, G. Henry, H. Knutson, A. Lecavelier des Etangs, F. Pont, A. P. Showman, A. Vidal-Madjar, and K. Zahnle, "Hst hot jupiter transmission spectral survey: detection of water in hat-p-1b from wfc3 near-ir spatial scan observations," *Monthly Notices of the Royal Astronomical Society*, vol. 435, no. 4, pp. 3481–3493, 09 2013. [Online]. Available: https://doi.org/10.1093/mnras/stt1536 [Cited on page 6.]

D. Deming, A. Wilkins, P. McCullough, A. Burrows, J. J. Fortney, E. Agol, I. Dobbs-Dixon, N. Madhusudhan, N. Crouzet, J.-M. Desert, R. L. Gilliland, K. Haynes, H. A. Knutson, M. Line, Z. Magic, A. M. Mandell, S. Ranjan, D. Charbonneau, M. Clampin, S. Seager, and A. P. Showman, "Infrared Transmission Spectroscopy of the Exoplanets HD 209458b and XO-1b Using the Wide Field Camera-3 on the Hubble Space Telescope," , vol. 774, no. 2, p. 95, Sep. 2013. [Cited on page 6.]

L. Kreidberg, J. L. Bean, J.-M. Désert, M. R. Line, J. J. Fortney, N. Madhusudhan, K. B. Stevenson, A. P. Showman, D. Charbonneau, P. R. McCullough, S. Seager, A. Burrows, G. W. Henry, M. Williamson, T. Kataria, and D. Homeier, "A precise water abundance measurement for the hot jupiter wasp-43b," *The Astrophysical Journal*, vol. 793, no. 2, p. L27, Sep. 2014. [Online]. Available: http://dx.doi.org/10.1088/2041-8205/793/2/L27 [Cited on page 6.]

M. R. Swain, G. Vasisht, and G. Tinetti, "Methane present in an extrasolar planet atmosphere," *arXiv e-prints*, p. arXiv:0802.1030, Feb. 2008. [Cited on page 6.]

M. Brogi, I. A. G. Snellen, R. J. de Kok, S. Albrecht, J. Birkby, and E. J. W. de Mooij, "The signature of orbital motion from the dayside of the planet τ Boötis b," , vol. 486, no. 7404, pp. 502–504, Jun. 2012. [Cited on pages 6 and 48.]

J. Yang, M. Hammond, A. A. A. Piette, J. Blecic, T. J. Bell, P. G. J. Irwin, V. Parmentier, S.-M. Tsai, J. K. Barstow, N. Crouzet, L. Kreidberg, J. M. Mendonça, J. Taylor, R. Baeyens, K. Ohno, L. Teinturier, and M. C. Nixon, "Simultaneous retrieval of orbital phase resolved JWST/MIRI emission spectra of the hot Jupiter WASP-43b: evidence of water, ammonia, and carbon monoxide," , vol. 532, no. 1, pp. 460–475, Jul. 2024. [Cited on page 6.]

N. Madhusudhan, S. Sarkar, S. Constantinou, M. Holmberg, A. A. A. Piette, and J. I. Moses, "Carbon-bearing Molecules in a Possible Hycean Atmosphere," , vol. 956, no. 1, p. L13, Oct. 2023. [Cited on page 6.]

T. Beatty, L. Welbanks, T. Bell, J. Fortney, T. Greene, M. Line, S. Mukherjee, M. Murphy, K. Ohno, V. Parmentier, E. Rauscher, E. Schlawin, and L. Wiser, "The Detection of Multiple Molecular Species in the Atmospheres of a Sub-Neptune and Super-Neptune," in *AASTCS10, Extreme Solar Systems V*, ser. AAS/Division for Extreme Solar Systems Abstracts, vol. 56, Apr. 2024, p. 103.06. [Cited on page 6.]

J. Fraine, D. Deming, B. Benneke, H. Knutson, A. Jordán, N. Espinoza, N. Madhusudhan, A. Wilkins, and K. Todorov, "Water vapour absorption in the clear atmosphere of a Neptune-sized exoplanet," , vol. 513, no. 7519, pp. 526–529, Sep. 2014. [Cited on page 6.]

A. A. Lanotte, M. Gillon, B. O. Demory, J. J. Fortney, N. Astudillo, X. Bonfils, P. Magain, X. Delfosse, T. Forveille, C. Lovis, M. Mayor, V. Neves, F. Pepe, D. Queloz, N. Santos, and S. Udry, "A global analysis of Spitzer and new HARPS data confirms the loneliness and metal-richness of GJ 436 b," , vol. 572, p. A73, Dec. 2014. [Cited on page 6.]

D. Charbonneau, T. M. Brown, D. W. Latham, and M. Mayor, "Detection of Planetary Transits Across a Sun-like Star," , vol. 529, no. 1, pp. L45–L48, Jan. 2000. [Cited on page 7.]

G. W. Henry, G. W. Marcy, R. P. Butler, and S. S. Vogt, "A Transiting "51 Peg-like" Planet," , vol. 529, no. 1, pp. L41–L44, Jan. 2000. [Cited on page 7.]

S. Seager and G. Mallén-Ornelas, "A Unique Solution of Planet and Star Parameters from an Extrasolar Planet Transit Light Curve," , vol. 585, no. 2, pp. 1038–1055, Mar. 2003. [Cited on page 7.]

J. N. Winn, "Exoplanet Transits and Occultations," in *Exoplanets*, S. Seager, Ed., 2010, pp. 55–77. [Cited on pages vi and 8.]

B. Prinoth, H. J. Hoeijmakers, D. Kitzmann, E. Sandvik, J. V. Seidel, M. Lendl, N. W. Borsato, B. Thorsbro, D. R. Anderson, D. Barrado, K. Kravchenko, R. Allart, V. Bourrier, H. M. Cegla, D. Ehrenreich, C. Fisher, C. Lovis, A. Guzmán-Mesa, S. Grimm, M. Hooton, B. M. Morris, M. Oreshenko, L. Pino, and K. Heng, "Titanium oxide and chemical inhomogeneity in the atmosphere of the exoplanet WASP-189 b," *Nature Astronomy*, vol. 6, pp. 449–457, Jan. 2022. [Cited on pages vi and 9.]

J. N. Winn, "Measuring accurate transit parameters," in *Transiting Planets*, ser. IAU Symposium, F. Pont, D. Sasselov, and M. J. Holman, Eds., vol. 253, Feb. 2009, pp. 99–109. [Cited on pages vi and 10.]

R. Alonso, T. Guillot, T. Mazeh, S. Aigrain, A. Alapini, P. Barge, A. Hatzes, and F. Pont, "The secondary eclipse of the transiting exoplanet CoRoT-2b," , vol. 501, no. 3, pp. L23–L26, Jul. 2009. [Cited on page 11.]

K. B. Sheppard, A. M. Mandell, P. Tamburo, S. Gandhi, A. Pinhas, N. Madhusudhan, and D. Deming, "Evidence for a Dayside Thermal Inversion and High Metallicity for the Hot Jupiter WASP-18b," , vol. 850, no. 2, p. L32, Dec. 2017. [Cited on page 11.]

I. A. G. Snellen, E. J. W. de Mooij, and A. Burrows, "Bright optical day-side emission from extrasolar planet CoRoT-2b," , vol. 513, p. A76, Apr. 2010. [Cited on page 11.]

F. Yan, L. Nortmann, A. Reiners, N. Piskunov, A. Hatzes, U. Seemann, D. Shulyak, A. Lavail, A. D. Rains, D. Cont, M. Rengel, F. Lesjak, E. Nagel, O. Kochukhov, S. Czesla, L. Boldt-Christmas, U. Heiter, J. V. Smoker, F. Rodler, P. Bristow, R. J. Dorn, Y. Jung, T. Marquart, and E. Stempels, "CRIRES$^+$ detection of CO emissions lines and temperature inversions on the dayside of WASP-18b and WASP-76b," , vol. 672, p. A107, Apr. 2023. [Cited on pages 11, 15, 18, and 19.]

J. H. C. Martins, N. C. Santos, P. Figueira, J. P. Faria, M. Montalto, I. Boisse, D. Ehrenreich, C. Lovis, M. Mayor, C. Melo, F. Pepe, S. G. Sousa, S. Udry, and D. Cunha, "Evidence for a spectroscopic direct detection of reflected light from <ASTROBJ>51 Pegasi b</ASTROBJ>," , vol. 576, p. A134, Apr. 2015. [Cited on page 11.]

B. Prinoth, "High-resolution transmission spectroscopy of gas giant atmospheres," Doctoral Thesis (compilation), Department of Physics, Apr. 2025, defence details Date: 2025-05-09 Time: 09:15 Place: Rydbergsalen, Fysikum, Lund. Join via Zoom: https://lu-se.zoom.us/j/67397942348?pwd=k7z5gnWTb4aqNVjbbBlruhYKAOqimQ. External reviewer(s) Name: Gibson, Neale Title: Professor Dr. Affiliation: Trinity College Dublin, Ireland —. [Cited on pages vi and 12.]

I. A. G. Snellen, R. J. de Kok, E. J. W. de Mooij, and S. Albrecht, "The orbital motion, absolute mass and high-altitude winds of exoplanet HD209458b," , vol. 465, no. 7301, pp. 1049–1051, Jun. 2010. [Cited on page 13.]

S. M. Simkin, "Measurements of Velocity Dispersions and Doppler Shifts from Digitized Optical Spectra," , vol. 31, p. 129, Mar. 1974. [Cited on page 13.]

S. K. Nugroho, H. Kawahara, K. Masuda, T. Hirano, T. Kotani, and A. Tajitsu, "High-resolution Spectroscopic Detection of TiO and a Stratosphere in the Day-side of WASP-33b," , vol. 154, no. 6, p. 221, Dec. 2017. [Cited on page 13.]

B. Prinoth, H. J. Hoeijmakers, S. Pelletier, D. Kitzmann, B. M. Morris, A. Seifahrt, D. Kasper, H. H. Korhonen, M. Burheim, J. L. Bean, B. Benneke, N. W. Borsato, M. Brady, S. L. Grimm, R. Luque, J. Stürmer, and B. Thorsbro, "Time-resolved transmission spectroscopy of the ultra-hot Jupiter WASP-189 b," , vol. 678, p. A182, Oct. 2023. [Cited on page 13.]

J. L. Birkby, R. J. de Kok, M. Brogi, E. J. W. de Mooij, H. Schwarz, S. Albrecht, and I. A. G. Snellen, "Detection of water absorption in the day side atmosphere of HD 189733 b using ground-based high-resolution spectroscopy at 3.2μm." , vol. 436, pp. L35–L39, Nov. 2013. [Cited on page 13.]

J. L. Birkby, R. J. de Kok, M. Brogi, H. Schwarz, and I. A. G. Snellen, "Discovery of Water at High Spectral Resolution in the Atmosphere of 51 Peg b," , vol. 153, no. 3, p. 138, Mar. 2017. [Cited on page 13.]

H. J. Hoeijmakers, D. Kitzmann, B. M. Morris, B. Prinoth, N. W. Borsato, B. Thorsbro, L. Pino, E. K. H. Lee, C. Akın, J. V. Seidel, J. L. Birkby, R. Allart, and K. Heng, "The Mantis Network. IV. A titanium cold trap on the ultra-hot Jupiter WASP-121 b," , vol. 685, p. A139, May 2024. [Cited on pages 13 and 55.]

Costa Silva, A.R., Demangeon, O. D. S., Santos, N. C., Ehrenreich, D., Lovis, C., Chakraborty, H., Lendl, M., Pepe, F., Cristiani, S., Rebolo, R., Zapatero-Osorio, M. R., Adibekyan, V., Alibert, Y., Allart, R., Allende Prieto, C., Azevedo Silva, T., Borsa, F., Bourrier, V., Cristo, E., Di Marcantonio, P., Esparza-Borges, E., Figueira, P., González Hernández, J. I., Herrero-Cisneros, E., Lo Curto, G., Martins, C. J. A. P., Mehner, A., Nunes, N. J., Palle, E., Pelletier, S., Seidel, J. V., Silva, A. M., Sousa, S. G., Sozzetti, A., Steiner, M., Suárez Mascareño, A., and Udry, S., "Espresso reveals blueshifted neutral iron emission lines on the dayside of wasp-76 b□," *AA*, vol. 689, p. A8, 2024. [Online]. Available: https://doi.org/10.1051/0004-6361/202449935 [Cited on pages vi, viii, 13, 16, 18, 19, 22, 26, 36, 39, 46, 48, 52, 54, 55, 56, and 58.]

B. Prinoth, J. V. Seidel, H. J. Hoeijmakers, B. M. Morris, M. Baratella, N. W. Borsato, Y. C. Damasceno, V. Parmentier, D. Kitzmann, E. Sedaghati, L. Pino, F. Borsa, R. Allart, N. Santos, M. Steiner, A. Suárez Mascareño, H. Tabernero, and M. R. Zapatero

Osorio, "Titanium chemistry of WASP-121 b with ESPRESSO in 4-UT mode," , vol. 694, p. A284, Feb. 2025. [Cited on page 13.]

S. R. Merritt, N. P. Gibson, S. K. Nugroho, E. J. W. de Mooij, M. J. Hooton, J. D. Lothringer, S. M. Matthews, T. Mikal-Evans, N. Nikolov, D. K. Sing, and C. A. Watson, "An inventory of atomic species in the atmosphere of WASP-121b using UVES high-resolution spectroscopy," , vol. 506, no. 3, pp. 3853–3871, Sep. 2021. [Cited on page 13.]

S. de Regt, A. Y. Kesseli, I. A. G. Snellen, S. R. Merritt, and K. L. Chubb, "A quantitative assessment of the VO line list: Inaccuracies hamper high-resolution VO detections in exoplanet atmospheres," , vol. 661, p. A109, May 2022. [Cited on page 13.]

E. Høg, C. Fabricius, V. V. Makarov, S. Urban, T. Corbin, G. Wycoff, U. Bastian, P. Schwekendiek, and A. Wicenec, "The Tycho-2 catalogue of the 2.5 million brightest stars," , vol. 355, pp. L27–L30, Mar. 2000. [Cited on pages 14 and 16.]

R. G. West, C. Hellier, J. M. Almenara, D. R. Anderson, S. C. C. Barros, F. Bouchy, D. J. A. Brown, A. Collier Cameron, M. Deleuil, L. Delrez, A. P. Doyle, F. Faedi, A. Fumel, M. Gillon, Y. Gómez Maqueo Chew, G. Hébrard, E. Jehin, M. Lendl, P. F. L. Maxted, F. Pepe, D. Pollacco, D. Queloz, D. Ségransan, B. Smalley, A. M. S. Smith, J. Southworth, A. H. M. J. Triaud, and S. Udry, "Three irradiated and bloated hot Jupiters:. WASP-76b, WASP-82b, and WASP-90b," , vol. 585, p. A126, Jan. 2016. [Cited on pages 14, 15, 16, and 39.]

D. Ehrenreich, C. Lovis, R. Allart, M. R. Zapatero Osorio, F. Pepe, S. Cristiani, R. Rebolo, N. C. Santos, F. Borsa, O. Demangeon, X. Dumusque, J. I. González Hernández, N. Casasayas-Barris, D. Ségransan, S. Sousa, M. Abreu, V. Adibekyan, M. Affolter, C. Allende Prieto, Y. Alibert, M. Aliverti, D. Alves, M. Amate, G. Avila, V. Baldini, T. Bandy, W. Benz, A. Bianco, □. Bolmont, F. Bouchy, V. Bourrier, C. Broeg, A. Cabral, G. Calderone, E. Pallé, H. M. Cegla, R. Cirami, J. M. P. Coelho, P. Conconi, I. Coretti, C. Cumani, G. Cupani, H. Dekker, B. Delabre, S. Deiries, V. D'Odorico, P. Di Marcantonio, P. Figueira, A. Fragoso, L. Genolet, M. Genoni, R. Génova Santos, N. Hara, I. Hughes, O. Iwert, F. Kerber, J. Knudstrup, M. Landoni, B. Lavie, J.-L. Lizon, M. Lendl, G. Lo Curto, C. Maire, A. Manescau, C. J. A. P. Martins, D. Mégevand, A. Mehner, G. Micela, A. Modigliani, P. Molaro, M. Monteiro, M. Monteiro, M. Moschetti, E. Müller, N. Nunes, L. Oggioni, A. Oliveira, G. Pariani, L. Pasquini, E. Poretti, J. L. Rasilla, E. Redaelli, M. Riva, S. Santana Tschudi, P. Santin, P. Santos,

A. Segovia Milla, J. V. Seidel, D. Sosnowska, A. Sozzetti, P. Spanò, A. Suárez Mascareño, H. Tabernero, F. Tenegi, S. Udry, A. Zanutta, and F. Zerbi, "Nightside condensation of iron in an ultrahot giant exoplanet," *Nature*, vol. 580, no. 7805, p. 597–601, Mar. 2020. [Online]. Available: http://dx.doi.org/10.1038/s41586-020-2107-1 [Cited on pages 14, 16, 17, 18, 19, and 39.]

O. D. S. Demangeon, P. E. Cubillos, V. Singh, T. G. Wilson, L. Carone, A. Bekkelien, A. Deline, D. Ehrenreich, P. F. L. Maxted, B. O. Demory, T. Zingales, M. Lendl, A. Bonfanti, S. G. Sousa, A. Brandeker, Y. Alibert, R. Alonso, J. Asquier, T. Bárczy, D. B. Navascues, S. C. C. Barros, W. Baumjohann, M. Beck, T. Beck, W. Benz, N. Billot, F. Biondi, L. Borsato, C. Broeg, M. Buder, A. C. Cameron, S. Csizmadia, M. B. Davies, M. Deleuil, L. Delrez, A. Erikson, A. Fortier, L. Fossati, M. Fridlund, D. Gandolfi, M. Gillon, M. Güdel, M. N. Günther, A. Heitzmann, C. Helling, S. Hoyer, K. G. Isaak, L. L. Kiss, K. W. F. Lam, J. Laskar, A. L. des Etangs, D. Magrin, M. Mecina, C. Mordasini, V. Nascimbeni, G. Olofsson, R. Ottensamer, I. Pagano, E. Pallé, G. Peter, G. Piotto, D. Pollacco, D. Queloz, R. Ragazzoni, N. Rando, H. Rauer, I. Ribas, M. Rieder, S. Salmon, N. C. Santos, G. Scandariato, D. Ségransan, A. E. Simon, A. M. S. Smith, M. Stalport, G. M. Szabó, N. Thomas, S. Udry, V. Van Grootel, J. Venturini, E. Villaver, and N. A. Walton, "Asymmetry in the atmosphere of the ultra-hot Jupiter WASP-76 b," , vol. 684, p. A27, Apr. 2024. [Cited on pages 14 and 17.]

V. Parmentier, M. R. Line, J. L. Bean, M. Mansfield, L. Kreidberg, R. Lupu, C. Visscher, J.-M. Désert, J. J. Fortney, M. Deleuil, J. Arcangeli, A. P. Showman, and M. S. Marley, "From thermal dissociation to condensation in the atmospheres of ultra hot jupiters: Wasp-121b in context," *Astronomy amp; Astrophysics*, vol. 617, p. A110, Sep. 2018. [Online]. Available: http://dx.doi.org/10.1051/0004-6361/201833059 [Cited on page 15.]

H. J. Hoeijmakers, D. Ehrenreich, D. Kitzmann, R. Allart, S. L. Grimm, J. V. Seidel, A. Wyttenbach, L. Pino, L. D. Nielsen, C. Fisher, P. B. Rimmer, V. Bourrier, H. M. Cegla, B. Lavie, C. Lovis, A. B. C. Patzer, J. W. Stock, F. A. Pepe, and K. Heng, "A spectral survey of an ultra-hot Jupiter. Detection of metals in the transmission spectrum of KELT-9 b," , vol. 627, p. A165, Jul. 2019. [Cited on page 15.]

K. Haynes, A. M. Mandell, N. Madhusudhan, D. Deming, and H. Knutson, "Spectroscopic evidence for a temperature inversion in the dayside atmosphere of hot jupiter wasp-33b," *The Astrophysical Journal*, vol. 806, no. 2, p. 146, jun 2015. [Online]. Available:

https://dx.doi.org/10.1088/0004-637X/806/2/146 [Cited on page 15.]

T. M. Evans, D. K. Sing, T. Kataria, J. Goyal, N. Nikolov, H. R. Wakeford, D. Deming, M. S. Marley, D. S. Amundsen, G. E. Ballester, J. K. Barstow, L. Ben-Jaffel, V. Bourrier, L. A. Buchhave, O. Cohen, D. Ehrenreich, A. García Muñoz, G. W. Henry, H. Knutson, P. Lavvas, A. L. d. Etangs, N. K. Lewis, M. López-Morales, A. M. Mandell, J. Sanz-Forcada, P. Tremblin, and R. Lupu, "An ultrahot gas-giant exoplanet with a stratosphere," *Nature*, vol. 548, no. 7665, p. 58–61, Aug. 2017. [Online]. Available: http://dx.doi.org/10.1038/nature23266 [Cited on page 15.]

L. Pino, J. Désert, M. Brogi, L. Malavolta, A. Wyttenbach, M. Line, J. Hoeijmakers, L. Fossati, A. Bonomo, V. Nascimbeni, V. Panwar, L. Affer, S. Benatti, K. Biazzo, A. Bignamini, F. Borsa, I. Carleo, R. Claudi, R. Cosentino, E. Covino, M. Damasso, S. Desidera, P. Giacobbe, A. Harutyunyan, A. Lanza, G. Leto, A. Maggio, J. Maldonado, L. Mancini, G. Micela, E. Molinari, I. Pagano, G. Piotto, E. Poretti, M. Rainer, G. Scandariato, A. Sozzetti, R. Allart, L. Borsato, G. Bruno, L. Fabrizio, D. Ehrenreich, A. Fiorenzano, G. Frustagli, B. Lavie, C. Lovis, A. Magazz, D. Nardiello, M. Pedani, and R. Smareglia, "Neutral iron emission lines from the dayside of kelt-9b: The gaps program with harps-n at tng xx," *Astrophysical Journal Letters*, vol. 894, no. 2, May 2020, publisher Copyright: © 2020. The American Astronomical Society. All rights reserved.. [Cited on pages 15 and 16.]

Yan, F., Pallé, E., Reiners, A., Molaverdikhani, K., Casasayas-Barris, N., Nortmann, L., Chen, G., Mollière, P., and Stangret, M., "A temperature inversion with atomic iron in the ultra-hot dayside atmosphere of wasp-189b⋆," *AA*, vol. 640, p. L5, 2020. [Online]. Available: https://doi.org/10.1051/0004-6361/202038294 [Cited on pages 15 and 16.]

B. Edwards, Q. Changeat, R. Baeyens, A. Tsiaras, A. Al-Refaie, J. Taylor, K. H. Yip, M. F. Bieger, D. Blain, A. Gressier, G. Guilluy, A. Y. Jaziri, F. Kiefer, D. Modirrousta-Galian, M. Morvan, L. V. Mugnai, W. Pluriel, M. Poveda, N. Skaf, N. Whiteford, S. Wright, T. Zingales, B. Charnay, P. Drossart, J. Leconte, O. Venot, I. Waldmann, and J.-P. Beaulieu, "Ares i: Wasp-76 b, a tale of two hst spectra*," *The Astronomical Journal*, vol. 160, no. 1, p. 8, jun 2020. [Online]. Available: https://dx.doi.org/10.3847/1538-3881/ab9225 [Cited on pages 15, 18, and 19.]

E. M. May, T. D. Komacek, K. B. Stevenson, E. M. R. Kempton, J. L. Bean, M. Malik, J. Ih, M. Mansfield, A. B. Savel, D. Deming, J.-M. Desert, Y. K. Feng, J. J. Fortney, T. Kataria,

N. Lewis, C. Morley, E. Rauscher, and A. Showman, "Spitzer Phase-curve Observations and Circulation Models of the Inflated Ultrahot Jupiter WASP-76b," , vol. 162, no. 4, p. 158, Oct. 2021. [Cited on page 15.]

G. Fu, D. Deming, J. Lothringer, N. Nikolov, D. K. Sing, E. M. R. Kempton, J. Ih, T. M. Evans, K. Stevenson, H. R. Wakeford, J. E. Rodriguez, J. D. Eastman, K. Stassun, G. W. Henry, M. López-Morales, M. Lendl, D. M. Conti, C. Stockdale, K. Collins, J. Kielkopf, J. K. Barstow, J. Sanz-Forcada, D. Ehrenreich, V. Bourrier, and L. A. dos Santos, "The Hubble PanCET Program: Transit and Eclipse Spectroscopy of the Strongly Irradiated Giant Exoplanet WASP-76b," , vol. 162, no. 3, p. 108, Sep. 2021. [Cited on pages 15, 18, and 19.]

I. Hubeny, A. Burrows, and D. Sudarsky, "A possible bifurcation in atmospheres of strongly irradiated stars and planets," *The Astrophysical Journal*, vol. 594, no. 2, p. 1011–1018, Sep. 2003. [Online]. Available: http://dx.doi.org/10.1086/377080 [Cited on page 15.]

J. J. Fortney, K. Lodders, M. S. Marley, and R. S. Freedman, "A Unified Theory for the Atmospheres of the Hot and Very Hot Jupiters: Two Classes of Irradiated Atmospheres," , vol. 678, no. 2, pp. 1419–1435, May 2008. [Cited on page 15.]

A. Tsiaras, I. P. Waldmann, T. Zingales, M. Rocchetto, G. Morello, M. Damiano, K. Karpouzas, G. Tinetti, L. K. McKemmish, J. Tennyson, and S. N. Yurchenko, "A Population Study of Gaseous Exoplanets," , vol. 155, no. 4, p. 156, Apr. 2018. [Cited on pages 15, 18, and 19.]

Q. Changeat, B. Edwards, A. F. Al-Refaie, A. Tsiaras, J. W. Skinner, J. Y. K. Cho, K. H. Yip, L. Anisman, M. Ikoma, M. F. Bieger, O. Venot, S. Shibata, I. P. Waldmann, and G. Tinetti, "Five Key Exoplanet Questions Answered via the Analysis of 25 Hot-Jupiter Atmospheres in Eclipse," , vol. 260, no. 1, p. 3, May 2022. [Cited on pages 15, 18, and 19.]

S. Pelletier, B. Benneke, M. Ali-Dib, B. Prinoth, D. Kasper, A. Seifahrt, J. Bean, F. Debras, B. Klein, L. Bazinet, H. Hoeijmakers, A. Kesseli, O. Lim, A. Carmona, L. Pino, N. Casasayas-Barris, T. Hood, and J. Stürmer, "Vanadium oxide and a sharp onset of cold-trapping on a giant exoplanet," *Nature*, vol. 619, no. 7970, pp. 491–494, Jul. 2023, publisher Copyright: © 2023, The Author(s), under exclusive licence to Springer Nature Limited. [Cited on pages 15, 16, 18, and 19.]

C. Maguire, N. P. Gibson, S. K. Nugroho, M. Fortune, S. Ramkumar, S. Gandhi, and E. de Mooij, "High resolution atmospheric retrievals of WASP-76b transmission spectroscopy with ESPRESSO: Monitoring limb asymmetries across multiple transits," , vol. 687, p. A49, Jul. 2024. [Cited on pages 15, 18, and 19.]

J. D. Lothringer, T. Barman, and T. Koskinen, "Extremely Irradiated Hot Jupiters: Non-oxide Inversions, H^- Opacity, and Thermal Dissociation of Molecules," , vol. 866, no. 1, p. 27, Oct. 2018. [Cited on page 15.]

C. Fisher and K. Heng, "Retrieval analysis of 38 WFC3 transmission spectra and resolution of the normalization degeneracy," , vol. 481, no. 4, pp. 4698–4727, Dec. 2018. [Cited on pages 16, 18, and 19.]

J. Žák, P. Kabáth, H. M. J. Boffin, V. D. Ivanov, and M. Skarka, "High-resolution transmission spectroscopy of four hot inflated gas giant exoplanets," *The Astronomical Journal*, vol. 158, no. 3, p. 120, aug 2019. [Online]. Available: https://dx.doi.org/10.3847/1538-3881/ab32ec [Cited on pages 16, 18, and 19.]

J. V. Seidel, D. Ehrenreich, A. Wyttenbach, R. Allart, M. Lendl, L. Pino, V. Bourrier, H. M. Cegla, C. Lovis, D. Barrado, D. Bayliss, N. Astudillo-Defru, A. Deline, C. Fisher, K. Heng, R. Joseph, B. Lavie, C. Melo, F. Pepe, D. Ségransan, and S. Udry, "Hot Exoplanet Atmospheres Resolved with Transit Spectroscopy (HEARTS). II. A broadened sodium feature on the ultra-hot giant WASP-76b," , vol. 623, p. A166, Mar. 2019. [Cited on pages 16, 18, and 19.]

H. J. Hoeijmakers, D. Ehrenreich, K. Heng, D. Kitzmann, S. L. Grimm, R. Allart, R. Deitrick, A. Wyttenbach, M. Oreshenko, L. Pino, P. B. Rimmer, E. Molinari, and L. Di Fabrizio, "Atomic iron and titanium in the atmosphere of the exoplanet KELT-9b," , vol. 560, no. 7719, pp. 453–455, Aug. 2018. [Cited on page 16.]

Bourrier, V., Ehrenreich, D., Lendl, M., Cretignier, M., Allart, R., Dumusque, X., Cegla, H. M., Suárez-Mascareño, A., Wyttenbach, A., Hoeijmakers, H. J., Melo, C., Kuntzer, T., Astudillo-Defru, N., Giles, H., Heng, K., Kitzmann, D., Lavie, B., Lovis, C., Murgas, F., Nascimbeni, V., Pepe, F., Pino, L., Segransan, D., and Udry, S., "Hot exoplanet atmospheres resolved with transit spectroscopy (hearts) - iii. atmospheric structure of the misaligned ultra-hot jupiter wasp-121b□□□," *AA*, vol. 635, p. A205, 2020. [Online]. Available: https://doi.org/10.1051/0004-6361/201936640 [Cited on page 16.]

Borsa, F., Giacobbe, P., Bonomo, A. S., Brogi, M., Pino, L., Fossati, L., Lanza, A. F., Nascimbeni, V., Sozzetti, A., Amadori, F., Benatti, S., Biazzo, K., Bignamini, A., Boschin, W., Claudi, R., Cosentino, R., Covino, E., Desidera, S., Fiorenzano, A. F. M., Guilluy, G., Harutyunyan, A., Maggio, A., Maldonado, J., Mancini, L., Micela, G., Molinari, E., Molinaro, M., Pagano, I., Pedani, M., Piotto, G., Poretti, E., Rainer, M., Scandariato, G., and Stoev, H., "The gaps programme at tng - xxxiii. harps-n detects multiple atomic species in emission from the dayside of kelt-20b□," *AA*, vol. 663, p. A141, 2022. [Online]. Available: https://doi.org/10.1051/0004-6361/202142768 [Cited on page 16.]

G. Scandariato, F. Borsa, A. Bonomo, B. Gaudi, T. Henning, I. Ilyin, M. Johnson, L. Malavolta, M. Mallonn, K. Molaverdikhani, V. Nascimbeni, J. Pateince, L. Pino, K. Poppenhaeger, E. Schlawin, E. Shkolnik, D. Sicilia, A. Sozzetti, K. Strassmeier, and F. Yan, "The pepsi exoplanet transit survey (pets). iii. the detection of fe i, cr i, and ti i in the atmosphere of mascara-1 b through high-resolution emission spectroscopy," *Astronomy Astrophysics*, vol. 674, 04 2023. [Cited on page 16.]

S. K. Nugroho, N. P. Gibson, E. J. W. de Mooij, M. K. Herman, C. A. Watson, H. Kawahara, and S. R. Merritt, "Detection of fe i emission in the dayside spectrum of wasp-33b*," *The Astrophysical Journal Letters*, vol. 898, no. 2, p. L31, jul 2020. [Online]. Available: https://dx.doi.org/10.3847/2041-8213/aba4b6 [Cited on page 16.]

A. Y. Kesseli and I. A. G. Snellen, "Confirmation of asymmetric iron absorption in wasp-76b with harps," *The Astrophysical Journal Letters*, vol. 908, no. 1, p. L17, feb 2021. [Online]. Available: https://dx.doi.org/10.3847/2041-8213/abe047 [Cited on pages 16, 18, and 19.]

A. Y. Kesseli, I. A. G. Snellen, N. Casasayas-Barris, P. Mollière, and A. Sánchez-López, "An Atomic Spectral Survey of WASP-76b: Resolving Chemical Gradients and Asymmetries," , vol. 163, no. 3, p. 107, Mar. 2022. [Cited on pages 16, 18, and 19.]

Gaia Collaboration, "VizieR Online Data Catalog: Gaia EDR3 (Gaia Collaboration, 2020)," VizieR On-line Data Catalog: I/350. Originally published in: 2021A&A...649A...1G, Nov. 2020. [Cited on page 16.]

T. Azevedo Silva, O. D. S. Demangeon, N. C. Santos, R. Allart, F. Borsa, E. Cristo, E. Esparza-Borges, J. V. Seidel, E. Palle, S. G. Sousa, H. M. Tabernero, M. R. Zapatero Osorio, S. Cristiani, F. Pepe, R. Rebolo, V. Adibekyan, Y. Alibert, S. C. C.

Barros, F. Bouchy, V. Bourrier, G. Lo Curto, P. Di Marcantonio, V. D'Odorico, D. Ehrenreich, P. Figueira, J. I. González Hernández, C. Lovis, C. J. A. P. Martins, A. Mehner, G. Micela, P. Molaro, D. Mounzer, N. J. Nunes, A. Sozzetti, A. Suárez Mascareño, and S. Udry, "Detection of barium in the atmospheres of the ultra-hot gas giants wasp-76b and wasp-121b: Together with new detections of co and sr+ on wasp-121b," *Astronomy amp; Astrophysics*, vol. 666, p. L10, Oct. 2022. [Online]. Available: http://dx.doi.org/10.1051/0004-6361/202244489 [Cited on pages 18 and 19.]

H. M. Tabernero, M. R. Zapatero Osorio, R. Allart, F. Borsa, N. Casasayas-Barris, O. Demangeon, D. Ehrenreich, J. Lillo-Box, C. Lovis, E. Pallé, S. G. Sousa, R. Rebolo, N. C. Santos, F. Pepe, S. Cristiani, V. Adibekyan, C. Allende Prieto, Y. Alibert, S. C. C. Barros, F. Bouchy, V. Bourrier, V. D'Odorico, X. Dumusque, J. P. Faria, P. Figueira, R. Génova Santos, J. I. González Hernández, S. Hojjatpanah, G. Lo Curto, B. Lavie, C. J. A. P. Martins, J. H. C. Martins, A. Mehner, G. Micela, P. Molaro, N. J. Nunes, E. Poretti, J. V. Seidel, A. Sozzetti, A. Suárez Mascareño, S. Udry, M. Aliverti, M. Affolter, D. Alves, M. Amate, G. Avila, T. Bandy, W. Benz, A. Bianco, C. Broeg, A. Cabral, P. Conconi, J. Coelho, C. Cumani, S. Deiries, H. Dekker, B. Delabre, A. Fragoso, M. Genoni, L. Genolet, I. Hughes, J. Knudstrup, F. Kerber, M. Landoni, J. L. Lizon, C. Maire, A. Manescau, P. Di Marcantonio, D. Mégevand, M. Monteiro, M. Monteiro, M. Moschetti, E. Mueller, A. Modigliani, L. Oggioni, A. Oliveira, G. Pariani, L. Pasquini, J. L. Rasilla, E. Redaelli, M. Riva, S. Santana-Tschudi, P. Santin, P. Santos, A. Segovia, D. Sosnowska, P. Spanò, F. Tenegi, O. Iwert, A. Zanutta, and F. Zerbi, "ESPRESSO high-resolution transmission spectroscopy of WASP-76 b," , vol. 646, p. A158, Feb. 2021. [Cited on pages 18 and 19.]

N. Casasayas-Barris, J. Orell-Miquel, M. Stangret, L. Nortmann, F. Yan, M. Oshagh, E. Palle, J. Sanz-Forcada, M. López-Puertas, E. Nagel, R. Luque, G. Morello, I. A. G. Snellen, M. Zechmeister, A. Quirrenbach, J. A. Caballero, I. Ribas, A. Reiners, P. J. Amado, G. Bergond, S. Czesla, T. Henning, S. Khalafinejad, K. Molaverdikhani, D. Montes, M. Perger, A. Sánchez-López, and E. Sedaghati, "CARMENES detection of the Ca II infrared triplet and possible evidence of He I in the atmosphere of WASP-76b," , vol. 654, p. A163, Oct. 2021. [Cited on pages 18 and 19.]

E. K. Deibert, E. J. W. de Mooij, R. Jayawardhana, J. D. Turner, A. Ridden-Harper, L. Fossati, C. E. Hood, J. J. Fortney, L. Flagg, R. MacDonald, R. Allart, and D. K. Sing, "Detection of Ionized Calcium in the Atmosphere of the Ultra-hot Jupiter WASP-76b," , vol.

919, no. 2, p. L15, Oct. 2021. [Cited on pages 18 and 19.]

E. K. Deibert, E. J. W. de Mooij, R. Jayawardhana, J. D. Turner, A. Ridden-Harper, C. E. Hood, J. J. Fortney, L. Flagg, L. Fossati, R. Allart, M. Brogi, and R. J. MacDonald, "Exo-GemS High-resolution Transmission Spectroscopy of WASP-76b with GRACES," , vol. 166, no. 4, p. 141, Oct. 2023. [Cited on pages 18 and 19.]

M. Lampón, M. López-Puertas, J. Sanz-Forcada, S. Czesla, L. Nortmann, N. Casasayas-Barris, J. Orell-Miquel, A. Sánchez-López, C. Danielski, E. Pallé, K. Molaverdikhani, T. Henning, J. A. Caballero, P. J. Amado, A. Quirrenbach, A. Reiners, and I. Ribas, "Characterisation of the upper atmospheres of HAT-P-32 b, WASP-69 b, GJ 1214 b, and WASP-76 b through their He I triplet absorption," , vol. 673, p. A140, May 2023. [Cited on pages 18 and 19.]

A. Masson, S. Vinatier, B. Bézard, M. López-Puertas, M. Lampón, F. Debras, A. Carmona, B. Klein, E. Artigau, W. Dethier, S. Pelletier, T. Hood, R. Allart, V. Bourrier, C. Cadieux, B. Charnay, N. B. Cowan, N. J. Cook, X. Delfosse, J. F. Donati, P. G. Gu, G. Hébrard, E. Martioli, C. Moutou, O. Venot, and A. Wyttenbach, "Probing atmospheric escape through metastable He I triplet lines in 15 exoplanets observed with SPIRou," , vol. 688, p. A179, Aug. 2024. [Cited on pages 18 and 19.]

J. V. Seidel, D. Ehrenreich, R. Allart, H. J. Hoeijmakers, C. Lovis, V. Bourrier, L. Pino, A. Wyttenbach, V. Adibekyan, Y. Alibert, F. Borsa, N. Casasayas-Barris, S. Cristiani, O. D. S. Demangeon, P. Di Marcantonio, P. Figueira, J. I. González Hernández, J. Lillo-Box, C. J. A. P. Martins, A. Mehner, P. Molaro, N. J. Nunes, E. Palle, F. Pepe, N. C. Santos, S. G. Sousa, A. Sozzetti, H. M. Tabernero, and M. R. Zapatero Osorio, "Into the storm: diving into the winds of the ultra-hot Jupiter WASP-76 b with HARPS and ESPRESSO," , vol. 653, p. A73, Sep. 2021. [Cited on pages 18 and 19.]

K. Kawauchi, N. Narita, B. Sato, and Y. Kawashima, "Investigation of the upper atmosphere in ultra-hot jupiter wasp-76 b with high-resolution spectroscopy," *Publication of the Astronomical Society of Japan*, vol. 74, no. 2, pp. 225–238, Apr. 2022, publisher Copyright: © 2022 The Author(s) 2022. Published by Oxford University Press on behalf of the Astronomical Society of Japan. [Cited on pages 18 and 19.]

D. Sicilia, L. Malavolta, G. Scandariato, L. Fossati, A. F. Lanza, A. S. Bonomo, F. Borsa, G. Guilluy, V. Nascimbeni, L. Pino, F. Biassoni, M. C. D'Arpa, I. Pagano, A. Sozzetti, M. Stangret, R. Cosentino, P. Giacobbe, M. Lodi, J. Maldonado, D. Nardiello, and

M. Pedani, "The GAPS programme at TNG: LXVI. A homogeneous search for Na I and its possible variability in ten gas giant exoplanets," , vol. 693, p. A316, Jan. 2025. [Cited on pages 18 and 19.]

M. Weiner Mansfield, M. R. Line, J. P. Wardenier, M. Brogi, J. L. Bean, H. Beltz, P. Smith, J. A. Zalesky, N. Batalha, E. M. R. Kempton, B. T. Montet, J. E. Owen, P. Plavchan, and E. Rauscher, "The Metallicity and Carbon-to-oxygen Ratio of the Ultrahot Jupiter WASP-76b from Gemini-S/IGRINS," , vol. 168, no. 1, p. 14, Jul. 2024. [Cited on pages 18 and 19.]

A. Sánchez-López, R. Landman, P. Mollière, N. Casasayas-Barris, A. Y. Kesseli, and I. A. G. Snellen, "Searching for the origin of the Ehrenreich effect in ultra-hot Jupiters. Evidence for strong C/O gradients in the atmosphere of WASP-76 b?" , vol. 661, p. A78, May 2022. [Cited on pages 18 and 19.]

S. Gandhi, R. Landman, I. Snellen, L. Welbanks, N. Madhusudhan, and M. Brogi, "Revealing H_2O dissociation in WASP-76 b through combined high- and low-resolution transmission spectroscopy," , vol. 530, no. 3, pp. 2885–2894, May 2024. [Cited on pages 18 and 19.]

R. Landman, A. Sánchez-López, P. Mollière, A. Y. Kesseli, A. J. Louca, and I. A. G. Snellen, "Detection of OH in the ultra-hot Jupiter WASP-76b," , vol. 656, p. A119, Dec. 2021. [Cited on pages 18 and 19.]

F. Pepe, S. Cristiani, R. Rebolo, N. C. Santos, H. Dekker, A. Cabral, P. Di Marcantonio, P. Figueira, G. Lo Curto, C. Lovis, M. Mayor, D. Mégevand, P. Molaro, M. Riva, M. R. Zapatero Osorio, M. Amate, A. Manescau, L. Pasquini, F. M. Zerbi, V. Adibekyan, M. Abreu, M. Affolter, Y. Alibert, M. Aliverti, R. Allart, C. Allende Prieto, D. Álvarez, D. Alves, G. Avila, V. Baldini, T. Bandy, S. C. C. Barros, W. Benz, A. Bianco, F. Borsa, V. Bourrier, F. Bouchy, C. Broeg, G. Calderone, R. Cirami, J. Coelho, P. Conconi, I. Coretti, C. Cumani, G. Cupani, V. D'Odorico, M. Damasso, S. Deiries, B. Delabre, O. D. S. Demangeon, X. Dumusque, D. Ehrenreich, J. P. Faria, A. Fragoso, L. Genolet, M. Genoni, R. Génova Santos, J. I. González Hernández, I. Hughes, O. Iwert, F. Kerber, J. Knudstrup, M. Landoni, B. Lavie, J. Lillo-Box, J. L. Lizon, C. Maire, C. J. A. P. Martins, A. Mehner, G. Micela, A. Modigliani, M. A. Monteiro, M. J. P. F. G. Monteiro, M. Moschetti, M. T. Murphy, N. Nunes, L. Oggioni, A. Oliveira, M. Oshagh, E. Pallé, G. Pariani, E. Poretti, J. L. Rasilla, J. Rebordão, E. M. Redaelli, S. Santana Tschudi, P. Santin, P. Santos, D. Ségransan, T. M. Schmidt, A. Segovia, D. Sosnowska, A. Sozzetti,

S. G. Sousa, P. Spanò, A. Suárez Mascareño, H. Tabernero, F. Tenegi, S. Udry, and A. Zanutta, "ESPRESSO at VLT. On-sky performance and first results," , vol. 645, p. A96, Jan. 2021. [Cited on pages 20 and 24.]

A. Smette, H. Sana, S. Noll, H. Horst, W. Kausch, S. Kimeswenger, M. Barden, C. Szyszka, A. M. Jones, A. Gallenne, J. Vinther, P. Ballester, and J. Taylor, "Molecfit: A general tool for telluric absorption correction. I. Method and application to ESO instruments," , vol. 576, p. A77, Apr. 2015. [Cited on pages 24 and 25.]

W. Kausch, S. Noll, A. Smette, S. Kimeswenger, M. Barden, C. Szyszka, A. M. Jones, H. Sana, H. Horst, and F. Kerber, "Molecfit: A general tool for telluric absorption correction. II. Quantitative evaluation on ESO-VLT/X-Shooterspectra," , vol. 576, p. A78, Apr. 2015. [Cited on page 24.]

S. A. Clough, M. W. Shephard, E. J. Mlawer, J. S. Delamere, M. J. Iacono, K. Cady-Pereira, S. Boukabara, and P. D. Brown, "Atmospheric radiative transfer modeling: a summary of the AER codes," , vol. 91, no. 2, pp. 233–244, Mar. 2005. [Cited on page 25.]

M. Cretignier, J. Francfort, X. Dumusque, R. Allart, and F. Pepe, "RASSINE: Interactive tool for normalising stellar spectra. I. Description and performance of the code," , vol. 640, p. A42, Aug. 2020. [Cited on page 30.]

J. V. Seidel, "Exoplanet winds: Modelling atmospheric dynamics via resolved spectral lines," Ph.D. dissertation, Université de Genève, May 2021, dOI: 10.13097/archive-ouverte/unige:152927. [Online]. Available: https://archive-ouverte.unige.ch/unige:152927 [Cited on pages vii and 39.]

C. Soubiran, G. Jasniewicz, L. Chemin, C. Zurbach, N. Brouillet, P. Panuzzo, P. Sartoretti, D. Katz, J. F. Le Campion, O. Marchal, D. Hestroffer, F. Thévenin, F. Crifo, S. Udry, M. Cropper, G. Seabroke, Y. Viala, K. Benson, R. Blomme, A. Jean-Antoine, H. Huckle, M. Smith, S. G. Baker, Y. Damerdji, C. Dolding, Y. Frémat, E. Gosset, A. Guerrier, L. P. Guy, R. Haigron, K. Janßen, G. Plum, C. Fabre, Y. Lasne, F. Pailler, C. Panem, F. Riclet, F. Royer, G. Tauran, T. Zwitter, A. Gueguen, and C. Turon, "Gaia Data Release 2. The catalogue of radial velocity standard stars," , vol. 616, p. A7, Aug. 2018. [Cited on page 39.]

E. F. S. Valente and A. C. M. Correia, "Tidal excitation of the obliquity of Earth-like planets in the habitable zone of M-dwarf stars," , vol. 665, p. A130, Sep. 2022. [Cited on page 39.]

P. Mollière, J. P. Wardenier, R. van Boekel, T. Henning, K. Molaverdikhani, and I. A. G. Snellen, "petitRADTRANS. A Python radiative transfer package for exoplanet characterization and retrieval," , vol. 627, p. A67, Jul. 2019. [Cited on page 45.]

A. Borysow, U. G. Jorgensen, and Y. Fu, "High-temperature (1000-7000 K) collision-induced absorption of H"2 pairs computed from the first principles, with application to cool and dense stellar atmospheres," , vol. 68, pp. 235–255, Feb. 2001. [Cited on page 45.]

A. Borysow, "Collision-induced absorption coefficients of H_2 pairs at temperatures from 60 K to 1000 K," , vol. 390, pp. 779–782, Aug. 2002. [Cited on page 45.]

J. Borysow, L. Frommhold, and G. Birnbaum, "Collision-induced Rototranslational Absorption Spectra of H 2-He Pairs at Temperatures from 40 to 3000 K," , vol. 326, p. 509, Mar. 1988. [Cited on page 45.]

A. Borysow, L. Frommhold, and M. Moraldi, "Collision-induced Infrared Spectra of H 2-He Pairs Involving 0 1 Vibrational Transitions and Temperatures from 18 to 7000 K," , vol. 336, p. 495, Jan. 1989. [Cited on page 45.]

A. Borysow and L. Frommhold, "Collision-induced Infrared Spectra of H 2-He Pairs at Temperatures from 18 to 7000 K. II. Overtone and Hot Bands," , vol. 341, p. 549, Jun. 1989. [Cited on page 45.]

K. Lodders, "Solar elemental abundances," 12 2020. [Online]. Available: https://oxfordre.com/planetaryscience/view/10.1093/acrefore/9780190647926.001.0001/acrefore-9780190647926-e-145 [Cited on page 46.]

J. P. Wardenier, V. Parmentier, E. K. H. Lee, M. R. Line, and E. Gharib-Nezhad, "Decomposing the iron cross-correlation signal of the ultra-hot Jupiter WASP-76b in transmission using 3D Monte Carlo radiative transfer," , vol. 506, no. 1, pp. 1258–1283, Sep. 2021. [Cited on page 46.]

J. P. Wardenier, V. Parmentier, M. R. Line, and E. K. H. Lee, "Modelling the effect of 3D temperature and chemistry on the cross-correlation signal of transiting ultra-hot Jupiters: a study of five chemical species on WASP-76b," , vol. 525, no. 4, pp. 4942–4961, Nov. 2023. [Cited on page 46.]

J. P. Wardenier, V. Parmentier, E. K. H. Lee, and M. R. Line, "From Pretransit to Posteclipse: Investigating the Impact of 3D Temperature, Chemistry, and Dynamics on High-resolution Emission Spectra of the Ultrahot Jupiter WASP-76b," , vol. 986, no. 1, p. 63, Jun. 2025. [Cited on pages 46, 55, 56, and 57.]

T. Guillot, "On the radiative equilibrium of irradiated planetary atmospheres," , vol. 520, p. A27, Sep. 2010. [Cited on page 46.]

L. Boldt-Christmas, F. Lesjak, A. Wehrhahn, N. Piskunov, A. D. Rains, L. Nortmann, and O. Kochukhov, "Optimising spectroscopic observations of transiting exoplanets," , vol. 683, p. A244, Mar. 2024. [Cited on page 48.]

G. Guilluy, P. Giacobbe, M. Brogi, F. Borsa, J. P. Wardenier, F. Amadori, P. E. Cubillos, M. Basilicata, A. S. Bonomo, A. Sozzetti, I. Carleo, T. Azevedo Silva, A. Bignamini, M. Damasso, C. Di Maio, A. Ghedina, M. Lodi, L. Mancini, F. Manni, G. Micela, V. Nascimbeni, D. Nardiello, L. Pino, M. Rainer, and G. Scandariato, "The GAPS Programme at TNG. LXIX.The Dayside of WASP-76b revealed by GIANO-B, HARPS-N and ESPRESSO: Evidence for Three-Dimensional Atmospheric Effects," *arXiv e-prints*, p. arXiv:2507.19299, Jul. 2025. [Cited on pages viii, 55, 56, 58, and 78.]

M. Brogi, V. Emeka-Okafor, M. R. Line, S. Gandhi, L. Pino, E. M. R. Kempton, E. Rauscher, V. Parmentier, J. L. Bean, G. N. Mace, N. B. Cowan, E. Shkolnik, J. P. Wardenier, M. Mansfield, L. Welbanks, P. Smith, J. J. Fortney, J. L. Birkby, J. A. Zalesky, L. Dang, J. Patience, and J.-M. Désert, "The Roasting Marshmallows Program with IGRINS on Gemini South I: Composition and Climate of the Ultrahot Jupiter WASP-18 b," , vol. 165, no. 3, p. 91, Mar. 2023. [Cited on page 55.]

D. Cont, F. Yan, A. Reiners, L. Nortmann, K. Molaverdikhani, E. Pallé, T. Henning, I. Ribas, A. Quirrenbach, J. A. Caballero, P. J. Amado, S. Czesla, F. Lesjak, M. López-Puertas, P. Mollière, D. Montes, G. Morello, E. Nagel, S. Pedraz, and A. Sánchez-López, "Atmospheric characterization of the ultra-hot Jupiter WASP-33b. Detection of Ti and V emission lines and retrieval of a broadened line profile," , vol. 668, p. A53, Dec. 2022. [Cited on page 55.]

Appendix: Additional Figures

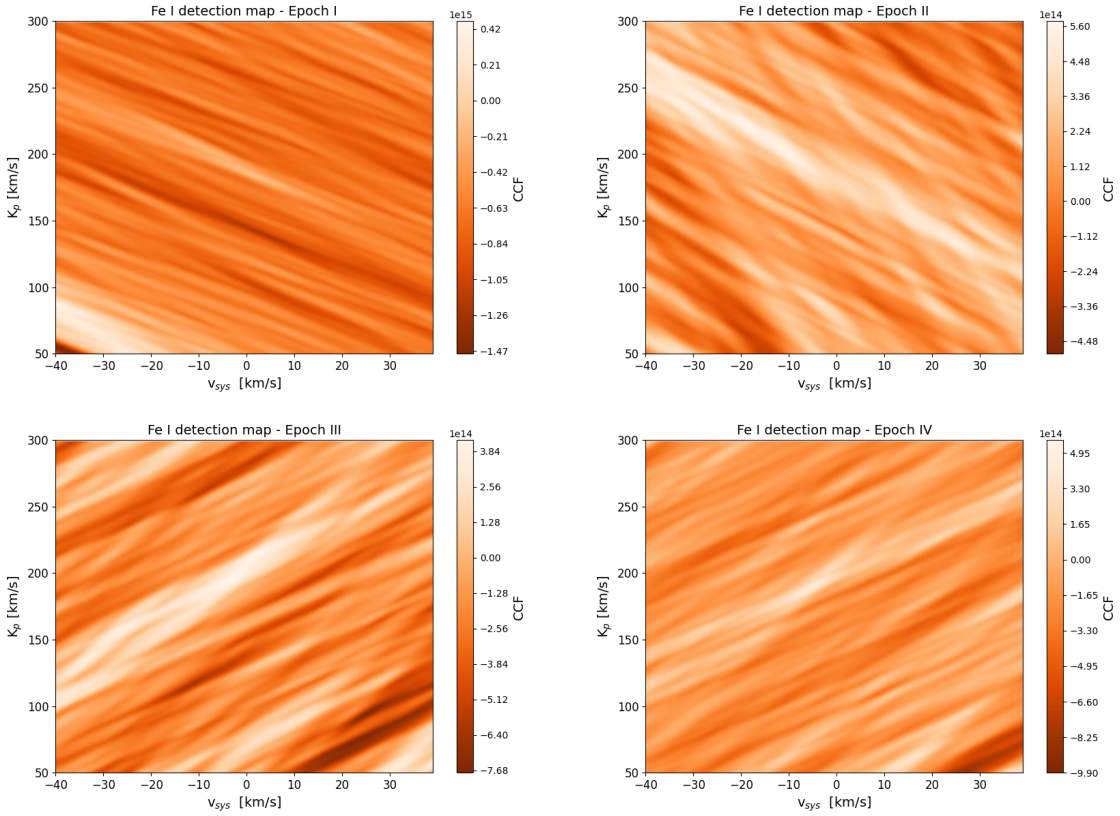

FIGURE 1: Same as Figure 4.8 for each epoch separately.

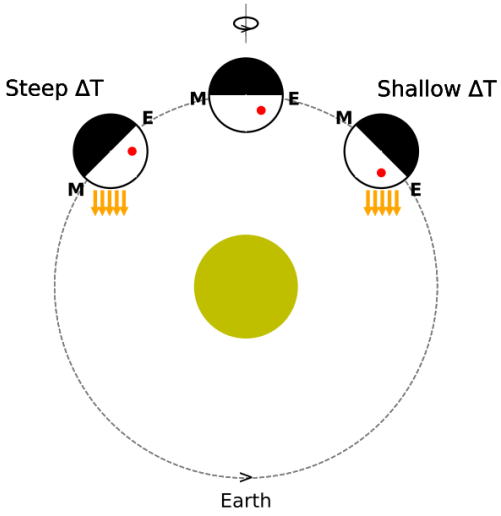

FIGURE 2: Part of Figure A.7 from Guilluy et al. (2025), showcasing a schematic of the WASP-76 system, assuming a hotspot deviated towards East and its effect on the observed temperature gradient.